



NATIONAL TECHNICAL UNIVERSITY OF ATHENS

DIPLOMA THESIS

The CAST experiment at CERN

Author:
Sofia KOSTOGLOU

Supervisors:
E. GAZIS
M. DAVENPORT

School of Electrical and Computer Engineering

June, 2016



ΕΘΝΙΚΟ ΜΕΤΣΟΒΙΟ ΠΟΛΥΤΕΧΝΕΙΟ

ΔΙΠΛΩΜΑΤΙΚΗ ΕΡΓΑΣΙΑ

Το πείραμα CAST στο CERN

Συγγραφέας:
Σοφία ΚΩΣΤΟΓΛΟΥ

Επιβλέποντες:
Ε. ΓΑΖΗΣ
Μ. DAVENPORT

Σχολή ηλεκτρολόγων μηχανικών & μηχανικών Η/Υ

Ιούνιος, 2016



ΕΘΝΙΚΟ ΜΕΤΣΟΒΙΟ ΠΟΛΥΤΕΧΝΕΙΟ
Σχολή ηλεκτρολόγων μηχανικών & μηχανικών Η/Υ

ΔΙΠΛΩΜΑΤΙΚΗ ΕΡΓΑΣΙΑ

Το πείραμα CAST στο CERN

Συγγραφέας:
Σοφία ΚΩΣΤΟΓΛΟΥ

Επιβλέποντες:
Ε. ΓΑΖΗΣ
Μ. DAVENPORT

Εγκρίθηκε από την τριμελή εξεταστική επιτροπή την 23^η Ιουνίου 2016.

(Υπογραφή)

(Υπογραφή)

(Υπογραφή)

.....
Ευάγγελος Γαζής
Καθηγητής Ε.Μ.Π

.....
Ηλίας Ν. Γλύτσας
Καθηγητής Ε.Μ.Π

.....
Ιωάννης Ξανθάκης
Καθηγητής Ε.Μ.Π

Ιούνιος, 2016

(Υπογραφή)

.....
ΚΩΣΤΟΓΛΟΥ ΣΟΦΙΑ

Διπλωματούχος Ηλεκτρολόγος Μηχανικός και Μηχανικός Υπολογιστών Ε.Μ.Π

© 2016- All rights reserved

Acknowledgements

From August 2015 I have been given the opportunity to work as a technical student in the CAST experiment. Over the past year I worked closely with many interesting people that offered guidance, help and influenced my first research steps and I would like to thank everyone from the CAST collaboration.

I would like to express my gratitude to my supervisors, Martyn Davenport and Theodoros Vafeiadis, for the guidance and the tremendous amount of patience. I have been extremely lucky to work under the supervision of people that cared so much about my work and responded to all of my queries.

I sincerely thank my professor, Evangelos Gazis, for his encouragement, his unlimited support and for the opportunity to embark on this project.

Last but not least, I would like to thank my family and my best friend, Serafeim Loukas, without whom my journey at CERN would not have been possible.

NATIONAL TECHNICAL UNIVERSITY OF ATHENS
School of Electrical and Computer Engineering

Abstract

The CAST experiment at CERN

The introduction of the theta angle as a solution to the $U(1)_A$ problem in the Lagrangian of QCD indicates a violation of Charge-Parity in strong interactions, which is not observed leading to the strong CP problem. From experimental results, the neutron electric dipole moment and thus the theta angle is orders of magnitude more strict than expected. A solution to this invokes a new global symmetry, the Peccei-Quinn symmetry. The spontaneous breaking of this symmetry at a specific energy scale predicts the existence of a light, neutral and weakly interacting Nambu-Goldstone boson, the axion. The characteristic of the axion, its mass and its coupling constant, are inversely proportional to the breaking f_a of the energy scale. Axions are expected to be copiously produced in stellar cores, escape and carry away amounts of energy from the star. Therefore they constitute an energy dissipation mechanism which affects their evolution and sets bounds in the axion mass and coupling. Axions might be created in reactions taking place inside the sun. The average energy of the expected axion solar flux is calculated equal to 4.2 keV. Depending on their density and mass, they may constitute a candidate for the cold dark matter in the universe.

CERN Axion Solar telescope (CAST) is an astroparticle experiment at CERN running since 2003 and its main purpose is the search for axions. The detection technique is based on the Primakoff effect. Inside a strong electric and magnetic field the coupling of two photons could lead to an axion production and vice versa the axion couples with a virtual photon producing a real detectable photon. The main component of CAST is a 10-meter LHC prototype magnet, with a twin aperture that reaches a magnetic field of 8.8 T. The magnet is placed on a moving platform and can be moved up to $\pm 8^\circ$ vertically and $\pm 40^\circ$ horizontally. The magnet can track the sun 90 minutes during sunrise and sunset. The remaining hours are dedicated to background measurements.

In the first phase the experiment operated with vacuum inside the magnet bores, thus exploring the axion mass range up to 0.02 eV. In order to extend CAST sensitivity to higher axion masses, the magnet bores were filled with a buffer gas, at first with ^4He and then with ^3He . For the first time, the limit entered the QCD axion model band and the KSVZ line was crossed. In the third phase of the experiment ^4He was used in order to revisit the results of phase two, with improved sensitivity and longer exposure time. During the fourth phase, CAST took data with vacuum in the magnet pipes using for the first time sub-keV detectors. CAST has made a first dedicated sub-keV search for solar chameleons based on the Primakoff effect.

CAST has completed the search for solar axions. Searches are now focused on relic axions using the haloscope technique. Up to now haloscope searches have used solenoid magnets to provide the magnetic field with cylindrical cavities. In the case of CAST, rectangular cavities will be inserted inside the dipole magnet. The conversion probability is significantly enhanced if it occurs in a cavity resonant to the energy of the ALP. To cover a wide range of axion masses a tuning mechanism will be used for different frequencies.

In the first chapter a brief introduction on axions and their properties is presented. A description of the various subsystems and the results of the experiment are included in chapter 2. Chapter 3 refers to the data acquisition system and the control systems in CAST. This chapter includes detailed description of the Slow Control, the Solar Tracking Software and the Horizontal laser check program. The properties of the Silicon Drift Detector, which was installed in the experiment in 2013 and it is currently used in the CAST laboratory, are presented in chapter 4. The final chapter contains a description of the microwave cavities that will be installed in the magnet in the upcoming months.

Keywords: Axions, CP violation, Peccei-Quinn symmetry, Primakoff effect, CAST experiment, dark matter, data acquisition, X-ray fluorescence, semiconductor detectors, silicon drift detector, microwave cavities

ΕΘΝΙΚΟ ΜΕΤΣΟΒΙΟ ΠΟΛΥΤΕΧΝΕΙΟ
Σχολή ηλεκτρολόγων μηχανικών & μηχανικών Η/Υ

Περίληψη

Το πείραμα CAST στο CERN

Η εισαγωγή της γωνίας θ στη λαγκρανζιανή της κβαντικής χρωμοδυναμικής ως λύση στο $U(1)_A$ πρόβλημα υποδηλώνει την παραβίαση της συμμετρίας φορτίου-ομοτιμίας στις ισχυρές αλληλεπιδράσεις. Το φαινόμενο αυτό ωστόσο δεν παρατηρείται, γεγονός που οδηγεί στο ισχυρό πρόβλημα φορτίου-ομοτιμίας. Από πειραματικά αποτελέσματα, η ηλεκτρική διπολική ροπή του νετρονίου και επομένως η γωνία θ έχει τιμή τάξεις μεγέθους μικρότερη από την αναμενόμενη. Μια προτεινόμενη λύση συμπεριλαμβάνει μια νέα συμμετρία, την Peccei-Quinn συμμετρία, η παραβίαση της οποίας προβλέπει την ύπαρξη ενός Nambu-Goldstone μποζονίου, του αξιονίου. Τα χαρακτηριστικά του σωματιδίου αυτού, η μάζα και η σταθερά ζεύξης του, είναι αντιστρόφως ανάλογα της κλίμακας f_a στην οποία γίνεται η παραβίαση. Τα αξιόνια αναμένεται να παράγονται στους πυρήνες αστερών, να διαφεύγουν και να αποτελούν βασικό μηχανικό απώλειας ενέργειας, επηρεάζοντας την εξέλιξη των άστρων. Επομένως, αστροφυσικοί και κοσμολογικοί περιορισμοί θέτουν όρια στην μάζα και την σταθερά ζεύξης των αξιονίων. Το σωματίδιο αυτό πιθανόν να παράγεται και σε αντιδράσεις που διαδραματίζονται στον ήλιο. Η μέση ενέργεια της αναμενόμενης ροής αξιονίων υπολογίζεται στα 4.2 keV. Ανάλογα με την πυκνότητα και την μάζα τους, αποτελούν υποψήφιους της ψυχρής σκοτεινής ύλης.

Το πείραμα CERN Axion Solar telescope (CAST) είναι ένα αστροσωματιδιακό πείραμα στο CERN το οποίο αναζητά από το 2003 αξιόνια. Η τεχνική ανίχνευσης που εφαρμόζεται στηρίζεται στο φαινόμενο Primakoff. Εντός ισχυρού ηλεκτρικού και μαγνητικού πεδίου η αλληλεπίδραση δύο φωτονίων μπορεί να οδηγήσει σε παραγωγή αξιονίων και αντιστρόφως η αλληλεπίδραση ενός αξιονίου με ένα δυναμικό φωτόνιο σε ανιχνεύσιμο φωτόνιο. Το κύριο συστατικό μέρος του πειράματος είναι ένας διπολικό μαγνήτης 10 μέτρων, με μαγνητικό πεδίο 8.7 T. Ο μαγνήτης είναι τοποθετημένος σε κινητή πλατφόρμα που επιτρέπει την κίνηση του $\pm 8^\circ$ στην κάθετη και $\pm 40^\circ$ στην οριζόντια κατεύθυνση. Ο μαγνήτης ακολουθεί τον ήλιο 90 λεπτά κατά την διάρκεια της ανατολής και της δύσης, ενώ οι υπόλοιπες ώρες αφιερώνονται σε μετρήσεις υποβάθρου.

Στην πρώτη φάση του πειράματος, με κενό εντός του μαγνήτη, οι έρευνες απέκλεισαν μάζες αξιονίων έως 0.02 eV. Για μεγαλύτερες μάζες αξιονίων, προστέθηκε αέριο εντός του μαγνήτη, αρχικά ^4He και στη συνέχεια ^3He . Για πρώτη φορά, οι έρευνες εισήλθαν εντός της θεωρητικά αναμενόμενης περιοχής και υπερκαλύφτηκε ένα μέρος της περιοχής του μοντέλου KSVZ. Στην τρίτη φάση του πειράματος, επαναλήφθηκαν οι μετρήσεις με ^4He , προκειμένου να αναθεωρηθούν τα αποτελέσματα της δεύτερης φάσης με αυξημένη ευαισθησία των ανιχνευτών και περισσότερες μετρήσεις. Κατά τη διάρκεια της τέταρτης φάσης, με κενό εντός του μαγνήτη, χρησιμοποιήθηκαν για πρώτη φορά ανιχνευτές ευαίσθητοι σε sub-keV ενέργειες και έγιναν οι πρώτες έρευνες για ηλιακούς χαμαιλέοντες.

Το CAST ολοκλήρωσε τις έρευνες ηλιακών αξιονίων και επικεντρώνεται στην αναζήτηση κοσμικών αξιονίων. Σε αντίθεση με τα υπόλοιπα πειράματα στα οποία γίνεται χρήση ενός σωληνοειδούς μαγνήτη με κυλινδρικές κοιλότητες, στο CAST ορθογώνιες κοιλότητες θα τοποθετηθούν στο εσωτερικό του διπολικού μαγνήτη. Η πιθανότητα μετατροπής ενός αξιονίου σε φωτόνιο μεγιστοποιείται όταν η συχνότητα συντονισμού της κοιλότητας είναι ίση με την ενέργεια του αξιονίου. Προκειμένου οι έρευνες να επεκταθούν σε ένα ευρύ φάσμα μαζών απαιτείται η χρήση ενός μηχανισμού απαραίτητου για το συντονισμό της κοιλότητας σε διαφορετικές συχνότητες.

Στο πρώτο κεφάλαιο γίνεται μια σύντομη εισαγωγή στα αξιόνια και στις ιδιότητες τους. Μια περιγραφή των επιμέρους υποσυστημάτων του πειράματος καθώς και τα αποτελέσματα του παρουσιάζονται στο κεφάλαιο 2. Το κεφάλαιο 3 αναφέρεται στα συστήματα λήψης δεδομένων και τα συστήματα ελέγχου του πειράματος. Στο κεφάλαιο αυτό περιλαμβάνονται αναλυτικές περιγραφές των πιο βασικών λογισμικών που επιβλέπουν τα υποσυστήματα του πειράματος καθώς και την κίνηση του μαγνήτη. Οι ιδιότητες του ανιχνευτή ολίσθησης πυριτίου, που τοποθετήθηκε στο πείραμα το 2013 και πλέον χρησιμοποιείται στο εργαστήριο του πειράματος, παρουσιάζονται στο κεφάλαιο 4. Στο τελευταίο κεφάλαιο περιλαμβάνεται η περιγραφή των μικροκυματικών κοιλοτήτων που θα τοποθετηθούν στο εσωτερικό του μαγνήτη τους επόμενους μήνες.

Λέξεις κλειδιά: Αξιόνια, παραβίαση φορτίου-ομοτιμίας, συμμετρία Peccei-Quinn, φαινόμενο Primakoff, πείραμα CAST, σκοτεινή ύλη, σύστημα λήψης δεδομένων, ανίχνευση ακτίνων-X, ημιαγώγιμοι ανιχνευτές, ανιχνευτής ολίσθησης πυριτίου, μικροκυματικές κοιλότητες

Contents

Acknowledgements	iii
Abstract	v
1 Axions in QCD	1
1.1 Theoretical aspects of QCD	1
1.1.1 The $U(1)_A$ problem	1
1.1.2 Strong CP violation	2
1.1.3 The Peccei-Quinn symmetry and the axion	3
1.1.4 Axion properties	4
Coupling to matter	4
Axion Models	5
Astrophysical & Cosmological constraints	6
Axion as dark matter candidate	6
1.2 Solar axion detection techniques	7
2 The CAST experiment	11
2.1 Introduction	11
2.2 Subsystems of the experiment	11
2.2.1 The magnet	11
2.2.2 The cryogenics	11
2.2.3 The quench system	12
2.2.4 The vacuum system	12
2.2.5 The gas system	13
2.3 CAST results	14
3 Controls and acquisition systems in CAST	17
3.1 Introduction	17
3.2 The Slow Control of CAST	18
3.2.1 Introduction	18
3.2.2 Hardware	18
3.2.3 Software presentation and Main Panel	22
The block diagram	22
The Front Panel	27
3.2.4 Signals, alarms and upgrades	36
3.3 Horizontal laser check upgrade	38
3.3.1 Introduction	38
3.3.2 Software presentation	39
3.3.3 Analysis of data	40
3.4 Magnet Movement control system	42
3.4.1 Hardware	42

3.4.2	The Solar tracking program	46
3.4.3	Upgrade of the communication system	49
4	Silicon Drift Detector System	55
4.1	Introduction	55
4.2	X-ray spectroscopy	55
4.2.1	Introduction	55
4.2.2	X-ray fluorescence	55
4.2.3	Interaction of photons with matter	56
4.2.4	X-ray beam line	58
4.3	Silicon Drift Detector	60
4.3.1	Properties of semiconductor materials	60
4.3.2	Characteristics of semiconductor detectors	62
4.3.3	Silicon Drift Detector (SDD)	63
4.3.4	Nuclear Instrumentation	66
	Preamplifier	66
	Spectroscopy Amplifier	68
	Multichannel Analyzer (MCA)	69
	Digital Pulse Processor	70
4.3.5	Signal acquisition using a Digital Pulse Processor (DPP)	70
4.3.6	Upgrade of signal acquisition using a Spectroscopy Amplifier	73
4.3.7	Comparison of signal acquisition systems	76
	Background noise	76
	X-ray peaks	78
4.3.8	Conslusions	78
5	Future prospects	83
5.1	Microwave cavities for axion detection	83
5.1.1	Introduction	83
5.1.2	Haloscope operating principle	84
5.1.3	Rectangular cavities in the CAST dipole magnet	87
	Cavities and tuning mechanism	87
	Electronics	87
	Bibliography	89

List of Figures

1.1	The Primakoff effect inside the solar core (left) which leads to the production of axions and the inverse Primakoff effect in a magnetic field (right) [20]	7
1.2	Differential solar axion flux at Earth [22]	8
2.1	The magnetic field in a dipole magnet	12
2.2	The CAST magnet	12
2.3	A simplified scheme of the movement system	13
2.4	The vacuum system of CAST [30]	13
2.5	The exclusion regions in the $m_a - g_{\alpha\gamma}$ plane achieved by CAST in phase I and II [26]	15
3.1	A)The Slow Control B)The Solar tracking and C)The horizontal lasercheck .	17
3.2	Flow diagram of the components of the data acquisition system [31]	18
3.3	The delta sigma ADC and its delta sigma modulator used in the PCI-4351 NI cards [32]	20
3.4	The flow diagram of the delta sigma modulator	21
3.5	The sigma delta modulator in the frequency domain [32]	21
3.6	Analog input circuit of the PCI-6225 NI card	22
3.7	Flow diagram of the first set of loops that are executed when the SC starts running	23
3.8	Flow diagram of the second set of loops that are executed to establish communication between the software and the cards.	25
3.9	Flow diagram of the main loops of the SC.	26
3.10	The range for the acquisition of the reference points for the vertical movement (left) and for the horizontal movement (right). The value stored is the value acquired when both the magnet is moving in the range specified and the laser is on.	27
3.11	The main panel of the Slow Control	29
3.12	The tab which includes all the information about the data taking from the cards	30
3.13	The active channels of the analogue cards DAQ 1-3	31
3.14	Configuration of the PCI-6225 analogue and digital card.	33
3.15	The data acquired from the analogue cards before the calibration	34
3.16	The active channels of the digital cards	35
3.17	The horizontal motor encoders as a function of time for the years 2014-2016 as saved from the SC	37
3.18	The flow diagram of the horizontal motor check program	39
3.19	The main tab of the program	40
3.20	The encoder reference positions as a function of time for every checkpoint and for every mode	40
3.21	The tab Information & Communication of the software	41

3.22	The histogram of the 2015 tracking data	42
3.23	The histogram of the 2015 non-tracking data	42
3.24	The standard deviation of the gaussian of each reference point for tracking and non tracking data of 2015	43
3.25	The difference of the tracking and not tracking data for 2014 (black) and 2015 (red)	43
3.26	The 2014-2015 difference of mean values of each reference point for all the data (black) and for the tracking data (red)	44
3.27	The 2014-2015 difference of mean values of each reference point for all the data (black) and for the tracking data (red)	44
3.28	The frequency converter used in the CAST area.	45
3.29	The flow diagram of the system rectifiers-inverters and motors.	46
3.30	The rectifier circuit of the frequency converter [35].	46
3.31	a) The highest and lowest voltages in the three-phase full-wave rectifier with diodes and b)the output voltage [35].The highest of the three phase voltages is connected to the load at any given instant while the lowest is connected to the other end of the load.	47
3.32	A simplified scheme of the inverter circuit [36].	47
3.33	Switch positions and Voltage $U + RS$ for a pulse number equal to five [36].	48
3.34	The PWM output of the inverter. The frequency and the voltage are simultaneously controlled so that the ratio V/f is constant [35].	48
3.35	The new 9 pin SUB-D connectors that allow the transition from the old to the new system.	50
3.36	The connection of the new system with the RS485 to Ethernet converter.	50
3.37	Previous communication system consisting of an RS485 to RS 232 converter	51
3.38	New communication system consisting of a RS 485 to Ethernet converter.	51
3.39	The Horizontal movement of the magnet as a function of time for the actual solar tracking of 2014 (blue) and for the fake tracking of 2016 with the new communication system (red)	52
3.40	The Vertical movement of the magnet as a function of time for the actual solar tracking of 2014 (blue) and for the fake tracking of 2016 with the new communication system (red)	52
3.41	The Vertical encoders subtracted by the fitting as a function of time for the actual solar tracking of 2014 (blue) and for the fake tracking of 2016 with the new communication system (red)	53
3.42	The Horizontal encoders subtracted by the fitting as a function of time for the actual solar tracking of 2014 (blue) and for the fake tracking of 2016 with the new communication system (red)	53
4.1	The electromagnetic spectrum.	55
4.2	The X-ray fluorescence process. An electron from a specific shell is ejected from the atom and a vacancy is created. This vacancy is filled by an electron of an outer shell and through this process a characteristic X-ray is emitted [37].	56
4.3	The X-ray spectrum of Copper with a Nickel filter.The bremsstrahlung and the superimposed X-ray peaks K_{a1} and K_{a2} at 8.0478 keV with relative intensity 100 and 8.0278 keV with relative intensity 51 respectively can be seen.	57
4.4	Interaction mechanisms of photons with matter according to the energy of the incident beam and the Z of the material [38].	58

4.5	The power supplies of the X-ray beam line.	59
4.6	The vacuum system of the X-ray beam line [30].	60
4.7	The Fermi distribution function. [39].	61
4.8	The variation of a) the energy gap on the left and b) of the average energy for electron-hole pair production on the right as a function of temperature of silicon. [39].	61
4.9	The energy gap of semiconductors. The average energy necessary for the creation of an electron-hole pair is equal to 3.66 eV. For most gases the average energy required for electron-ion pair production is equal to 30 eV. As temperature increases electrons are able to move to the conduction band. [39].	62
4.10	Sideward depletion [42].	64
4.11	The potential in a) the drift region and b) in the region close to the anode where the electrons are directed towards the surface [42].	64
4.12	Operating principle of Silicon Drift Detector [43].	65
4.13	Quantum efficiency of Silicon Drift Detector [44].	66
4.14	Vacuum and shielding system of Silicon Drift Detector [44].	67
4.15	The Pulse Height analysis system [37].	67
4.16	The electronic circuit of a differentiator [39].	68
4.17	The electronic circuit of CR-RC shaping [39].	69
4.18	A schematic of a analog pulse processor consisting of a CR-RC-RC electronic circuit [45].	69
4.19	Schematic of an ideal digital pulse processor [45].	70
4.20	The shaped pulse and the output pulse of the differentiator in a) an analog pulse shaper in the left and b) in a Digital Pulse Processor in the right [45].	71
4.21	The differentiator output of a) an analog shaper on the left and b) a digital shaper on the right as a function of the rising time. For the analog shaper higher rising time leads to lower amplitude of the rise edge of the pulse and therefore loss of the actual amplitude of the preamplifier's signal [45].	71
4.22	Flow diagram of the readout system of the SDD using a Digital Pulse Processor	72
4.23	FWHM versus energy of the SDD [44].	72
4.24	Comparison of the spectrum acquired from the run of the detector immediately after being cooled down with the data obtained after 3, 7, 21 and 25 hours later. The increasing drop of the count rate with time indicates a C_3H_6 film deposition on its surface. [44].	73
4.25	The drop in transmission due to the increasing deposition of the hydrocarbon film on the surface of the detector, for each energy bin, at the energy range of interest (400-1500 eV) [44].	74
4.26	Comparison of the spectrum acquired from the start of the run of the detector with the spectrum obtained after 3,7,21 and 24 hours with the preamplifier board out of vacuum. No increasing drop of count rate is observed with time.	74
4.27	The transmission of the detector for each energy bin as a function of time indicates that no loss of efficiency is observed with the preamplifier outside of vacuum.	75
4.28	The flow diagram of the readout system using a spectroscopy amplifier and a MCA	75

4.29	Fitting and background rejection of the spectrum acquired from Manganese target with EPIC filter for Gaussian pulse shaping and for A) $0.5\mu s$ shaping time B) $6\mu s$ shaping time	76
4.30	Fitting and background rejection of the spectrum acquired from Manganese target with EPIC filter for Triangular pulse shaping and for A) $0.5\mu s$ shaping time B) $6\mu s$ shaping time	76
4.31	Fitting and background rejection of the spectrum acquired from Titanium target with EPIC filter for Gaussian pulse shaping and for A) $0.5\mu s$ shaping time B) $6\mu s$ shaping time	76
4.32	Fitting and background rejection of the spectrum acquired from Titanium target with EPIC filter for Triangular pulse shaping and for A) $0.5\mu s$ shaping time B) $6\mu s$ shaping time	77
4.33	Full Width at Half Maximum as a function of the Shaping Time constant for A) Aluminium target with Aluminium Filter B) Titanium target with EPIC filter C) Copper target with Nickel filter and D) Manganese target with EPIC filter	77
4.34	Noise rate of each 100 eV bin for the range of 400-1500 eV using the spectroscopy amplifier.	78
4.35	Noise rate of each 100 eV bin for the range of 400-1500 eV using the PX5.	78
4.36	Fitting and background reduction for the Aluminum spectrum acquired using the PX5 system.	79
4.37	Fitting and background reduction for the Copper spectrum acquired using the PX5 system.	79
4.38	Fitting and background reduction for the Aluminum spectrum acquired using the spectroscopy amplifier for Triangular shaping mode with $1\mu s$ shaping constant	80
4.39	Fitting and background reduction for the Copper spectrum acquired using the spectroscopy amplifier for Triangular shaping mode with $1\mu s$ shaping constant.	80
4.40	FWHM as a function of the energy of each characteristic peak for the data of 2015 and 2016 for the two readout systems. A higher FWHM is observed in 2016 with the preamplifier outside vacuum resulting to a worse resolution, which can be attributed to the longer distance between the detector and the preamplifier.	81
5.1	Existing bounds for ALPs. Achieved and expected limits in black and green respectively [46].	83
5.2	A rectangular cavity	84

List of Tables

3.1	Reference encoder values for the vertical movement	28
3.2	Reference encoder values for the horizontal movement	28
3.3	Vacuum pressure signals acquired from DAQ 1	36
3.4	Signals acquired from DAQ 2 concerning the load, the temperature and the current	36
3.5	The vacuum pressure signals acquired from DAQ 3	37
3.6	The list of alarms sent by the SC	38
4.1	The available targets in the X-ray generator and the values of their characteristic peaks in the spectrum	59

List of Abbreviations

AC	A lternating C urrent
ADC	A nalog to D igital C onverter
AFS	A n <i>dr</i> ew F ile S ystem
AlGaAs	A luminium G allium A rsenide
ALP	A xion L ike P article
C.L	C onfidence L evel
CAST	C ERN A xion S olar T elescope
CCD	C harge- C oupled D evice
CP	C harge P arity
DAQ	D ata A c <i>q</i> uisition
DC	D irect C urrent
DAC	D igital to A nalog C onverter
DE	D ark E nergy
DFSZ	D ine F ischles S rednicki Z hitnitskii
DM	D ark M atter
DPP	D igital P ulse P rocessor
D-SUB	D - SUB miniature
ENC	E quivalent N oise C ancellation
FWHM	F ull W idth at H alf M aximum
GaAs	G allium A rsenide
HB	H orizontal B ranch
HFET	H eterostructure F ield- E ffect T ransistor
HMET	H igh E lectron M obility T ransistor
JFET	J unction gate F ield- E ffect T ransistor
KSVZ	K im S hifman V ainshtein Z acharov
KWISP	K inetic W eaky I nteracting S lim P articles
LabView	L aboratory V irtual I nstrument E ngineering W orkbench
LED	L ight E mitting D iode
LEP	L arge E lectron P ositron collider
LHC	L arge H adron C ollider
MCA	M ulti C hannel A nalyzer
MFB	M agnetic F eed B ox
NI	N ational I nstruments
PC	P ersonal C omputer
PCI	P eripheral C omponent I nterconnect
PLC	P rogrammable L ogic C ontroller
PWM	P ulse- W idth M odulation
QCD	Q uantum C hromo D ynamics
RGB	R ed G iant B ranch
RMS	R oot M ean S quare

SC	S low C ontrol
SDD	S ilicon D rift D etector
SNR	S ignal to N oise R atio
TE	T ransverse E lectric
TPC	T ime P rojection C hamber
TTL	T ransistor to T ransistor L ogic
URL	U niform R esource L ocator
WD	W hite D warf

Chapter 1

Axions in QCD

1.1 Theoretical aspects of QCD

QCD is the $SU(3)$ quantum field theory of the standard model that describes strong interactions observed between quarks and gluons. Each of the six flavors of quarks, u, d, s, c, b and t has an additional quantum number called color which has three possible values: Red (R), green (G) and blue (B). There are 8 force carriers in QCD, G^a , a strong gauge coupling g_s and a strong fine structure $a_s = g_s^2/4\pi$. As opposed to weak interactions, Charge-Parity symmetries are not violated in QCD, giving rise to the strong CP problem [1].

1.1.1 The $U(1)_A$ problem

The strong interactions are described by a Lagrangian which is invariant under a group of local transformations:

$$L_{QCD} = \sum_n \bar{q}_n (\gamma^\mu i D_\mu - m_n) q_n - \frac{1}{4} G_{\mu\nu}^a G_a^{\mu\nu} \quad (1.1)$$

where:

n is the quark flavor

q_n is the quark field

γ^μ are the Dirac matrices

m_n is the quark mass

$G_{\mu\nu}^\alpha$ is the field tensor of gluons with a color index $\alpha=1,2..8$

In the limit of vanishing quark masses there is an apparent symmetry of the Lagrangian. For $m_n \rightarrow 0$ the equation (1.1) is invariant under a global symmetry $G = U(n)_R \times U(n)_L$. This limit is satisfied by the relatively small masses of up and down quarks leading to a $U(2)_L \times U(2)_R$ symmetry. The $U(1)_v$ subgroup of the $U(2)_L \times U(2)_R$ symmetry:

$$q_n \rightarrow e^{ia} q_n \quad (1.2)$$

is an exact symmetry in QCD and it corresponds to the conservation of the baryon number.

Massless fermion fields exhibit chiral symmetry, a symmetry to left-handed and right handed rotations as follows:

$$q_L \rightarrow e^{i\theta_L} q_L \text{ and } q_R \rightarrow q_R \parallel q_R \rightarrow e^{i\theta_R} q_R \text{ and } q_L \rightarrow q_L \quad (1.3)$$

Massive fermions do not exhibit chiral symmetry. Therefore, for the same limit $m_n \rightarrow 0$ there is an approximate chiral symmetry, $SU(2)_L \times SU(2)_R$ often denoted as $SU(2)_A$ which expresses the invariance of the quark kinetic energy terms:

$$\bar{q}_n \gamma^\mu i D_\mu q_n = \bar{q}_L \gamma^\mu i D_\mu q_L + \bar{q}_R \gamma^\mu i D_\mu q_R \quad (1.4)$$

In the limit of $m_u = m_d$ a further $SU(2)_v$ symmetry would arise, the isospin. Although the vectorial part of the symmetry $SU(2)_v \times SU(2)_A \times U(1)_v$ is a good approximate symmetry of nature, the axial part is not valid for the vacuum state due to a Bose-Einstein condensate of the quark fields [2, 3]:

$$\langle \bar{u}u \rangle = \langle \bar{d}d \rangle \neq 0 \quad (1.5)$$

This spontaneously broken symmetry gives rise to a triplet of light pseudo-Goldstone bosons, the pions. Furthermore, there is a forth symmetry $U(1)_A$ expressed as:

$$q_L \rightarrow e^{i\alpha} q_L, \quad q_R \rightarrow e^{-i\alpha} q_R \quad (1.6)$$

However, no Nambu-Goldstone boson exists for the violation of that symmetry, leading to the $U(1)_A$ -problem [4]. The lightest candidate would be the η with a mass of 958 MeV, however the mass of the corresponding boson is bounded by $\sqrt{3}m_\pi \approx 225 \text{ MeV}$.

1.1.2 Strong CP violation

The solution to the $U(1)_A$ problem came through the realization that $U(1)_A$ is not a true symmetry of QCD, although the Lagrangian is symmetrical under the associated transformation for vanishing quark masses. This is due to a more complicated QCD vacuum that requires the presence of a phase parameter θ with arbitrary values between 0 and 2π , adding an extra term L_θ to the Lagrangian [2, 3]:

$$L_\theta = \theta \frac{g^2}{8\pi^2} G_{\mu\nu}^a \bar{G}_a^{\mu\nu} \quad (1.7)$$

where:

g is the coupling constant

$G_{\mu\nu}^a$ is the gluon field tensor

The θ vacuum, the ground state is a result of a superposition of n-vacua:

$$|\theta\rangle = \sum_n e^{-in\theta} |n\rangle \quad (1.8)$$

After adding the electroweak interaction to the angle θ :

$$\bar{\theta} = \theta + \theta_{weak} = \theta + \text{arg}(\det M) \quad (1.9)$$

M is the matrix of the quark masses

and the Lagrangian transforms into:

$$L_{QCD} = L_{pert} + L_{\bar{\theta}} \quad (1.10)$$

With the additional term the Lagrangian is not invariant under CP transformation. CP symmetry is expected to be violated both in weak and strong interactions, however the latter has not been observed. The neutron electric dipole moment is associated with the θ angle as follows:

$$d_n \approx 8.2 \times 10^{-16} \bar{\theta} e \text{ cm} \quad (1.11)$$

The existing strong bound on the neutron electric dipole moment [5]:

$$d_n < 3 \times 10^{-26} e \text{ cm} \text{ (90\% C.L)} \quad (1.12)$$

sets an upper limit to $\theta < 10^{-10}$. Therefore, θ , a free parameter from 0 to 2π , must have a really small value and this is known as the strong CP problem [6].

1.1.3 The Peccei-Quinn symmetry and the axion

The Peccei-Quinn symmetry constitutes the most elegant solution to the CP problem [7, 8]. Instead of the static θ angle, a new symmetry U(1) is introduced. This symmetry is necessarily spontaneously broken and the Nambu-Goldstone boson is the axion. Under the $U(1)_{PQ}$ transformation the axions field $a(x)$ translates into:

$$a(x) \rightarrow a(x) + a f_a \quad (1.13)$$

where:

f_a is a parameter associated with the breaking of the symmetry

The Lagrangian becomes:

$$L_{QCD} = L_{pert} + L_{\theta} + L_a \quad (1.14)$$

where:

$$L_a = L_{kinetic} + L_{int} + L_{axion-gluon} \quad (1.15)$$

where:

$L_{kinetic}$ is the kinetic energy term

L_{int} is the term that represents further interactions of the axion

$L_{axion-gluon}$ is the axion field and its coupling with gluons

The expected axion field $\langle a \rangle$ for the vacuum is equal to:

$$\langle a \rangle = \frac{f_a \bar{\theta}}{C_a} \quad (1.16)$$

where:

f_a is the energy scale of the spontaneous breaking of the PQ symmetry

C_a is a model dependent parameter

Thus, for any value f_a the angle $\bar{\theta}$ is canceled, giving a solution to the strong CP problem

1.1.4 Axion properties

The properties of the axions depend on the energy scale of the spontaneous breaking of the Peccei-Quinn symmetry as follows [9]:

$$m_a \propto \frac{1}{f_a} \text{ and } g_{ai} \propto \frac{1}{f_a} \quad (1.17)$$

where:

f_a is the energy scale of the spontaneous braking of the PQ symmetry

m_a is the axion mass

g_{ai} is the coupling constant with the i particle

Coupling to matter

Axions can interact with gluons, photons and fermions. The coupling with gluons is the third term described in equation 1.15 and it can be expressed as [9]:

$$L_{axion-gluon} = \frac{a_s}{8\pi f_a} a G_{\mu\nu}^a \bar{G}_a^{\mu\nu} \quad (1.18)$$

where:

a_s is the strong fine-structure constant

Axions can acquire mass through their interaction with gluons by mixing with pions, which can be calculated by the expression:

$$m_a = \frac{m_\pi f_\pi}{f_a} \sqrt{\frac{z}{(1+z+w)(1+z)}} \simeq 6 \text{ meV} \frac{10^9 \text{ GeV}}{f_a} \quad (1.19)$$

where:

m_π is the pion mass equal to 135 MeV

f_π is the pion decay constant

z is the ratio m_u/m_d

w is the ratio m_u/m_s

The coupling of axions with photons is expressed as [10]:

$$L_{a\gamma} = g_{a\gamma} \vec{E} \vec{B} a \quad (1.20)$$

where:

α is the axion field

\vec{E} is the electric field

\vec{B} is the magnetic field

$g_{\alpha\gamma}$ is the axion-photon coupling constant which is calculated as:

$$g_{\alpha\gamma} = \frac{a}{2\pi f_a} C_\gamma \quad (1.21)$$

α is the fine structure constant

C_γ is a model dependent coefficient

The coupling constant of axions with fermions can be calculated as:

$$g_{af} = \frac{C_f m_f}{f_a} \quad (1.22)$$

m_f is the mass of the fermion

C_f is a model dependent coefficient

In particular, in the case of axion-electron and axion-nucleon coupling respectively:

$$g_{ae} = \frac{C_e m_e}{f_a} \text{ and } g_{aN} = \frac{C_N m_N}{f_a} \quad (1.23)$$

Axion Models

Coupling of axions with other particles is strictly model dependent. At first, it was thought that the violation of Peccei-Quinn symmetry took place in the electroweak scale $f_a \simeq 250\text{GeV}$ with masses greater than 150keV, strongly interacting with baryonic matter and radiation. However, this axion model, the visible axion model, has not been observed and was ruled by astrophysical limits [11, 12]. As a result, f_a must have a higher value than the electroweak scale leading to the invisible axion models. Two types of models have been postulated, the KSVZ (Kim-Shifman-Vainshtein-Zakharov) and the DFSZ (Dine-Fischles-Srednicki-Zhitnitskii). In both models the axions is light and weakly interacting with matter.

KSVZ model: According to this model [13, 14], axions couple only with gluons and they do no interact with fermions and quarks. The only particle that carries PQ charge has to be a new heavy quark Q and the ratio E/N is equal to:

$$\frac{E}{N} = 6Q_{heavy}^2 \quad (1.24)$$

Q_{heavy} is the electric charge of the new heavy quark with possible values $Q_{heavy} = -1/3, 1, 0$

E/N is the ratio of the electromagnetic to color anomalies with common values $E/N = 0, 2, 6$ for the KSVZ model

DFSZ model: In this model no further quarks are introduced [15]. The PQ charge is carried by fermions, however a fine tuning is needed in order to obtain a scale of breaking of the symmetry larger than the electroweak scale. In this case $E/N = 8/3$.

Astrophysical & Cosmological constraints

The strong CP problem does not define the breaking scale f_a and thus the axion mass is arbitrary. However, axions can be produced in environments like the ones of stars, clusters and white dwarfs, setting constraints to the axion mass limit [9].

Globular clusters A globular cluster is defined as a group of 10^6 stars. The Red Giant Branch (RGB) stars have degenerate helium burning core and hydrogen burning shell. When the temperature and the density increases, a higher fusion rate is observed and the stars become Horizontal Branch stars (HB). It is expected that the HB stars lose more energy through the production of axions via the Primakoff effect and thus less HB stars than RGB should be observed. As a result, the axion to photon coupling is constrained to $g_{a\gamma} \lesssim 10^{-10} GeV^{-1}$. Furthermore due to axion emission through electron-Bremsstrahlung processes in RGB stars, the brightness of the star in case of high helium core losses should be increased. From observations of the globular cluster M5 a new limit to the axion-electron coupling is set, equal to $g_{ae} < 4.7 \times 10^{-13} GeV^{-1}$ [16].

White dwarf cooling Low-mass stars at the end of their life transform into white dwarfs made of a helium burning shells and degenerate carbon-oxygen core. The temperature of WD gradually decreases due to the emission of neutrinos, photon and also axion emission created by axion-Bremsstrahlung processes. From the cooling of the ZZ Ceti Star a limit for the axion-electron coupling is obtained equal to $g_{ae} < 1.3 \times 10^{-13} GeV^{-1}$ [17].

Supernova 1987 A When a massive star burns its carbon-oxygen core, heavier nuclei are produced and the core size is increased. When the Chandrasekhar limit is exceeded, a stellar explosion takes place accompanied by a huge flux of neutrinos and radiation.

Axions can be produced through a Bremsstrahlung axion-nucleon coupling in a core of a type-II SN. As a result, the duration of the burst is affected. As the coupling constant increases the burst duration decreases until it reaches a minimum value. After that point with a higher coupling constant the axions are trapped and cannot escape. The SN 1987 A gave the first limit for axion-nucleon coupling $3 \times 10^{-10} \lesssim g_{aN} \lesssim 3 \times 10^{-7}$

The cosmological and astrophysical constraints on invisible axions allow a window for the axion mass [9, 17]:

$$10^{-6} eV \leq m_a \leq 10^{-3} eV \quad (1.25)$$

Axion as dark matter candidate

The baryonic matter only accounts for the 4.2% of the Universe, the 27.2% is dark matter and the rest 68.9% is Dark Energy, responsible for the accelerated expansion of the universe. However, the composition of DM and DE is still unknown.

DM is composed by electrically neutral and weakly interacting particles. Axions are DM candidates, as they could have been thermally produced in the primordial plasma and

although being light particles they are not relativistic [11]. The life time of an axion can be calculated as [18]:

$$\tau_a \approx 4.6 \times 10^{40} s \left(\frac{E}{N} - 1.95 \right)^2 \left(\frac{f_a/N}{10^{10} GeV} \right)^5 \quad (1.26)$$

From equation 1.26 $\tau_a > t_0$ where t_0 is the age of the Universe.

1.2 Solar axion detection techniques

There are multiple detection techniques used for axion searches such as photon regeneration experiments, polarization experiments and haloscopes [19]. The sun constitutes a possible source of axions and the research program of CAST has been focused on the detection of solar axions with a helioscope experimental setup. The Primakoff effect implies a coupling of pseudoscalar particles with two photons which is observed in the decay of π_0 [20]. For an axion interaction with two photons the form of the Lagrangian is [21]:

$$L_{\alpha\gamma\gamma} = \frac{-1}{4} g_{\alpha\gamma} F_{\mu\nu} \tilde{F}^{\mu\nu} \alpha = g_{\alpha\gamma} \vec{E} \vec{B} \alpha \quad (1.27)$$

$F_{\mu\nu}$ is the electromagnetic field-strength tensor

$\tilde{F}^{\mu\nu}$ is the dual of the electromagnetic tensor

α is the axion field

$g_{\alpha\gamma}$ is the coupling constant

\vec{E} is the electric field

\vec{B} is the magnetic field

In figure 1.1 the conversion of the axion into a photon in the electric field of a charged particle is shown

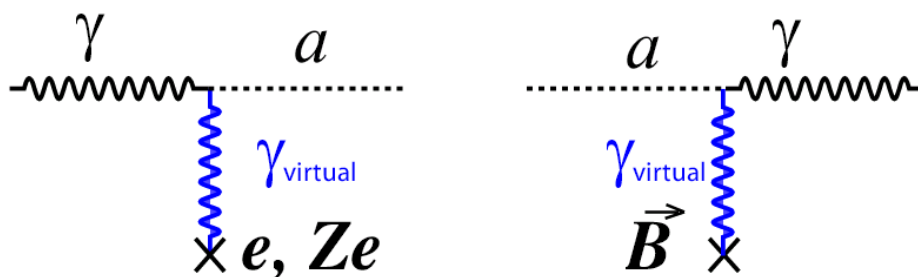


FIGURE 1.1: The Primakoff effect inside the solar core (left) which leads to the production of axions and the inverse Primakoff effect in a magnetic field (right) [20]

The solar axion flux from the sun is expected to be equal to [21]:

$$\frac{d\Phi_\alpha}{dE} = 6 \times 10^{10} cm^{-2} s^{-1} keV^{-1} g_{10}^2 E^{2.481} e^{\frac{-E}{1.205}} \quad (1.28)$$

Φ_α is the axion flux

$$g_{10} = g_{\alpha\gamma\gamma}/10^{-10}$$

The spectrum has a peak at 3 keV and a mean energy of 4.2 keV (figure 1.2).

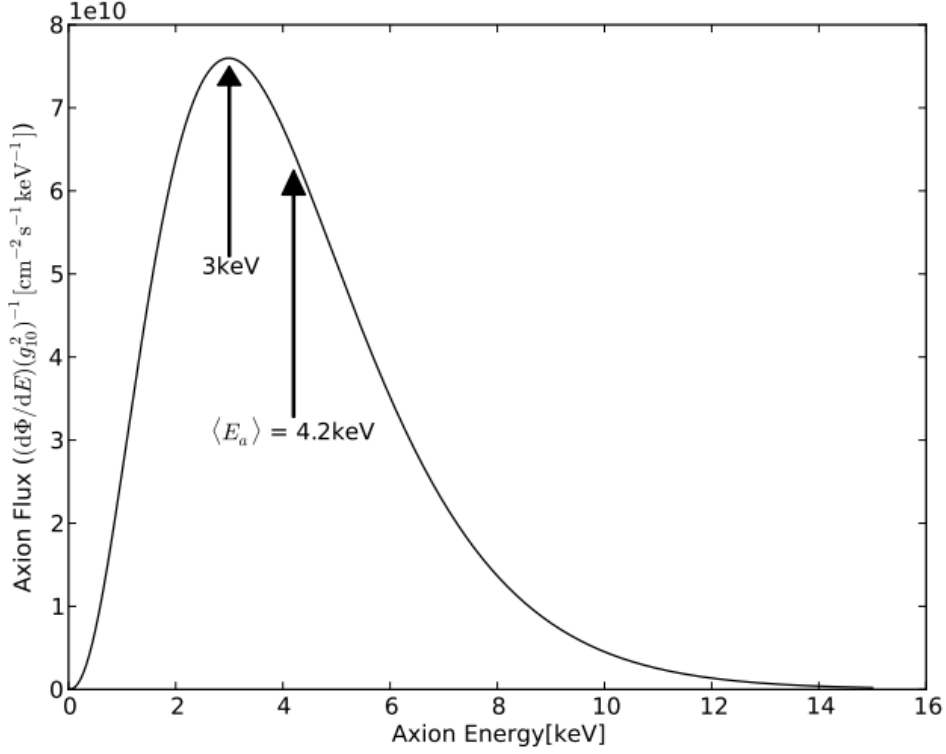


FIGURE 1.2: Differential solar axion flux at Earth [22]

The probability of the axion-photon conversion in a magnetic field is equal to:

$$P_{a \rightarrow \gamma} = \left(\frac{g_{\alpha\gamma}}{2}\right)^2 B^2 \frac{1}{q^2 + \Gamma^2/4} [1 + e^{-\Gamma L - 2e^{-\Gamma L/2}} \cos(qL)] \quad (1.29)$$

where:

$g_{\alpha\gamma}$ is the coupling constant

B is the magnetic field

γ is the inverse absorption length

L is the effective length

q is the momentum transfer between axions and the photons in the medium which can be calculated as:

$$q = \left| \frac{m_\gamma^2 - m_\alpha^2}{2E_a} \right| \quad (1.30)$$

In the case of vacuum the absorption term is equal to zero and equation 1.2 takes the form:

$$P_{a \rightarrow \gamma} = \left(\frac{g_{\alpha\gamma} BL}{2} \right)^2 \left(\frac{\sin\left(\frac{qL}{2}\right)}{\left(\frac{qL}{2}\right)} \right)^2 \quad (1.31)$$

The effective mass of the photon can be considered zero and the momentum transfer is simplified to:

$$q = \frac{m_\alpha^2}{2E_a} \quad (1.32)$$

For values of $qL < 2\pi$ the probability is maximized within the limit:

$$m_\alpha < \sqrt{\frac{4\pi E_\alpha}{L}} \quad (1.33)$$

For searches in the higher axion mass region the conversion length can be filled with a buffer gas. While traversing the medium, the massless photons exhibit an effective mass which is equal to:

$$m_\gamma = \sqrt{\frac{4\pi\alpha n_e}{m_e}} \quad (1.34)$$

n_e is the electron density of the buffer gas and can be calculated from the expression:

$$n_e = N_A \frac{Z}{W} p \quad (1.35)$$

where Z and W are the atomic number and the atomic weight of the gas respectively, N_A is the Avogadro's number and p the density of the gas. For $q = 0 \Rightarrow m_\alpha = m_\gamma$ the coherence is restored.

Chapter 2

The CAST experiment

2.1 Introduction

The CERN Axion Solar Telescope has been searching for axion-photon conversion from the sun's core since 2003 in SR8 at CERN. A decommissioned LHC prototype magnet is used that can track the sun for 1.5 h during sunrise and sunset [23]. The two 43mm diameter bores of the superconducting magnet reach a magnetic field of 8.8 T. At the bore ends X-ray detectors are placed in order to detect an excess of counts in the acquired spectra.

The CAST research program is divided into two phases. In the first phase the magnetic bores were under vacuum and the detectors used were a Time Projection Chamber (TPC), a Micromegas and a Charge Coupled Device (CCD) in the focal plane of an X-ray telescope [24, 25]. During the second phase the bores were filled with ^3He buffer gas [26, 27] and ^4He for searches of higher mass axions [28] and the TPC was replaced by two Micromegas. After the end of the second phase, the bores were under vacuum and the CCD was replaced by InGrid. At the moment, the detectors used in the experiment are Ingrid, KWISP and in the upcoming months microwave cavities.

2.2 Subsystems of the experiment

2.2.1 The magnet

The magnet (figure 2.2) is a LHC prototype with two straight cold bores with a 43mm diameter. It is fabricated by superconducting Niobium-Titanium windings and with a 13kA power supply a perpendicular 8.8 T magnetic field is created (figure 2.2). The 10m long magnet sits on a movable platform as can be seen in figure 2.3. The turntable platform allows a movement of $\pm 40^\circ$ horizontally and the girder supports the two jacks that move the magnet vertically $\pm 8^\circ$. The movement of the magnet will be discussed in further detail in the next chapter.

2.2.2 The cryogenics

In order to obtain a 9 T magnetic field the magnet has to be cooled down from ambient temperature to 1.9 K. The temperature reaches 4.5 K with liquid helium supplied by a cold box which was recovered from the e^+e^- collider LEP and DELPHI. The magnet is cooled down to 1.9 K through a further pumping group. Cryogenic and electrical feed to the magnet is done through the Magnet Feed Box (MFB). Seven flexible transfer lines connect the MFB to the cold box, the helium pumping group and the quench recovery system that allow the movement of the magnet without interrupting its cryogenic operation. Liquid helium from

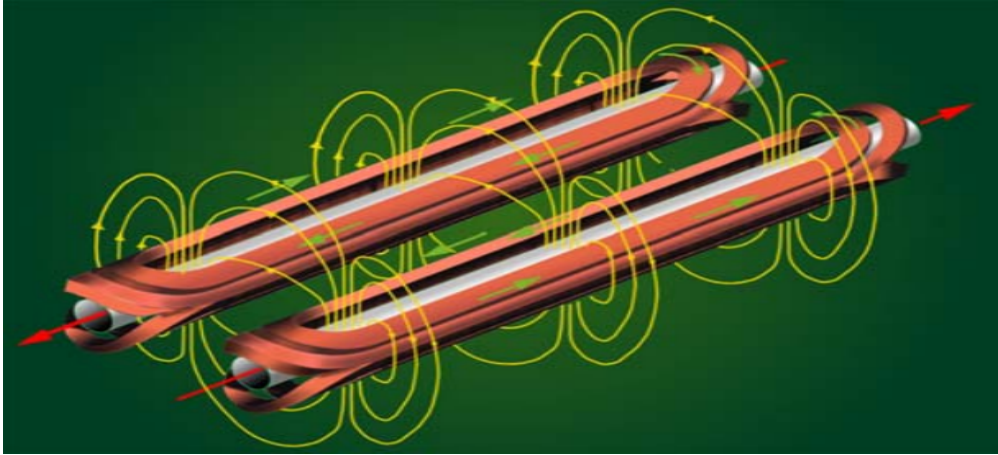


FIGURE 2.1: The magnetic field in a dipole magnet

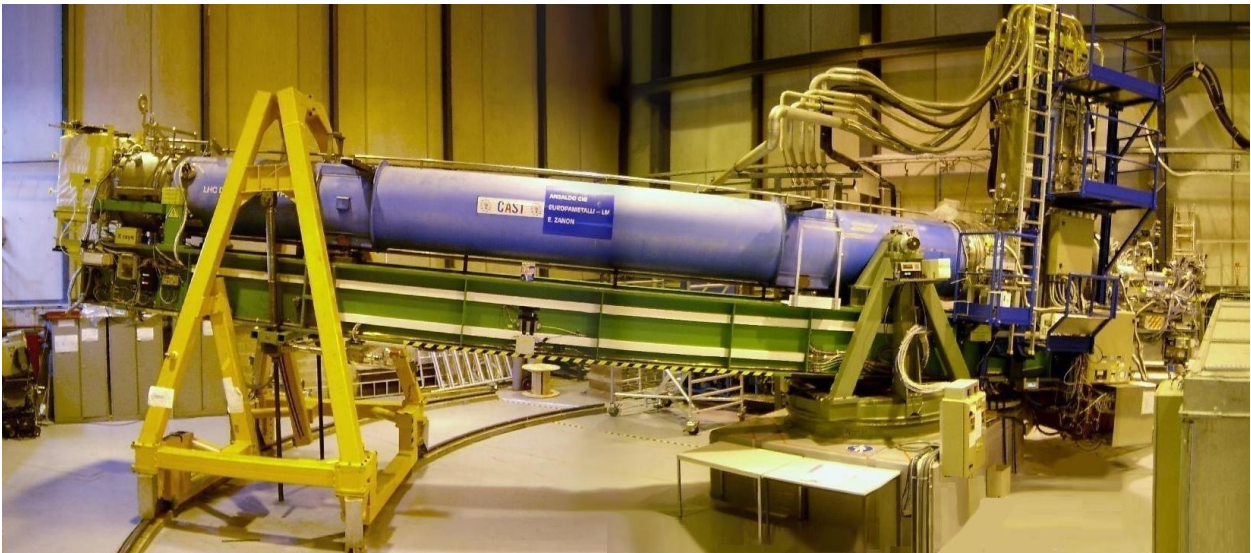


FIGURE 2.2: The CAST magnet

the 4.5 K bath is subcooled in a copper mesh heat exchanger and it is transferred along the magnet length [29]. The control system of the cryogenics is a PVSS software.

2.2.3 The quench system

In case of a resistive transition of the magnet and loss of superconductivity an emergency helium discharge occurs. In 120 ms a quench valve opens and the superfluid helium is discharged in the liquid helium buffer, where it is vaporized. The buffer is also equipped with a relief valve to the atmosphere in case that the pressure increases more than 0.12 MPa. The last measure of protection for the pressurized helium is a rupture disk with a 2 MPa pressure limit.

2.2.4 The vacuum system

The vacuum system in CAST consists of three subsystems: The cryostat vacuum, the general vacuum and the detectors vacuum (figure 2.4). The cryostat vacuum thermally

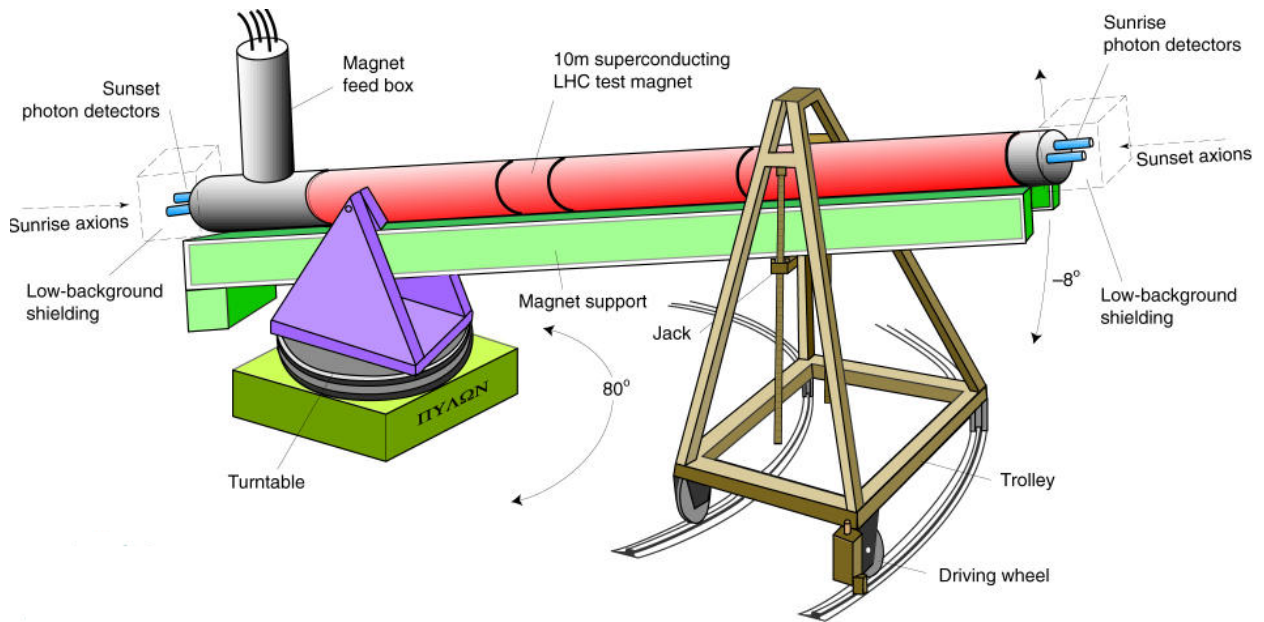


FIGURE 2.3: A simplified scheme of the movement system

isolates the magnet from the environment, while the general vacuum lines are used to pump the cold bores and the extension lines leading to the detectors. At the end of each line a gate valve is installed to isolate the magnet from the detector system. The detectors vacuum is the vacuum between each detector and the gate valve.

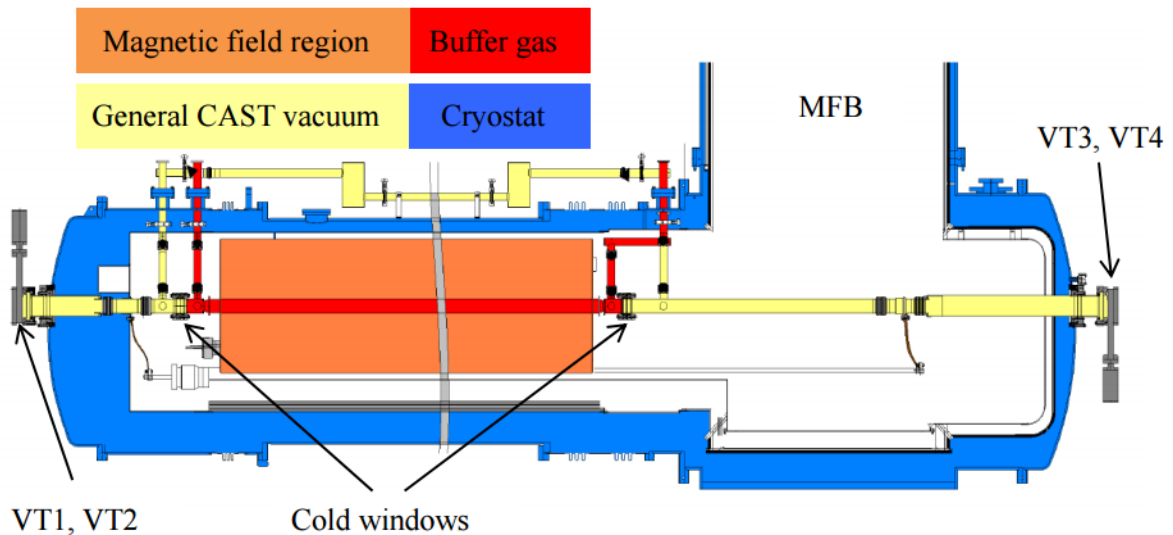


FIGURE 2.4: The vacuum system of CAST [30]

2.2.5 The gas system

Buffer gas was used inside the bores for the restoration of the coherence length and sensitivity to higher mass axions was achieved. With vacuum inside the bores the axion

masses reached were up to 0.02 eV. With the bores filled with ^4He the scanned axion masses reached 0.39eV. ^4He is saturated at 16.405 mbar at 1.8 K and therefore ^3He was introduced as a buffer gas in order to scan masses up to 1.16eV.

A specific amount of gas was inserted in small steps through a filling system. For the confinement of the gas inside the magnet four cold windows of $15\mu\text{m}$ polypropylene connected to a stainless steel strongback were installed at the end of the magnet bores. The gas system consists of the storage volume, the cleaning system, two metering volumes and the expansion volume. The gas is sent from the storage volume through the cleaning system to the metering volume. One of the metering volumes is used for a step increase in the density of the gas and the other for accurately injecting larger amounts of ^3He in the cold bores. From the metering volumes the gas is injected into the magnet. The system is controlled by a PLC which sends the signal for the gas to be transferred or recovered. In case of a quench, the magnet temperature and therefore the pressure increases and the PLC opens two electrovalves that connect the conversion volume with the expansion volume. After the quench the buffer gas is transferred back to the storage volume.

2.3 CAST results

The first phase of CAST lasted from 2003 to 2004 with vacuum in the magnet's bores. The limits achieved are [24]:

$$g_{\alpha\gamma} < 8.8 \times 10^{-11} \text{ GeV}^{-1} \text{ 95\% C.L for } m_a < 0.02 \text{ eV} \quad (2.1)$$

From 2005-2006 ^4He was used as a buffer gas. The experimental limits achieved are [28]:

$$g_{\alpha\gamma} < 2.17 \times 10^{-10} \text{ GeV}^{-1} \text{ 95\% C.L for } 0.02 < m_a < 0.39 \text{ eV} \quad (2.2)$$

In 2008 ^4He was replaced by ^3He until 2011. The KSVZ theoretical region was crossed for the first time. The limits obtained are [26]:

$$g_{\alpha\gamma} < 2.3 \times 10^{-10} \text{ GeV}^{-1} \text{ 95\% C.L for } 0.39 < m_a < 0.64 \text{ eV} \quad (2.3)$$

$$g_{\alpha\gamma} < 3.3 \times 10^{-10} \text{ GeV}^{-1} \text{ 95\% C.L for } 0.64 < m_a < 1.17 \text{ eV} \quad (2.4)$$

In 2012 the ^4He phase and in 2013 the vacuum phase were revisited with improved background levels in the detectors. The limits achieved in phase I and phase II are shown in figure 2.5.

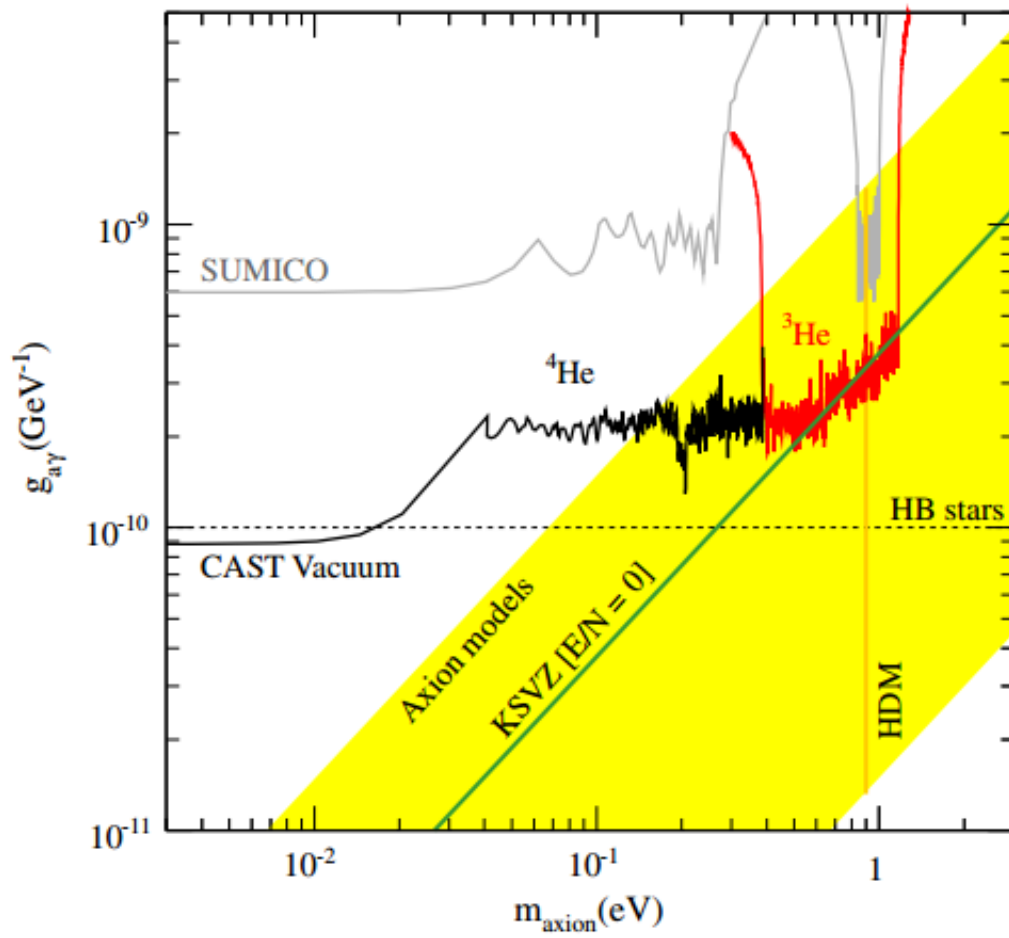


FIGURE 2.5: The exclusion regions in the $m_a - g_{\alpha\gamma}$ plane achieved by CAST in phase I and II [26]

Chapter 3

Controls and acquisition systems in CAST

3.1 Introduction

All the controls and acquisition systems in CAST are LabView based. LabView is a dataflow programming language in which execution is determined through a graphical block diagram and the front panel is used as a user interface. The most important benefit over other development environments is the direct communication with NI instrumentation hardware through a set of standard graphical nodes. The Slow Control and the Solar Tracking program are LabView based data acquisition, logging and plotting systems. A new software was installed for the online monitor of the horizontal movement of the magnet (Figure 3.1).

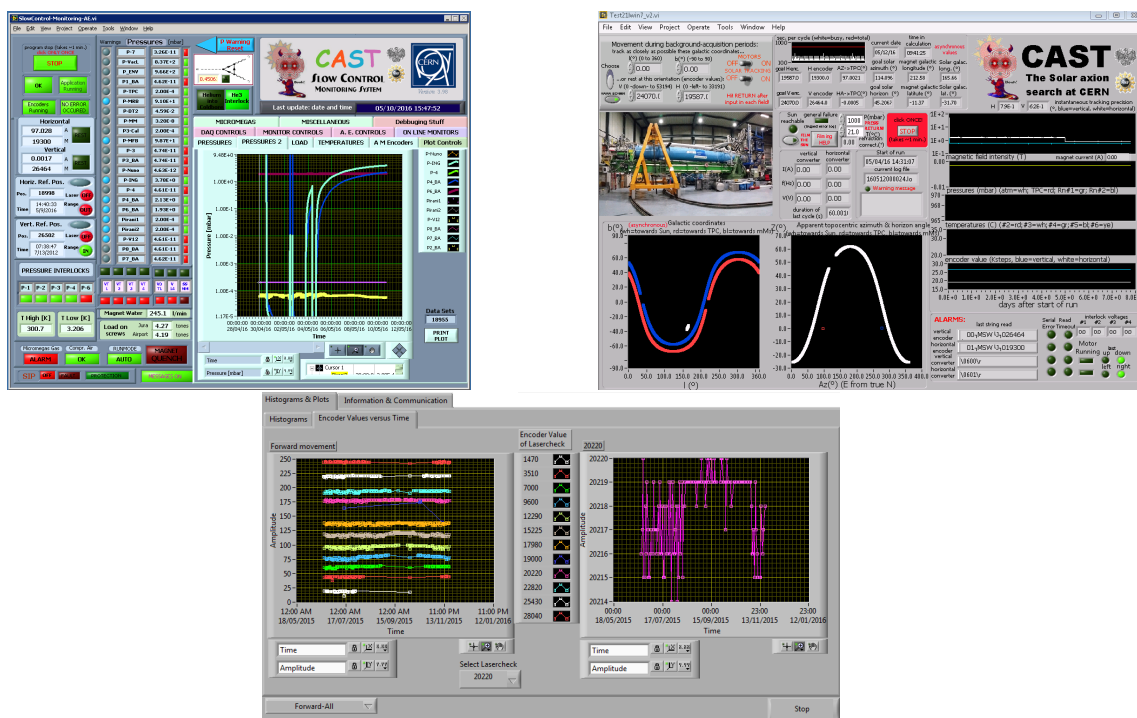


FIGURE 3.1: A)The Slow Control B)The Solar tracking and C)The horizontal lasercheck

3.2 The Slow Control of CAST

3.2.1 Introduction

The main purpose of the Slow Control involves gathering signals from measurement sources from all the subsystems of the experiment and digitizing the signals for storage and presentation on the PC. Figure 3.2 shows the operating principle of the data acquisition system. The components of the DAQ system are:

1. Transducers and sensors: The temperature, pressure and load are some of the phenomena amongst others that must be monitored. The transducers and the sensors convert those physical phenomena into electrical signals of voltage and current that can be measured by the DAQ hardware.
2. DAQ Hardware: NI analogue and digital cards are used as an interface between the signals acquired and the computer. Their main function is to digitize incoming analog signals so that they can be interpreted by the software running on the computer. They are coupled with the PC through a PCI bus architecture.
3. Driver software: It forms the middle layer between the software and the hardware so that the communication is established without complex commands. NI-DAQmx and NI 435x driver software are used for the Slow Control.
4. Software: The software is implemented in a 8.5 LabView version.

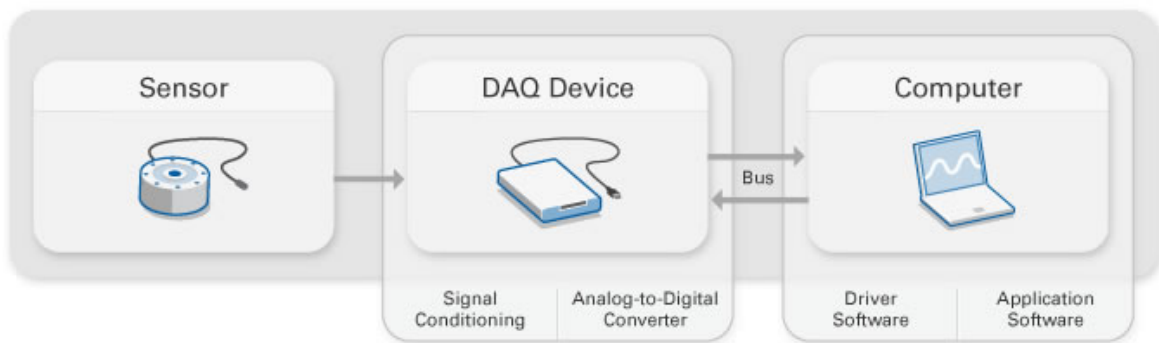


FIGURE 3.2: Flow diagram of the components of the data acquisition system

[31]

3.2.2 Hardware

The hardware of the Slow Control consists of NI boards. The DAQ interface of the cards used is the PCI bus with a bandwidth of 132MB/s, which is fast enough for the data acquisition needed and PCI slots are included in all desktops. The main component of the cards is the ADC. The resolution given refers to the number of binary level the ADC can use to represent the signal which determines what change in the input can be detectable. 16-bit resolution corresponds to $2^{16} = 65536$ discrete levels. The minimum signal change that can be detected is equal to:

$$\text{Resolution in Volts} = \frac{\text{Input range in Volts}}{2^{\text{bits}}} \quad (3.1)$$

The total amount of information in megabytes per second can be calculated as *Resolution in bytes/s* \times *Sampling rate in MS/s* \times *Number of channels*.

The Slow Control data acquisition system is formed by:

three PCI-4351 NI cards: These cards (DAQ 1-3) are high-precision temperature and voltage meters. Each one has 16 differential analog inputs and each input contains a 24-bit ADC. With the differential inputs, every input has its own ground reference and noise errors are reduced as the common noise picked up is rejected. The input ranges are up to 15V and 25 μ A. NI 4351 includes 8 TTL signal inputs and outputs, however they are not currently used.

The most important characteristic of this card is the delta sigma ADC as seen in figure 3.3a, the main purpose of which is to digitize the analog signal and reduce the noise of lower frequencies. The delta sigma ADC consists of two parts. The first part is the modulator which samples the input signal at a very high rate into a 1-bit stream and the second is the digital/decimation filter which takes this sample and converts it into high-resolution signal with a lower frequency. Therefore the input sampling rate f_s is different with the f_D output data rate. The modulator is shown in figure 3.3b and the flow diagram in figure 3.4. From the input voltage the output of the 1 bit DAC is subtracted, which has a value equal to 1 or -1. The voltage X_2 , enters the integrator where it is added to its previous values. The output X_3 is compared to the reference voltage which is zero. If X_3 is equal or greater than zero both the output and X_4 are set to 1. Otherwise, the output is equal to 0 and the DAC output to -1. Through the feedback negative loop, the output is constantly modified and if the output pulse is averaged it is equal to the value of the input signal. Therefore, higher input voltage signals will lead to an output with higher frequency of ones compared to a lower input signal. The main purpose of the modulator is the discrimination of the noise from the signal. In figure 3.5 the operating principle of the delta sigma modulator can be seen in the z domain and the output can be calculated as follows:

$$Y(z) = V(z) + E(z) \quad (3.2)$$

$$V(z) = \frac{A(z)}{1 - z^{-1}} \quad (3.3)$$

$$A(z) = X(z) + z^{-1}E(z) \quad (3.4)$$

$$Y(z) = E(z) + \frac{(X(z) - z^{-1}Y(z))}{1 - z^{-1}} \quad (3.5)$$

$$Y(z) = z^{-1}X(z) + E(z)(1 - z^{-1}) \quad (3.6)$$

where:

$Y(z)$ is the output function in the z domain

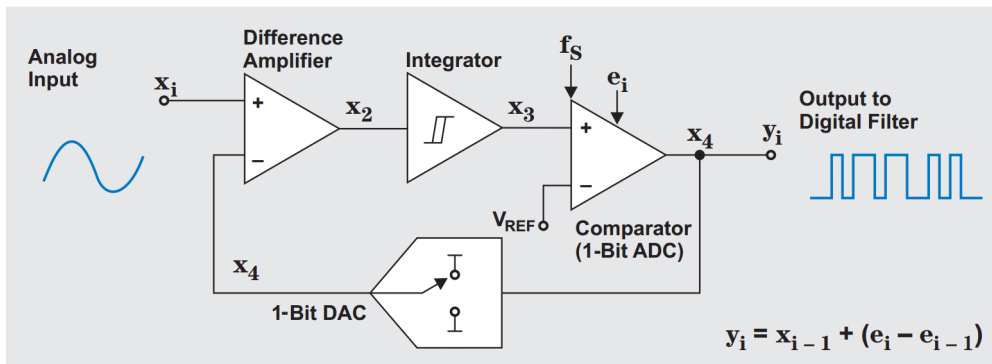
$E(z)$ is the function of the noise

$X(z)$ is the input signal in the z domain

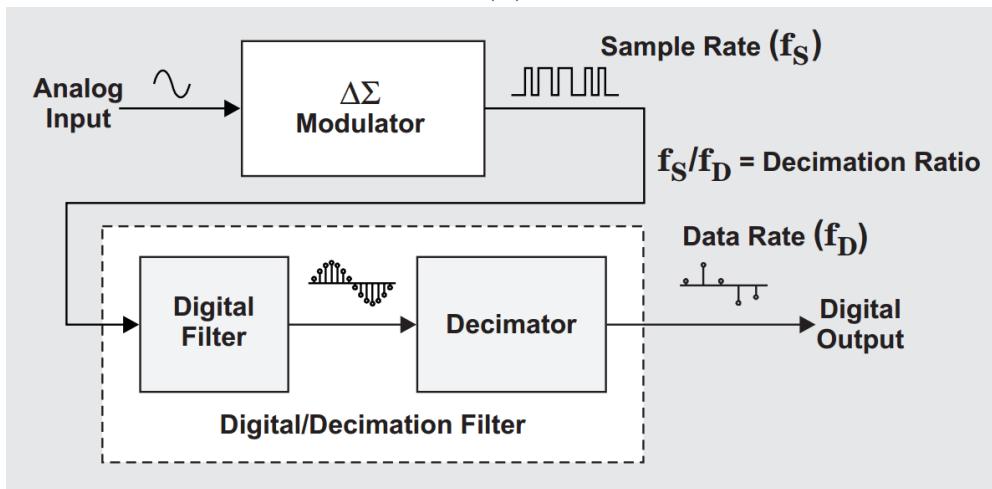
From equation 3.6 it can be seen that the input signal is not modified, apart from a delay, but the noise is powered and shifted in the frequency domain. By replacing the z transform with the Fourier transform:

$$|1 - \exp^{-j2\pi f}|^2 = |2\sin(2\pi f)|^2 \quad (3.7)$$

The output signal and noise in the frequency domain are shown in 3.5. The digital filter averages the series of logic ones and zeros and outputs multiple-bit data and the decimation filter decreases the sample rate. Therefore the digital/decimation filter acts as a low pass filter and it rejects the noise which is transferred to higher frequencies [32, 33].



(A)



(B)

FIGURE 3.3: The delta sigma ADC and its delta sigma modulator used in the PCI-4351 NI cards [32]

one PCI-6225 NI card: This card (DAQ 4) includes 40 input differential channels, each one of which contains a 16-bit ADC with a multichannel sampling rate of 250kS/s. The maximum input range is 10 V and this card also includes 24 digital channels, currently not used. The circuit of the card for analogue inputs can be seen in figure 3.6. The analog input signal is connected to the I/O connector with its ground reference. The multiplexer connects one analog channel at a time with the ADC. The Terminal Configuration Selection selects the mode of the signal which can be differential, reference single-ended and non-referenced single ended. For the Slow Control each input is connected with its reference ground and therefore the differential mode is selected. The NI-PGIA, a differential amplifier, is used as

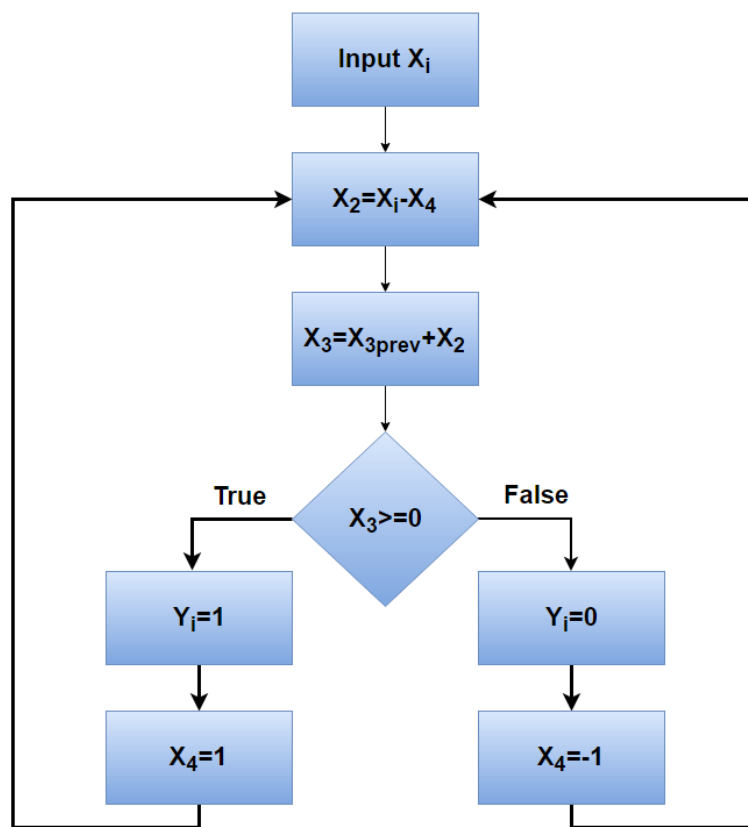


FIGURE 3.4: The flow diagram of the delta sigma modulator

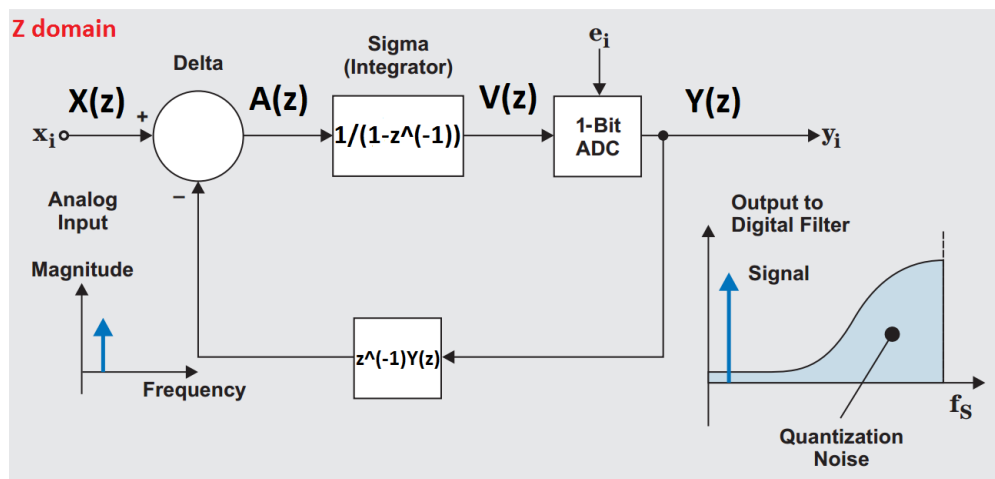


FIGURE 3.5: The sigma delta modulator in the frequency domain [32]

an interface between the signal and the ADC to ensure that the maximum resolution of the ADC is used. Then the signal enters the ADC where it is digitized and it is stored in a large FIFO buffer so that no data is lost. The lowpass filter attenuates noise beyond the cutoff frequency and enhances the signal to noise ratio [34].

one digital card PCI 6527: It includes 48 digital channels and it can sense digital levels up to 28V DC and 120 μ A.

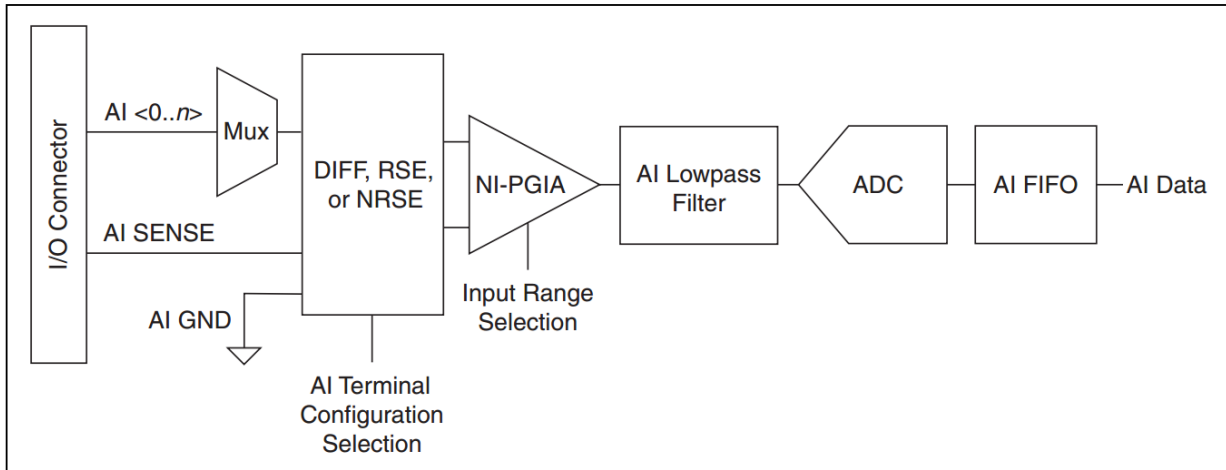


FIGURE 3.6: Analog input circuit of the PCI-6225 NI card

one digital card PCI 6528: It includes 24 digital channels and it can sense digital levels up to $60V$ DC and $150\mu A$.

3.2.3 Software presentation and Main Panel

The block diagram

The first group of commands that are executed when the program starts running are a set of essential steps which help the interface with the user, the initialization of parameters and creation of the data socket. These steps are shown in figure 3.7.

1. Dialogue VI: A message is displayed to the user when the program starts running. The user must press the START button when he has checked that all DAQ configurations are correct.
2. Tab Initialization: The tab control of the front panel is initialized in the page "DAQ controls"
3. Configuration of front panel arrays for 6225 and 6528 cards: This loop configures the information that can be seen in the cards arrays in the front panel. Each column includes the number of each channel, the name and the type. In case that the user modifies the configuration the button SORT must be pressed and the array of channels is sorted according to the channel number. This loop checks if there is a double definition of channels. If this is the case a message is displayed, otherwise the loop stops executing. The application status is set to "initialization setup" and the stuck message, the message which appears when the program does not work properly, is initialized to false.
4. Data socket: The data socket node opens a data connection with the URL specified. This loop is repeated as long as the application is running. The data socket refnum includes the names and the values of the variables transmitted. If an error occurred while trying to write to the URL specified the system execution VI is used, which forces to run an executable that will try to establish the communication with the address specified.

5. Panic Button and matching of indexes: If the user presses the panic button a dialog pop-up appears that asks the user if he actually wants to terminate the application. If the user presses OK all applications are aborted. This loop also matches the indexes of the array that includes the names of the channels with the ones of the channel number arrays and types.

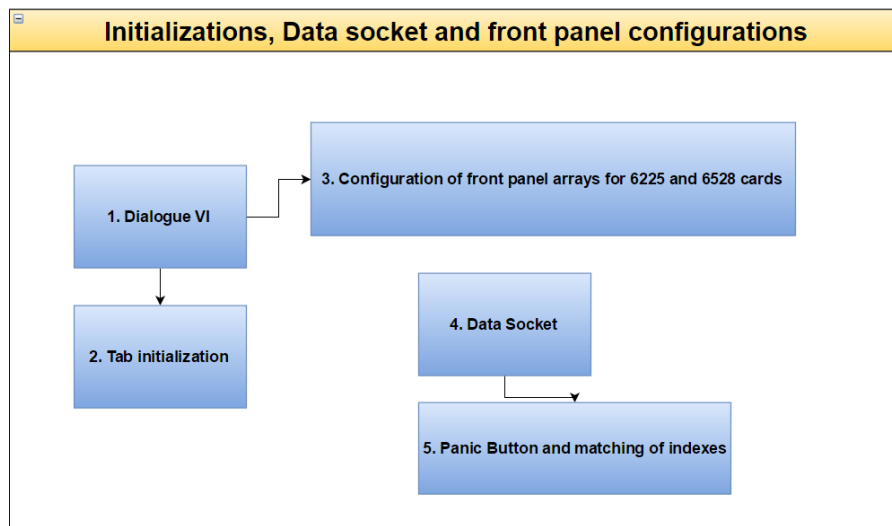


FIGURE 3.7: Flow diagram of the first set of loops that are executed when the SC starts running

The second set of loops include the communication between the program and the analogue and digital cards (figure 3.8). This step is achieved with standard procedures which are followed for the communication of the NI cards and the NI software.

1. Slow Control Self-Monitor: If the SC is not updated for two minutes or if the user pressed the Manual Reset button the cards are reset. In that case a text file is created under the name warning.txt in the debug files mentioning that the cards were reset and the time that it occurred.
2. Reading Analog Cards PCI-4351: If the PCI-4351 mode boolean button is set to true, communication is established with the three NI PCI-4351 cards. The upper and lower limits are set to 15 and -15 V respectively and the input signals are voltage signals. If the absolute value of the signal acquired is greater than 0.01 the input is accepted, the counter of each card increases and the voltage output is saved in an array for each card. The counter resets after 1000 inputs. If an error occurred during the communication with the cards an alarm is sent to all the Alarm mailing list contacts. When the application stops running the communication with the cards is closed. If the button PCI-4351 mode is set to false sine signals are simulated and they are used as inputs in the arrays previously mentioned. In that case the mode is set to Simulation Mode.
3. Reading Analog Channels from Card PCI-6225: From the configuration for the analogue channels of the 6225 card of the first sets of loop the number of active channels is calculated. If it is a non-zero number communication with the card is established. The Voltage range is set to -10 to +10 V and the sampling rate can be set by the user

using the knob in the front panel. The DC and RMS values of the input waveform are calculated and if they are greater than zero the input signal is accepted. The counter resets after 100 inputs. In case of an error an alarm is sent to the alarm mailing list.

4. Reading Digital Channels from Card PCI-6225: The digital channels of this card are not used.
5. Digital Card PCI-6527 and lasers: If the Enable Digital Output is ON the reference positions of the horizontal and vertical lasers are checked. If the magnet passes from a reference point the values of the laser variables are changed. When this event occurs the writing laser boolean button is switched to ON.
6. Reading Digital Card 6528: This digital card is only ready when the switch in the front panel is set to Read Mode. The configuration of the channels in the first set of loops for this card are checked. If the number of channels is non-zero communication with the card is established. The program does not read this card in every loop but only when a change in the channels is detected. Then the time is stored and if the alarm button is enabled then an alarm is sent to the alarm mailing list.
7. Fast Data taking: When the user presses the start fast data tracking button a specified variable can be monitored with a higher rate than the others. The user chooses the variable, presses reset and sets the rate in ms. The program detects in which DAQ this signal is detected and plotted. A new file is created in the fast logfiles every day that the program is set to fast data tacking and this file is also saved in AFS.
8. Pressures array: All the inputs from DAQ 1-4 are gathered in the same array, the indicator of which is in the front panel. The space element is deleted from the names of the pressures.

The main loops are the executed steps that create the files where the data are stored and the plots of the front panel as shown in figure 3.9. The main loops are:

1. Copy-Write file: The application status is set to Data Logging. This loop consists of a stacked sequence with 10 frames. In each frame the value of the timer is stored in order to calculate the time of execution of each step and the time difference with the previous step. This is also the loop where the Warning Reset button of the front panel is set to true when the user switches on or off one of a warning. If the Lock button in the front panel is enabled the sampling rate is locked in the value chosen by the user. The steps followed in the stacked sequence are:
 - Step 0: The program gets the current date and time from the system. If this is the first loop, which means that the program just started running it creates a new file with a year-month-day format the H directory. If it is not the first loop it creates a new file only when the day has changed. The program creates a backup copy of the file each day at 09:00 and 24:00 both in AFS and in the G directory.
 - Step 1: The program checks if the data of all the cards are available. When all the cards are properly read or if the button Skip is pressed by the user it continues to the next step.

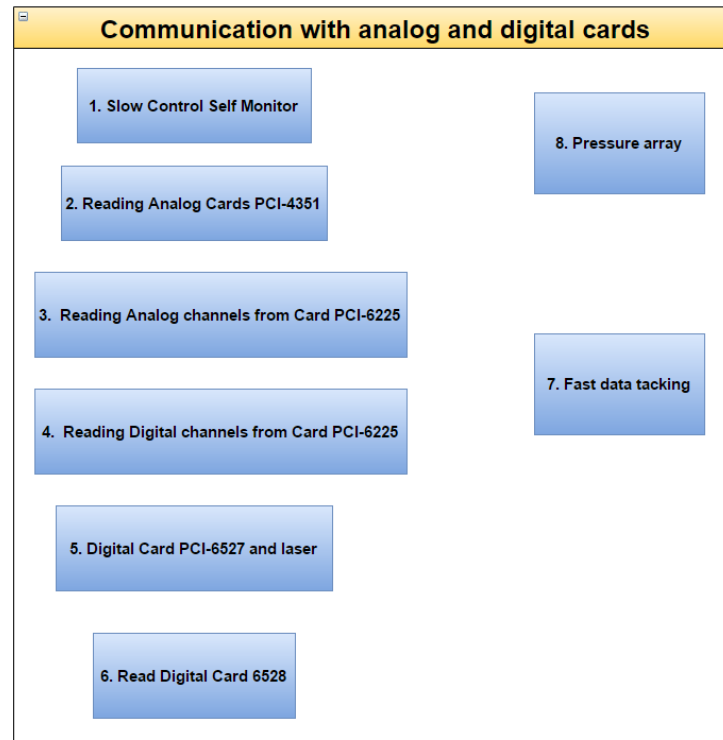


FIGURE 3.8: Flow diagram of the second set of loops that are executed to establish communication between the software and the cards.

- Step 2: The active analogue channels of DAQ 1-4 are calibrated according to their type. All the important parameters such as high and low temperature, proximity sensors values, loads and pressures are linked to an indicator in the front panel.
- Step 3, Step 4 and Step 5: All the important parameters are plotted.
- Step 6: In this step all the boolean indicators in the front panel for the digital cards are updated. At the same time the pressures from the analogue cards are checked. If there is a change of $\pm 1\%$ of the maximum change set by the user the sampling rate is increased.
- Step 7: The indicators in the front panel of the digital cards are updated. If the current of the magnet decreases it sends an alarm as a warning that a ramp down occurred or some other reason caused the current to go below 12000 A.
- Step 8: If the file was just created it adds the header with the version number of the program and the variables for the data socket are selected. The data are converted into strings and saved in the logfiles, the data send to the data socket are updated and if the file changes a new header and version number are added.
- Step 9: A delay is added to complete the cycle according to the sampling rate. The sampling rate returns to its nominal value in case it was changed due to a rapid change of the value of the pressures. item Step 10: All the pressured are checked. If one of them is out of the range set an alarm is sent to the alarm mailing list.

2. Print plots: If the user presses the print plots button the plot is printed.

3. Lasers and Encoder files: The Encoder files with the reference positions are created with a Encoder_check_Year-Month format in the H directory. Moreover, eventfiles are created with information about the active channels of the digital cards PCI-6527 and PCI-6528.
4. Encoders and angle encoders: The program communicates with the serial horizontal and vertical port of the angle encoders. The address of the Vertical serial port is 02 and the serial port is ASRL1::INSTR while the address if the horizontal one is 03 and the port is COM4. A new files is created when the program starts running or when the day has changed. In that case a buffer with all the data is emptied to the specified path in H directory. According to the previous and current value of the angle encoders the direction of movement is determined. Communication is also established with the encoders from the inverters. According to the value of the encoders the laser boolean indicators are set to true or false if they are in a specified range or not respectively and the direction of the movement is determined.
5. Save plots: If the user presses the boolean button save plots the pressure, the temperature, the load and the vertical and horizontal position plots are saved.

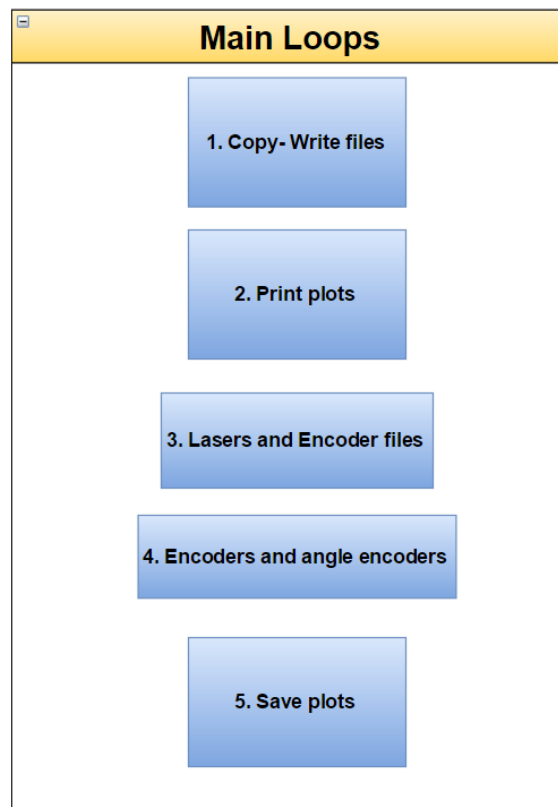


FIGURE 3.9: Flow diagram of the main loops of the SC.

The last part of the block diagram includes all the warning and alarms that are sent to the alarm mailing list. Alarms are sent when the Slow Control does not run properly for more than two minutes, in case of a quench and if the pressures, the temperatures, the compressed air and the demineralized water are out of a predefined range. Furthermore,

the Data Socket data are updated, eventfiles are created in case that a chance occurred in the channels of the digital cards and if the user exits the application the logfiles, the angle encoder files and the eventfiles are copied in AFS.

The Front Panel

The main panel of the Slow Control is shown in figure 3.11:

1. The main boolean control that the user presses to start and stop the program. When pressed, the main loops of the program stop running and the text files created are saved in AFS. This procedure requires approximately one minute to be completed.
2. The values of the angle encoders and of the encoders for the horizontal and vertical movement. When the magnet moves the LED indicator is turned ON.
3. The horizontal and vertical reference points. When the magnet crosses a specified range of values the boolean indicators Range and Laser are switched on. Figure 3.10 shows the relative encoder values when the two boolean indicators are switched on and tables 3.2 and 3.1 show the actual values specified for the vertical and horizontal movement respectively. Then the encoder value and the time are stored in the front panel (Position-Time indicators) as a reference point as well as in the Encoder check files.

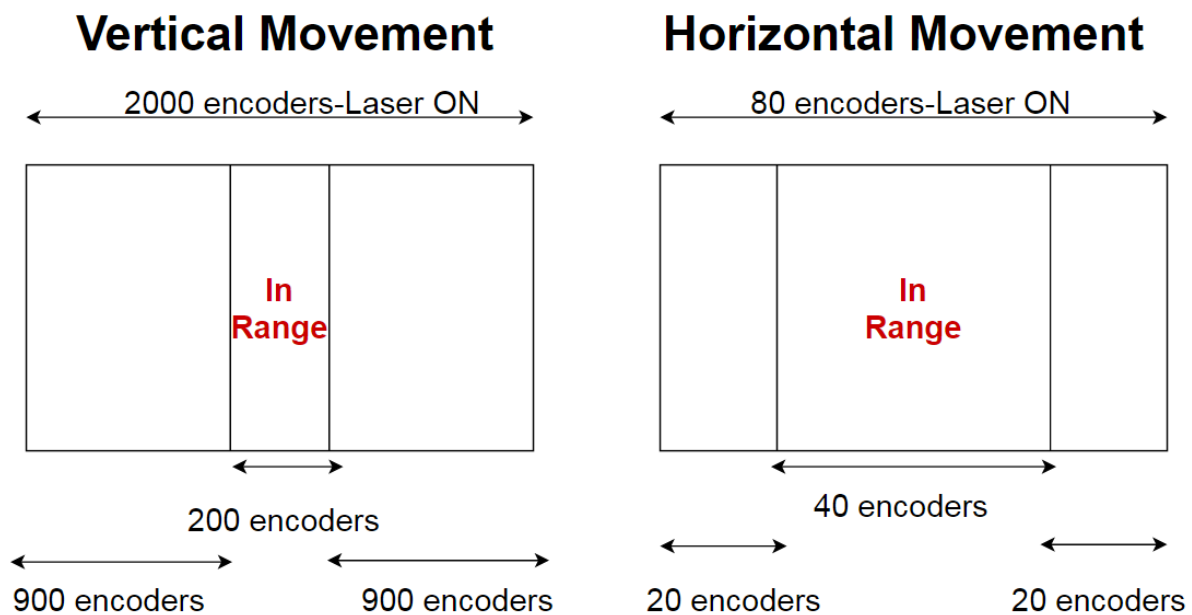


FIGURE 3.10: The range for the acquisition of the reference points for the vertical movement (left) and for the horizontal movement (right). The value stored is the value acquired when both the magnet is moving in the range specified and the laser is on.

4. The status of the pressure interlocks. These digital signals are acquired through the PCI-6527 card which reads the pressure interlocks only when a change has occurred compared to their previous status.

Vertical Movement			
Laser ON		In Range	
25492	27492	26392	26592

TABLE 3.1: Reference encoder values for the vertical movement

Horizontal Movement			
Laser ON		In Range	
1430	1510	1450	1490
3470	3550	3490	3530
6960	7040	6980	7020
9560	9640	9580	9620
12250	12330	12270	12310
15185	15265	15205	15245
17940	18020	17960	1800
18960	19040	18980	19020
20180	20260	20200	20240
22780	22860	22800	22840
25390	25470	25410	25450
28000	28080	28020	28060

TABLE 3.2: Reference encoder values for the horizontal movement

5. The temperatures of the cold bore
6. All the Warnings activated by the user
7. All the pressures acquired from DAQ 1-4
8. Warning Reset button. This button must be pressed every time that a modification in the activated list of warnings occurs.
9. The current of the magnet. If the current obtains a higher value than the threshold, which is set to 12000 the boolean indicators switches on
10. The date and the time that the Slow Control was last updated. The version number changes every time that the user modifies the program and saves a new version. The version number is saved in the Version.idx file with the header of the logfiles which include all the variables used in the newer version.
11. The status of the valves
12. The load on each side of the magnet
13. The Quench alarm status
14. The status of the valves. It can be set either to automatic or to manual
15. The alarm about the compressed air pressure

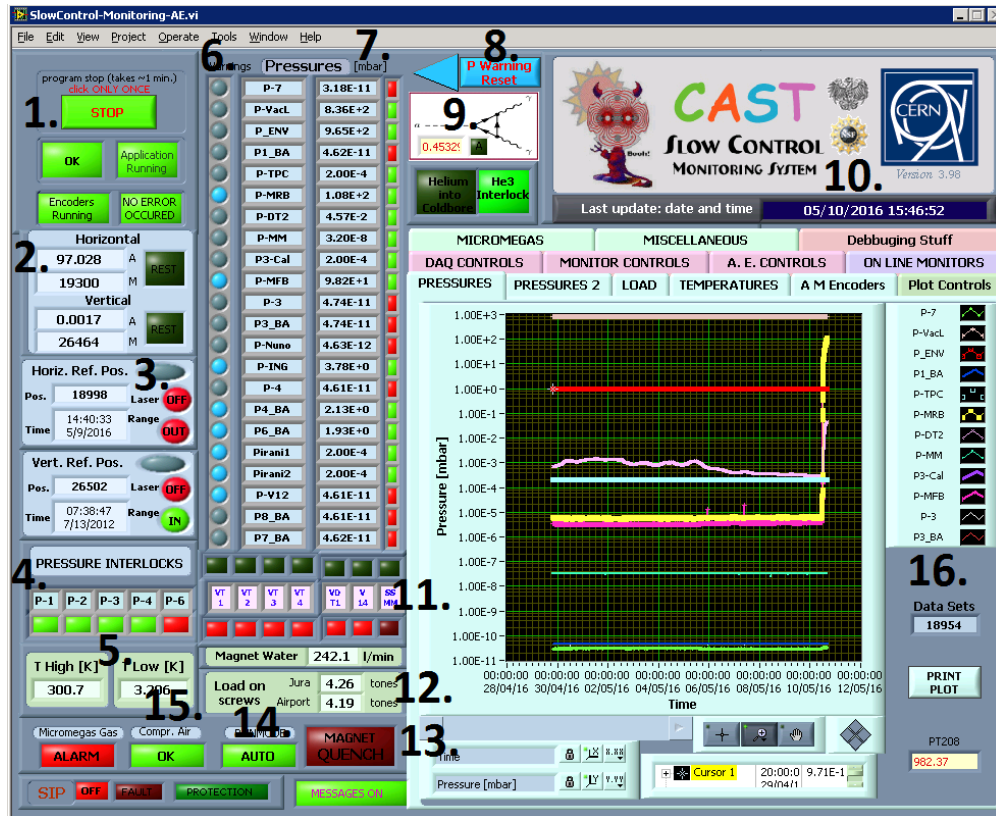


FIGURE 3.11: The main panel of the Slow Control

16. Some of the pressures plotted as a function of time. An indicator with the number of data sets included in the plot and the Print button for the user

The tab seen in figure 3.12 includes information about the data taking:

1. The application status has three modes: Initialization setup, when the program starts running and the first series of loops are executed, Data logging, when the data are stored to the files and the main loops are executed and Copying files on exit when the user presses the Stop button and the files are copied in AFS.
2. The full output path. This is the path where the logfiles are saved
3. Start of run and current date
4. The name of the current logfile
5. Data transmitted in the data socket
6. The URL of the data socket
7. The sampling rate in seconds that the data is acquired from the cards. If the Locked/Enabled control is set to Locked the user cannot change the sampling rate. If the FORCE/AUTO indicator is set to FORCE the sampling rate does not change if a sudden change in pressures occurs.

8. The percentage of maximum change of the sampling rate. If a change of the signals acquired is observed higher than the maximum change set the sampling rate increases so that the parameters are monitored more closely. The FORCE/AUTO button must be set to AUTO, otherwise the sampling rate does not change.
9. Save plots indicator. When the LED is on the plots are saved to the H directory



FIGURE 3.12: The tab which includes all the information about the data taking from the cards

In figure 3.13 the tab with the channels of the analogue cards is shown:

1. The status of the channels of the analogue cards DAQ 1-3.
2. The names, the types and the ranges of the active channels
3. The number of active channels
4. The PCI-4351 mode button. If the Run Mode is chosen the channels of the cards are read. The boolean indicators of the cards are on when the signals are properly acquired and the number of data of each card is displayed. If the Simulated mode is chosen simulations of sine signals are used as signal inputs.

The tab in figure 3.14 concerns the configuration of the PCI-6225 card with both analogue and digital signals:

1. The number of analogue channels used



FIGURE 3.13: The active channels of the analogue cards DAQ 1-3

2. The configuration of the card. The inputs is a differential continuous waveform with a voltage range from -10 to +10 V.
3. The sampling rate of the PCI-6225 card in Hz
4. The number of digital channels used. Not digital channels from that card are currently used.
5. An array with the number, the name and the type of each channel of the PCI-6225 card
6. The Sort button. After adding a channel the user must press the Sort button to sort the channel according to their number
7. Digital channels. No digital channels from this card are currently used

In figure 3.15 the data from the analogue cards before the calibration are shown:

1. Time of execution of each step of the main loop and the time difference between the steps. The time that the file was created and the time that the data are read and plotted is stored in this array.
2. The date and time of the last time that the cards were read, the timestamp and the number of days that the program has been running
3. The boolean indicator of the angle encoders data. When the data are available it switches to On

4. The Skip button and the Manual Reset. If there is no proper communication with the cards the user can press skip and the program continues to run without reading the cards. If the user presses Manual Reset the cards are reset and the program tries to establish a new communication.
5. Panic button. When the user presses this button, a dialogue window appears. If he presses OK the program is instantly aborted. In that case the files are not copied to AFS before closing the program.
6. The readouts from the analogue cards before being calibrated. In the last column the data from the digital channels of the PCI-6225 card are displayed

All the information about the digital cards are included in the tab shown in figure 3.16:

1. The active channels of the digital card. This card is read only when a change in the signals of the channels has been detected
2. The Application running indicator
3. A cluster that includes the last time that the card was read and the last three status of each channel when the change occurred (left). A cluster that includes the timestamp that the card was last read and the current and previous status of each channel.
4. List of events. The card 6527 includes all the digital signals for the lasers and the reference positions
5. The boolean indicator for the detection of a change in the signals from the card
6. Date and Time of last event
7. The active channel of PCI-6528 digital card
8. The boolean indicator for the detection of a change in the signals from the card
9. Date and Time of last event



(A)



(B)

FIGURE 3.14: Configuration of the PCI-6225 analogue and digital card.

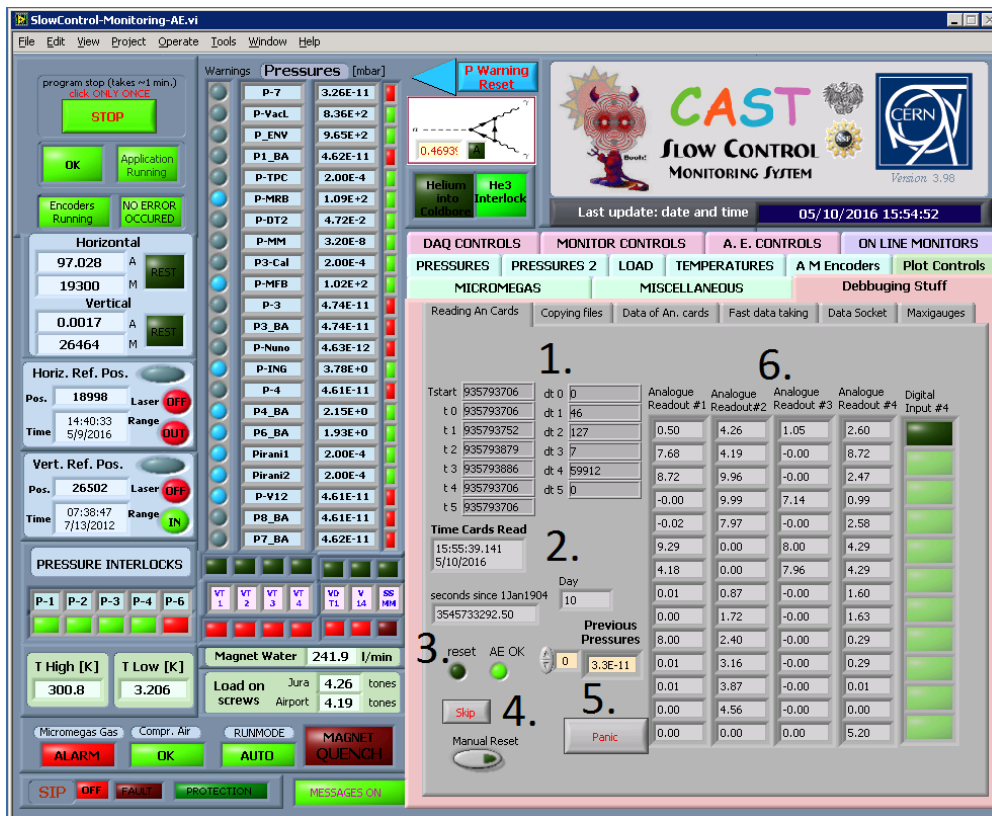
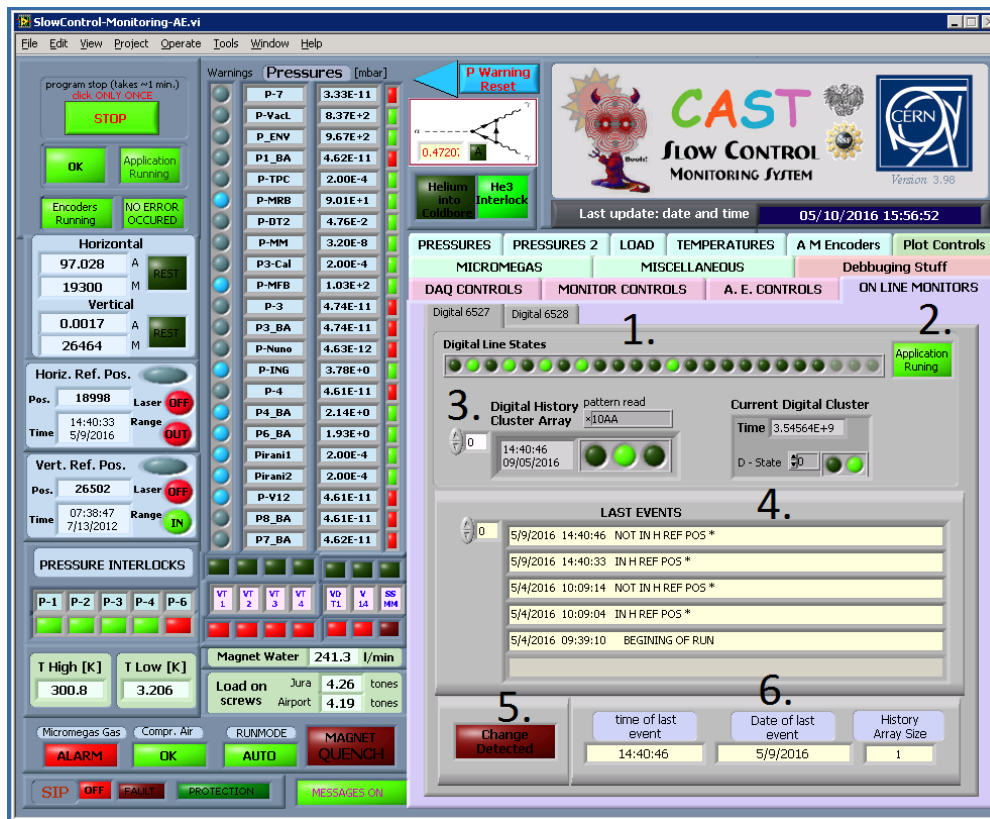


FIGURE 3.15: The data acquired from the analogue cards before the calibration



(A)



(B)

FIGURE 3.16: The active channels of the digital cards

3.2.4 Signals, alarms and upgrades

The input signals in the analogue cards can be seen in tables 3.3, 3.4 and 3.5. The values of those signals are stored in text files for further offline analysis.

DAQ 1				
Name	Type	Channel	Color	Ground
P-7	mbar	2	White	Bridge
P-VacL	mbar	3	Brown	Bridge
P-ENV	bar	4	Green	Bridge
P1'(BA)	mbar	5	Yellow	yellow green
P-TPC	mbar	6	Grey	Bridge
P-MRB	mbar	7	Pink	Brown/Pink
P-DT2	mbar	8	Pink	Grey
P-MM	mbar	9	White	Bridge
P3-Cal	mbar	10	Brown	Bridge
P-MFB	mbar	11	Green	Bridge
P-3	mbar	12	Yellow	Bridge
P3'(BA)	mbar	13	Grey	Bridge

TABLE 3.3: Vacuum pressure signals acquired from DAQ 1

DAQ 2				
Name	Type	Channel	Color	Ground
JURA LOAD	tones	2	Blue	Red
AIR LOAD	tones	3	Yellow	Green
TT868	K	4	Red	Blue
TT869	K	5	Yellow	Green
Water	L/m	6	White with label '+'	White
I_magnet	A	7	Red	White

TABLE 3.4: Signals acquired from DAQ 2 concerning the load, the temperature and the current

The signals from the analog and digital cards are not the only signals stored from the SC. The SC establishes communication with the encoder motors and the angle encoders. In figure 3.17 the Horizontal motor encoders from the logfiles of the SC are plotted as a function of time for the years 2014-2016.

In 2015 the modifications done for the SC were:

- The Horizontal frequency is added to the Encoder check files. The frequency was calculated by subtracting the previous and current horizontal encoder values of each loop and then divided by one second. For a tracking frequency of 35-40 Hz the speed is equal to 1-1.5 horizontal encoders/sec while for 150 Hz 5 horizontal encoders/sec. This information is needed for the Horizontal laser check program.
- P_{ENV} and P_{MRB} , previously read from DAQ 2, were moved to DAQ 1 due to a maxi-gauge removal. P_{ENV} replaced P_{dMM-Ss} while for P_{MRB} a new channel was activated.

DAQ 3				
Name	Type	Channel	Color	Ground
P-Nuno	bar	4	Brown	Bridge
P-CCD	mbar	5	Green	Bridge
P4'(BA)	bar	7	Grey	Bridge
P6'(BA)	bar	8	Pink	White green
PIRANI1	bar	9	White	Blue (MGRD7)
PIRANI2	bar	10	Brown	Bridge
P-V12	bar	12	Yellow	Bridge
P8_BA	bar	13	Grey	Bridge
P7_BA	bar	14	Pink	Red (MGRD9)

TABLE 3.5: The vacuum pressure signals acquired from DAQ 3

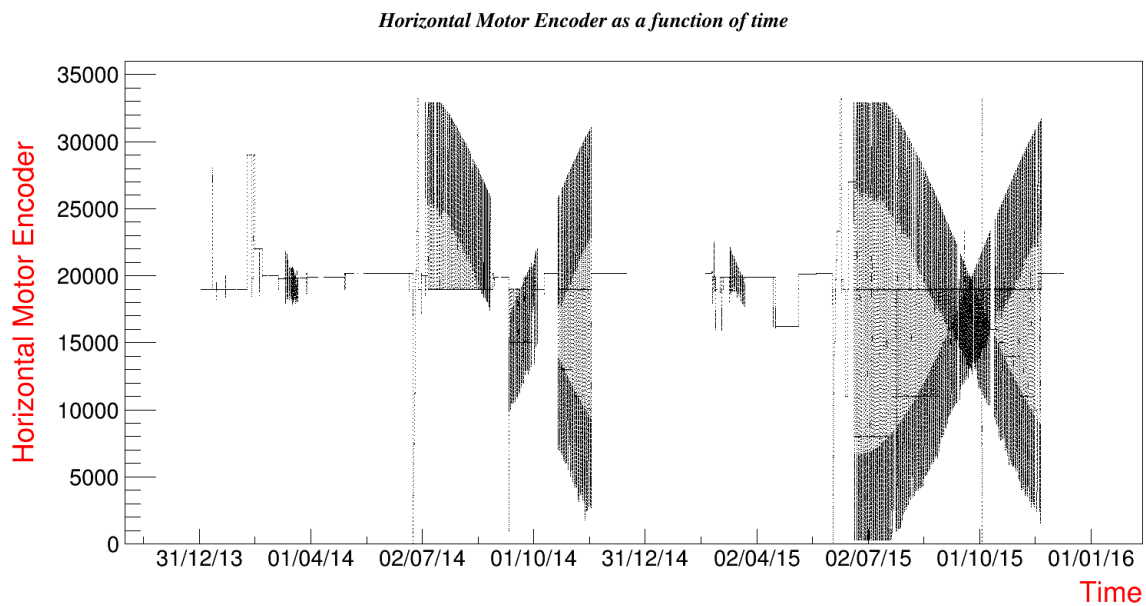


FIGURE 3.17: The horizontal motor encoders as a function of time for the years 2014-2016 as saved from the SC

- P_{CCD} was renamed to P_{ING} . The name of the variable was changed both in the logfiles and in the plots.

List of Alarms sent by the SC	
Alarm	Description
Change of status of Valve	When a digital card reads a modification in the valves status it sends alarms that inform about the new current state (OPEN/NOT OPEN) and (CLOSE/NOT CLOSE)
Change in interlock box	It includes information about the status of the pressures, the compressed air alarm and the quench alarms
Maxigauges pressures	An alarm is sent when a pressure exceeds the range defined by the user (each decade higher than 10^{-6} mbar)
Compressed Air Warning	A warning is sent when the compressed air decreases and crosses a defined value
Magnet Temperature	The first alarm is sent when the magnet temperature is above 1.9K and the second when it is above 1.95K. Both alarms are reset when the temperature drops under 1.85 K
Pressure Ingrid	Alarm is sent if the pressure increases above a certain value
Slow Control is stuck	If the SC is not working properly after 2 minutes an alarm is sent
Cards reading error	When there is no proper communication with one of the cards the SC is not working properly and a warning is sent

TABLE 3.6: The list of alarms sent by the SC

3.3 Horizontal laser check upgrade

3.3.1 Introduction

A new LabView software has been installed for the monitoring of the horizontal movement of the magnet. The correlation of the horizontal motor encoder value at the reference points provides a means to detect and measure any systematic error in the horizontal drive system such as a slippage of encoders on the belt. The operating principle of the system is based on a digital laser sensor. There are 12 reflecting spots that have been installed in the rail that allows the horizontal movement of the magnet. At the start of each check point, a beam of laser is emitted from a laser head that is attached to the horizontal drive wheel. According to the color of the target the intensity of the received light varies. The amplifier displays a maximum value when the target is the silver part of the reference point and a fluctuating value when the laser is crossing the black part of the check point. When this transition happens, the value of the encoders is sent to the SC and it is saved in the Encoder check files along with the time and the direction of movement. These files are used as an input to the program for online monitoring.

3.3.2 Software presentation

The block diagram: The description of the dataflow of the program is shown in figure 3.18. When the sampling time set by the user has elapsed, the program checks in the Encoder files directory if there is a modification in the current file. If this is the case it reads the new elements and it saves the data that concern the forward movement of the magnet in a histogram. Then, the data are grouped according to the frequency of the magnet. For frequencies above 40 Hz the new elements are saved in the histogram with the non tracking data otherwise they are stored in the histogram with the tracking data. In the next step each reference position was associated to its checkpoint and plotted as a function of time. If a deviation of ± 4 horizontal encoders is registered an alarm is sent with the current value.

The front panel: The main tab of the program consists of a histogram (Figure 3.19). The reference points have a distance of approximately 3000 horizontal encoder values. To make the comparison easier an offset was added to each reference point so that the distance between each one with the next is equal to 40 units. The histogram can be set to three modes: All the data, Only tracking data and non tracking data. The next tab includes the reference positions stored in the files for every check point as a function of time for all three modes (Figure 3.20). The tab information and communication contains all the information needed about the data taking (Figure 3.21). In this tab there are indicators about the base path of the Encoder files directory, the number of files read, the last modified file and the time and file name of the last input in the software. In addition, the user can use the knob controller to set the sampling time, the time that the program checks if the current file was modified.

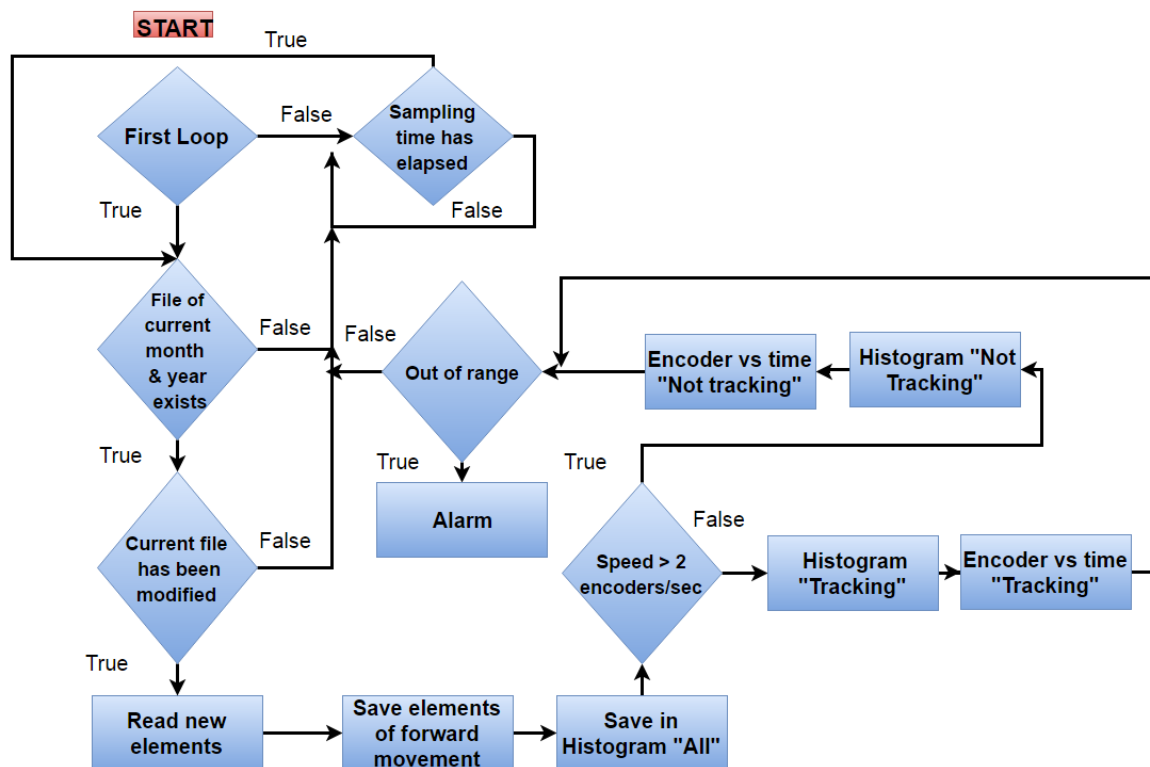


FIGURE 3.18: The flow diagram of the horizontal motor check program

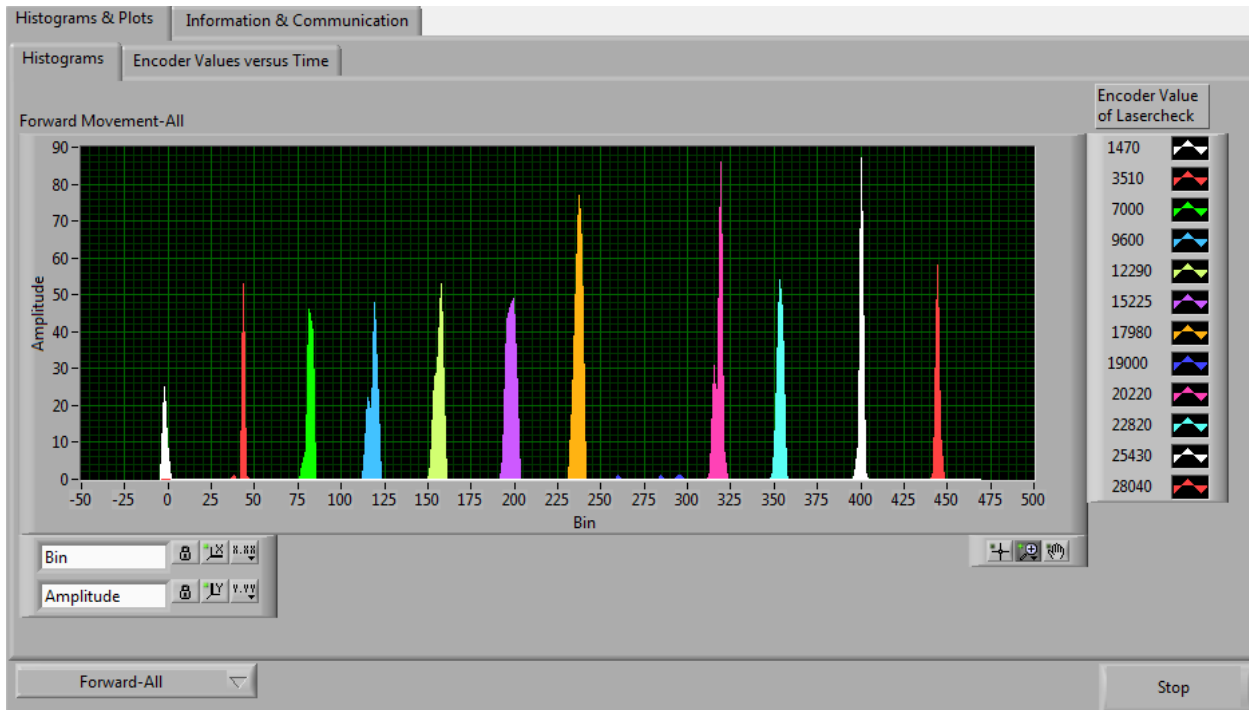


FIGURE 3.19: The main tab of the program

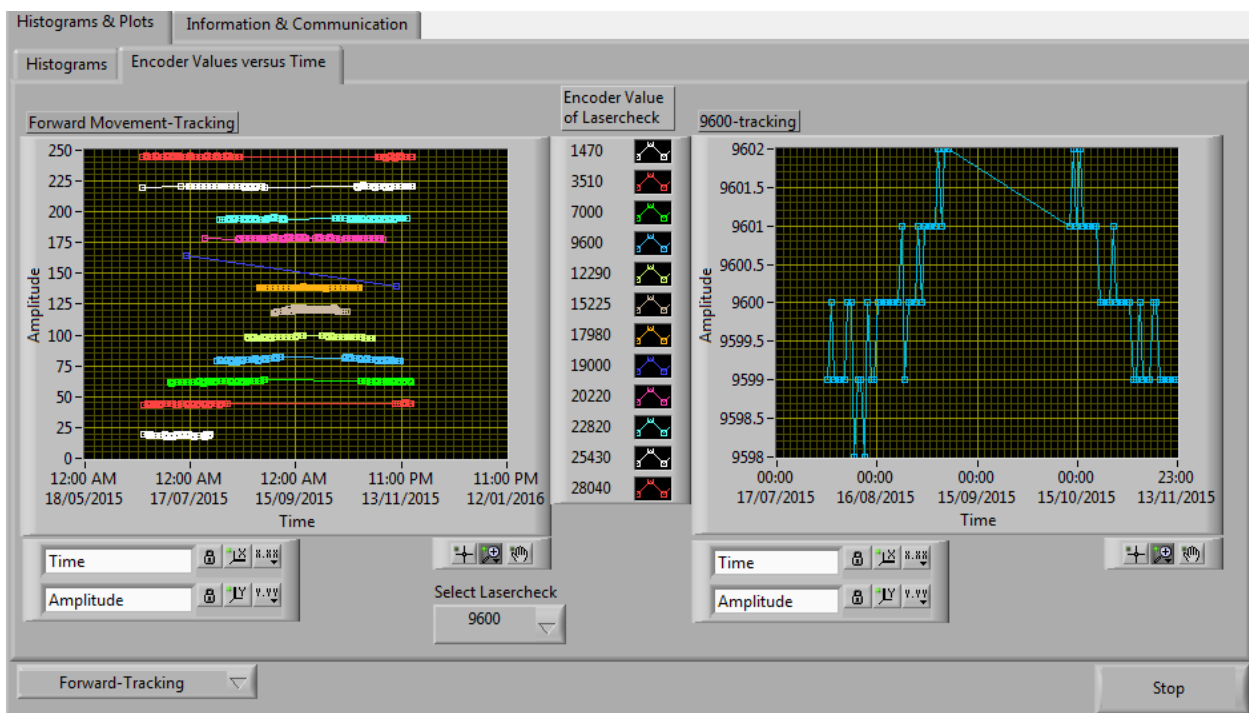


FIGURE 3.20: The encoder reference positions as a function of time for every checkpoint and for every mode

3.3.3 Analysis of data

The reference positions acquired in 2015 are plotted in the histograms of figures 3.22 and 3.23 for tracking and non-tracking motion respectively. The frequency of the movement is

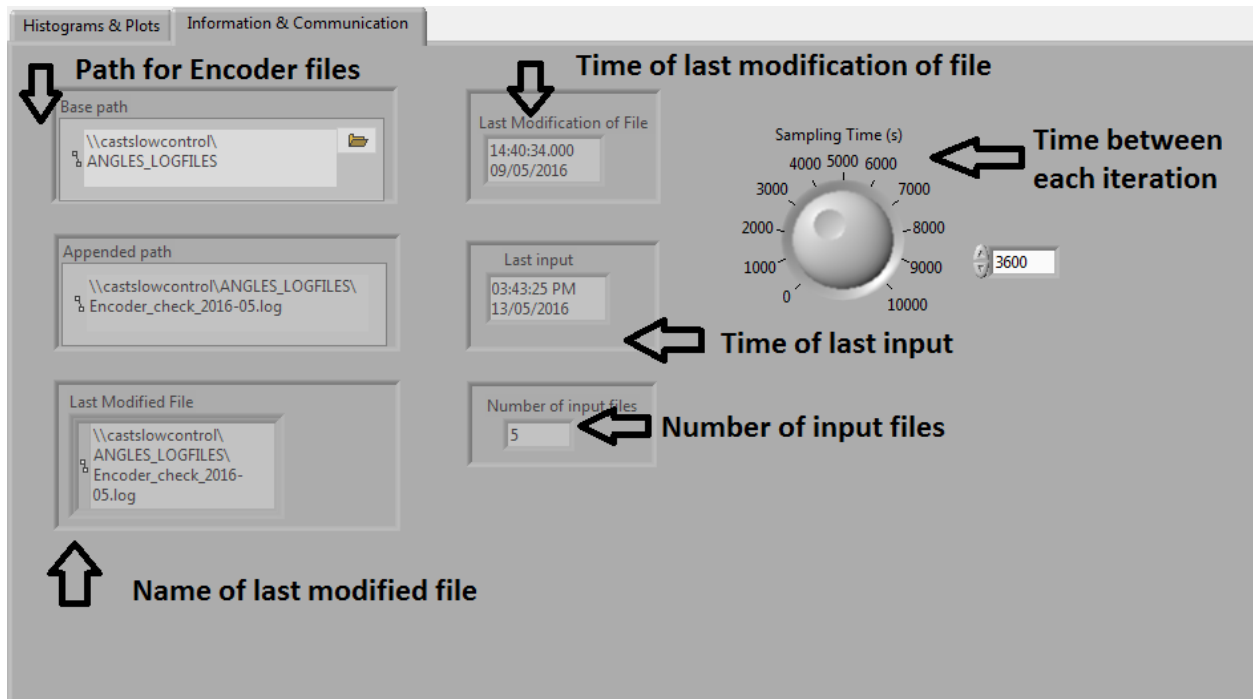


FIGURE 3.21: The tab Information & Communication of the software

correlated with the spread of the gaussian, which represents the range of values obtained for each reference point. From figure 3.24 it is clear that the standard deviation is shifted to greater values for frequencies higher than 40 Hz. Lower frequency leads to a more narrow spread of values and consequently to more accurate measurements. As a result, the mean value of each reference point is also affected by the movement of the magnet. As can be seen in figure 3.25 in most cases when the magnet is moving with a frequency lower than 40 Hz the mean value has a higher value than the one calculated with the non-tracking data. This leads to the necessity of separating the data according to the frequency during the online monitoring.

For the comparison of the data of 2014 and 2015, the mean values of each reference point were subtracted. For all the data included, no deviation higher than 1.9167 encoder units was observed (Figure 3.26), equivalent to 0.9583 mm in 10 m (Figure 3.27). For the movement of the magnet with a frequency lower than 40 Hz the maximum difference observed is equal to 0.9872 encoder units or 0.4939 mm in 10 m.

From the offline analysis of the data of 2014 and 2015 no noticeable deviations are observed. The results of 2014 are reproduced in 2015 with a maximum mean difference of less than 0.1 mm, which is an acceptable limit for the accuracy needed during the data taking.

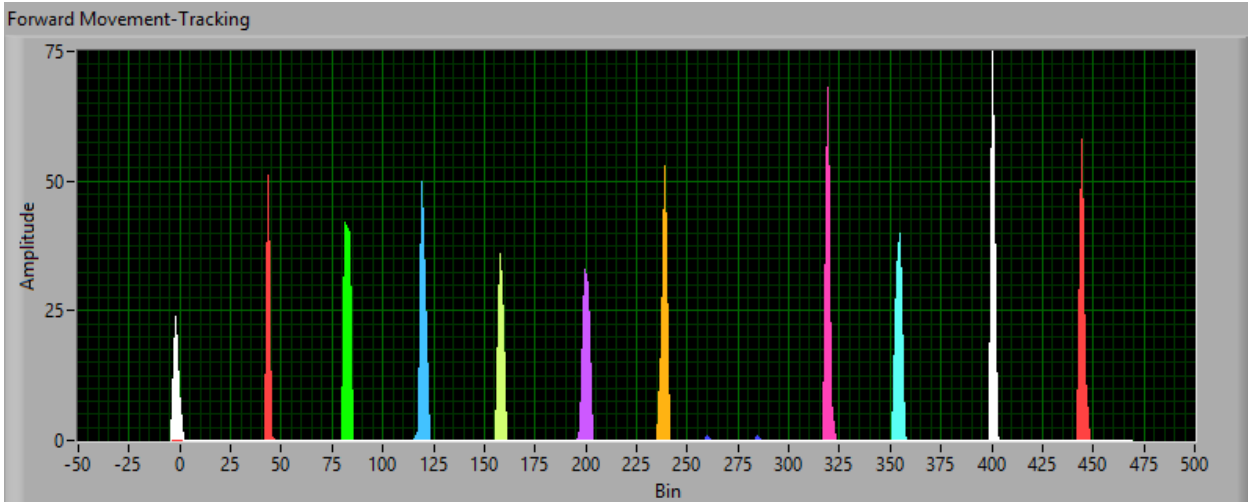


FIGURE 3.22: The histogram of the 2015 tracking data

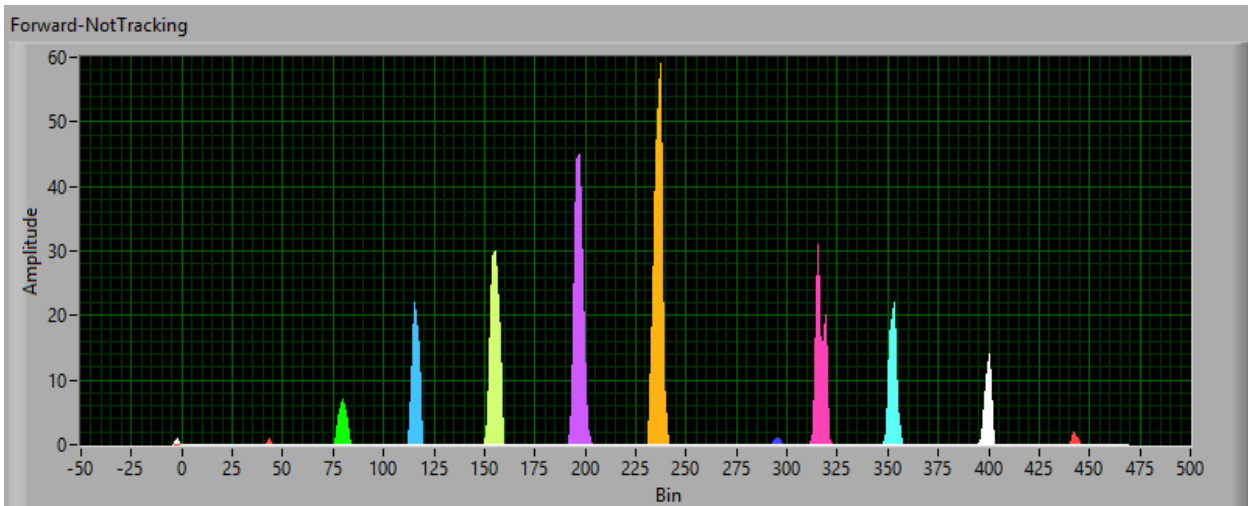


FIGURE 3.23: The histogram of the 2015 non-tracking data

3.4 Magnet Movement control system

3.4.1 Hardware

The range of movement of the CAST magnet is from 46° to 133° horizontally and -8° to $+8^\circ$ vertically. The MFB side is supported upon a rotary pivot while the MRB side is mounted on a four-wheel trolley which moves on rails. Two three-phase induction motors control the vertical and the horizontal movement. The movement of the vertical motor is connected with two jacks that rotate around two lifting screws. If the movement is forward the polar angle increases while if it is reversed the polar angle of the position of the magnet decreases. The horizontal motor controls the horizontal motion by driving a wheel. Forward horizontal movement leads to clockwise motion of the magnet and higher azimuth angle and vice versa for the reverse movement. Two pairs of master-slave motor encoder systems monitor the horizontal and vertical motion and the values of the digital panel displays are transmitted to the tracking software. One vertical encoder unit corresponds to $40\mu m/10m$ and one horizontal encoder unit to $0.5mm/10m$.

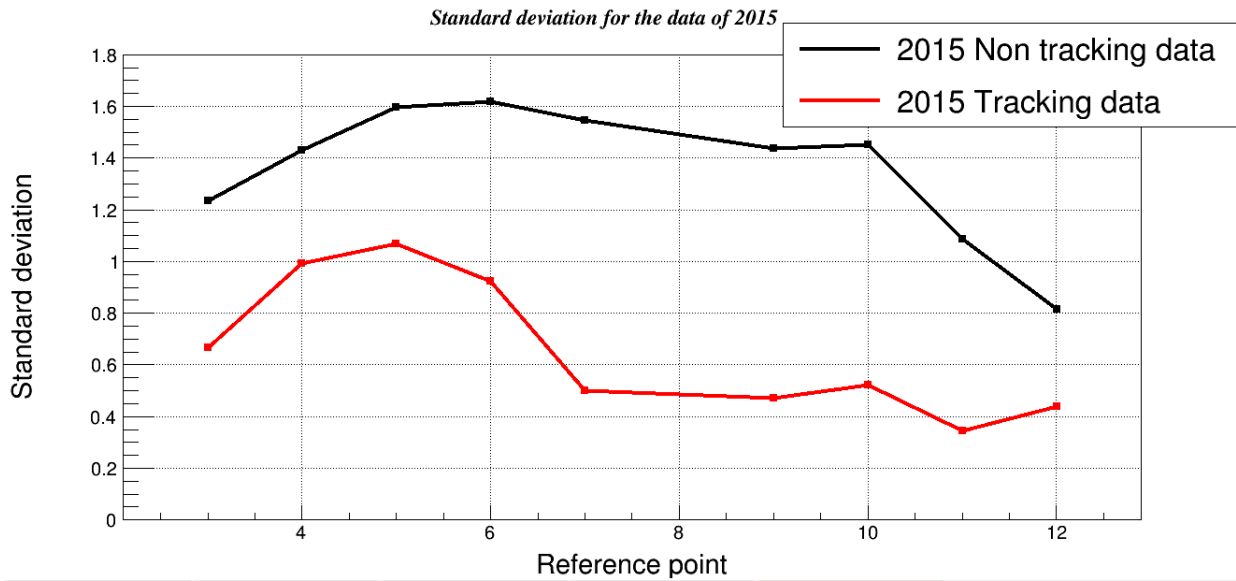


FIGURE 3.24: The standard deviation of the gaussian of each reference point for tracking and non tracking data of 2015

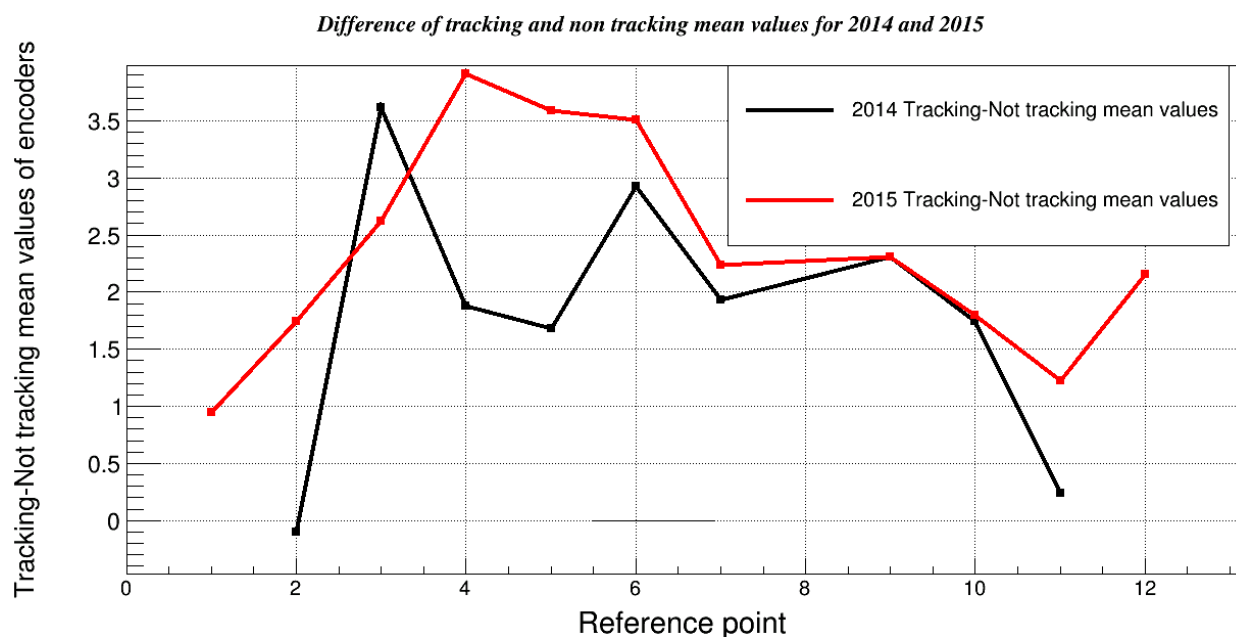


FIGURE 3.25: The difference of the tracking and not tracking data for 2014 (black) and 2015 (red)

The frequency of the vertical motors can vary from 0 to 70 Hz while for the horizontal motor the range is 0 to 150 Hz. For a varying frequency output of the motors two frequency rectifiers-inverters are required. The rectifiers-inverters convert the ac power at one frequency to dc power and then the dc power to an ac power at a different frequency. The ones used in the CAST experiment can be seen in figure 3.28.

The flow diagram of the voltage through the system is shown in figure 3.29. The operating mode selected is the V/F meaning that the ratio of the voltage in the stator with the frequency is constant for values lower than the field weakening area. For an induction motor

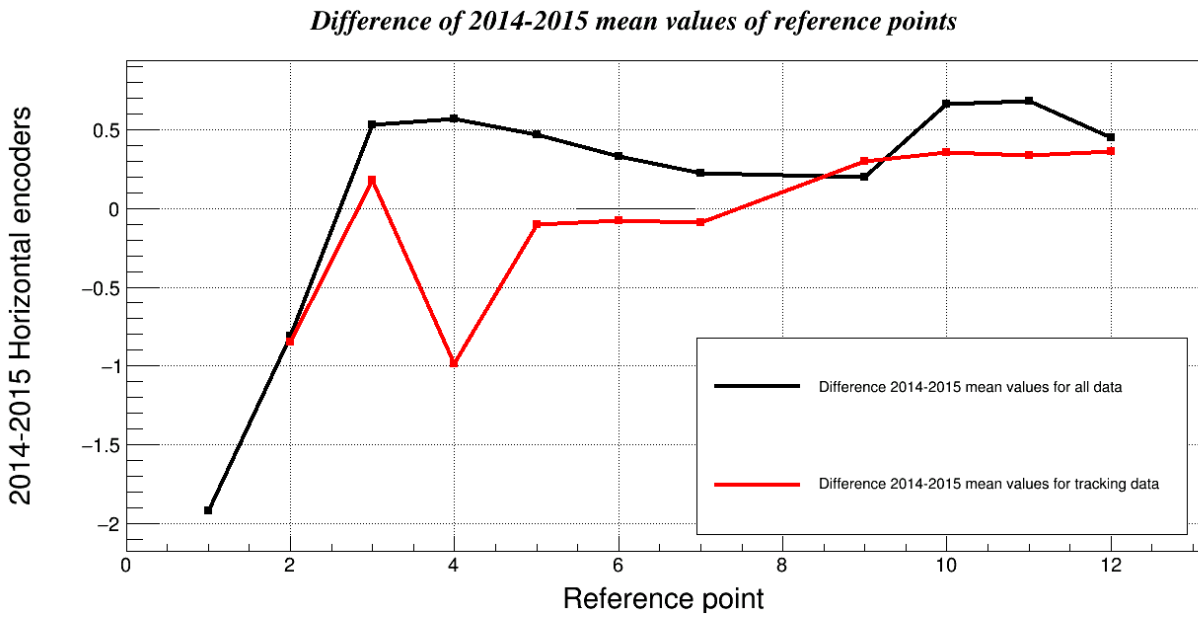


FIGURE 3.26: The 2014-2015 difference of mean values of each reference point for all the data (black) and for the tracking data (red)

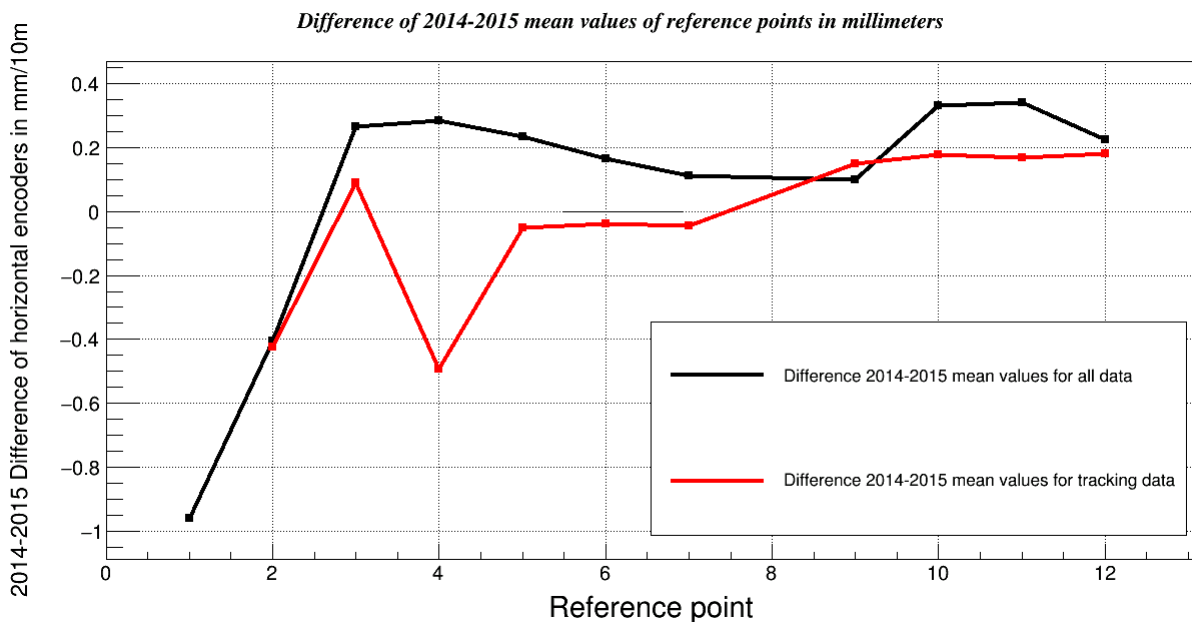


FIGURE 3.27: The 2014-2015 difference of mean values of each reference point for all the data (black) and for the tracking data (red)

the asynchronous speed can be calculated as follows:

$$n = \frac{120f(1-s)}{P} \quad (3.8)$$

where:

f is the frequency of the input voltage

n is the mechanical speed in rounds per minute



FIGURE 3.28: The frequency converter used in the CAST area.

P is the number of poles

s is the slip

The torque on the shaft is equal to:

$$T = k_1 \phi_m I_2 \quad (3.9)$$

where:

k_1 is a constant that depends on the material

ϕ_m is the magnetizing flux in Wb

I_2 is the current in the rotor which depends on the load

For the magnetizing flux:

$$\phi_m = k_2 \frac{V_1}{f} \quad (3.10)$$

where:

V_1 is the voltage of the stator

k_2 is material dependent constant

f is the frequency

From equation 3.9 the current in the rotor is constant as it depends only on the load. Assuming that the torque is also constant:

$$I_2 = \frac{T}{k_1 \phi_m} \Rightarrow \phi_m = ct \Rightarrow \frac{V_1}{f} = ct \quad (3.11)$$

However, when the frequency increased beyond a base value the magnetic flux starts decreasing. In this field weakening area the ratio voltage-frequency and the torque start decreasing.

The simplified electronic circuit of the frequency converters can be divided into two part:

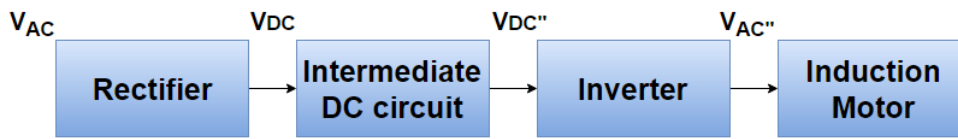


FIGURE 3.29: The flow diagram of the system rectifiers-inverters and motors.

1. **The rectifier circuit** is a three-phase full wave rectifier for converting ac power to dc power composed by three wire thyristors which are shown in figure 3.30. For positive values of v_a the first thyristor in the left corner of the circuit is switched on and the same time the negative value of v_B switches on the thyristor in the lower part of the B-wire. These two voltages are summed in the output. The output of the circuit can be seen in figure 3.31 and it is an approximation of a DC voltage. The capacitor and the inductor of figure 3.30 are added to the output of the rectifier circuit to cut out harmonics and smooth the dc output [35].

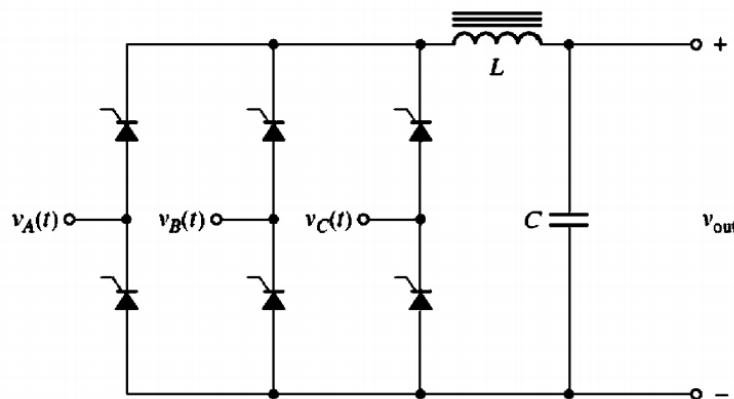


FIGURE 3.30: The rectifier circuit of the frequency converter [35].

2. **The inverter circuit:** In this phase the DC voltage is inverted to AC with the pulse width modulation technique (PWM). Three switches R, S, T are controlled as appropriate to produce a 3-phase voltage on the poles of the motor whose magnitude and frequency can be controlled (Figure 3.32). The states of the switches are on at the first half of each cycle and then off. The frequency and the voltage can be controlled by using more voltage pulses per half-cycle in the main voltage. Figure 3.33 shows the waveform for five pulses per half cycle. By modulating the on and off times of the power switches both output frequency and output voltage can be controlled so that the ratio V/f is constant (Figure 3.34).

3.4.2 The Solar tracking program

The Solar tracking program is the LabView software that controls the movement of the magnet for the tracking of the sun. The position of the sun is calculated using NOVAS software. Every one minute the program calculates the position of the sun and controls the

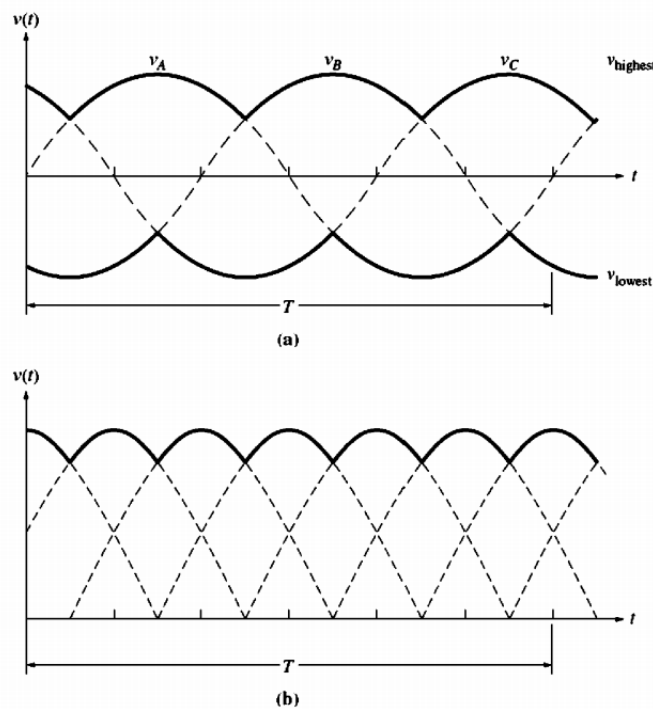


FIGURE 3.31: a) The highest and lowest voltages in the three-phase full-wave rectifier with diodes and b) the output voltage [35]. The highest of the three phase voltages is connected to the load at any given instant while the lowest is connected to the other end of the load.

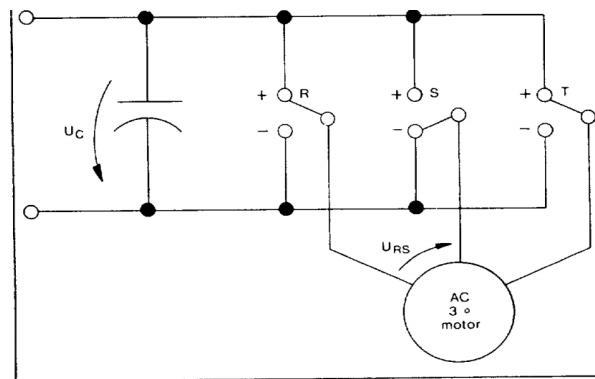


FIGURE 3.32: A simplified scheme of the inverter circuit [36].

speed of the vertical and horizontal movement so that the sun will be reached and followed. The software properly modifies the speed during each loop and it compares the expected and the reached position to calculate the accuracy of the tracking. The block diagram is composed of a stacked sequence with 18 frames which can be described as follows:

- A new file is created for each day or if it is the first iteration of the program. The name of the file has a format "year-month-day-hour-minutes-seconds" which are acquired from the system. If it is the first iteration or if the day has changed and a new file was created a header is added to the file.
- The position of the sun is evaluated. The kernel.exe is executed with the time after

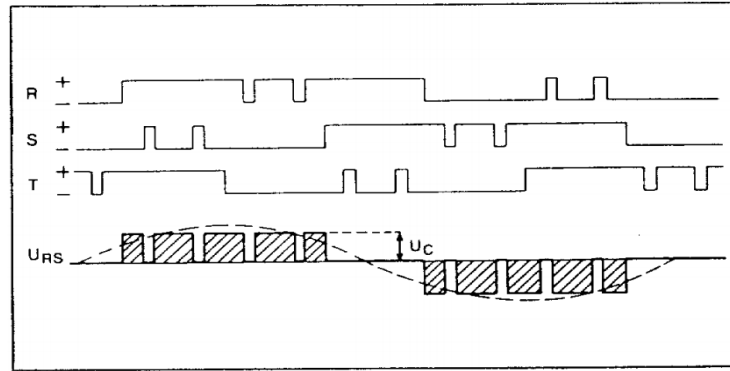


FIGURE 3.33: Switch positions and Voltage $U + RS$ for a pulse number equal to five [36].

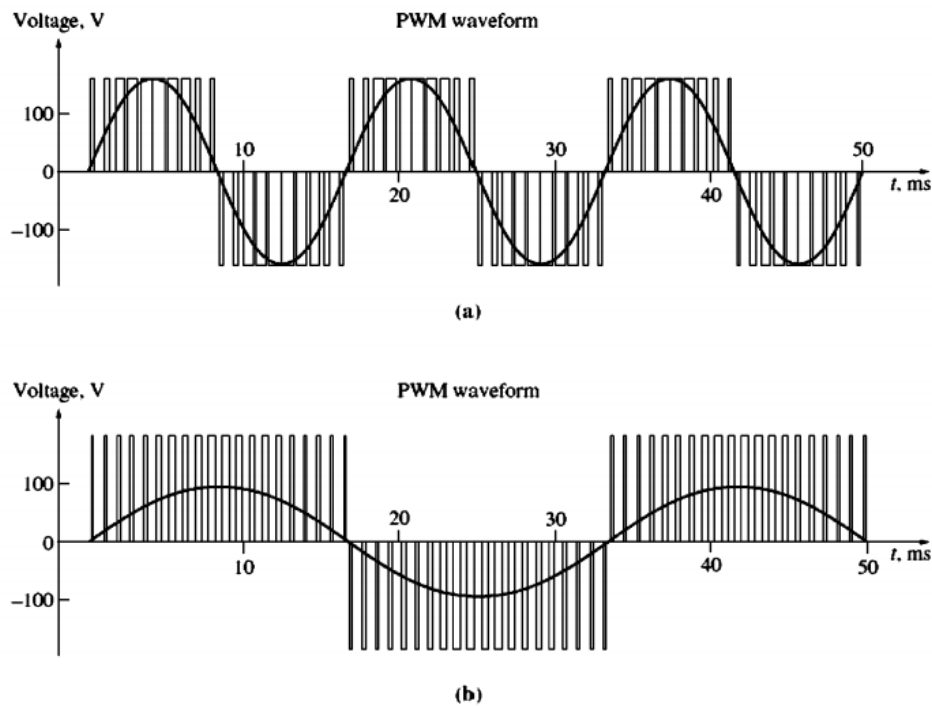


FIGURE 3.34: The PWM output of the inverter. The frequency and the voltage are simultaneously controlled so that the ratio V/f is constant [35].

one minute as an input. The outputs of the executable are the azimuthal, the zenith and the galactic coordinates of the sun in the next minute.

- The program determines if the sun is rising or not, if it is in the safe band of the magnet's movement and if the sun is reachable. If this is the case it sends a command to the inverters with the appropriate position and frequency of movement. At the same time the program checks if the sunfilming boolean button is pressed. If it is true then a correction to the altitude is added so that the magnet can follow the visible sun.
- The Hardy.exe executable is used to transform the goal position in encoder units and it checks that the goal encoder units are in range.

- The program establishes communication with the horizontal inverter by sending a command and reading the response of the device with the horizontal encoder.
- If the horizontal encoder is out of range the general failure boolean button is switched on.
- It calculates the frequency needed to reach the horizontal goal encoder from the current horizontal encoder position. If the frequency required has a higher value than the maximum allowed it will use the maximum frequency and if it is lower than 0.1 Hz the frequency will be set to zero. The instantaneous precision of tracking is calculated and the values of the voltage and current of the motors are sent to the program.
- The time when the horizontal encoder was sent to the program is stored. It will be compared with the time that the vertical encoder was acquired as they are sent to the program with a difference of a few seconds.
- The same procedure is repeated for the Vertical encoder.
- The horizontal and the vertical position are plotted.
- From the measured encoder values the galactic and topocentric coordinates are calculated with Hardy.exe and stored in the logfiles. The time used is the average between the time that the horizontal encoder was read and the time that the vertical encoder was read because time delays are added due to the communication with the inverters.
- All the data are stored in the logfiles.
- Every time that the hour changes and if the software is not in solar tracking mode the program plays a wave file.
- A delay is added so that the loop of one minute is completed. If the sunfilming boolean button is on the user has to enter a value of the pressure and temperature that will be added to the correction of the altitude during sunfilming.
- If the general failure boolean button is on or if the user has pressed the stop button the vertical and horizontal motor movement are stopped, the data are saved in AFS. If there was a failure an alarm is sent.

3.4.3 Upgrade of the communication system

Serial interface is used for the communication between devices over longer distances compared to the parallel. In serial communication protocols each byte of information is sent and received one bit at a time. RS 232 is the most common serial interface and allows for one transmitter and one receiver on the same line. The RS485 standard has multi-drop capabilities allowing up to 32 devices to communicate via the same line. The differential form of the signals over two lines allows lower rates of noise and with the combination of lower logic voltage levels transmission over greater distances is achieved with higher speed. Ethernet on the other hand supports higher bit rates and a longer distance transmission.

A new parallel communication system between the inverters and the new Tracking computer has been installed. So far, the communication between the inverters and the computer was done via a MOXA RS485-RS232 converter. In order to create a parallel system, a female

and a male 9 pin D-SUB connectors were added to the system as shown in figure 3.35. By plugging in the two connectors the old system is used. The new system consists of a MOXA RS485 to Ethernet converter which is connected to the new Female D-SUB connector and a 12 meter Ethernet cable is used for the transmission of the signal to the computer (Figure 3.36). The connections of both systems can be seen in figure 3.37 and figure 3.38 respectively.

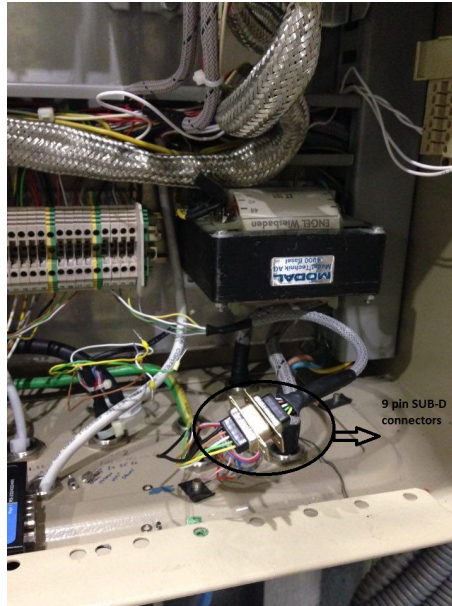


FIGURE 3.35: The new 9 pin SUB-D connectors that allow the transition from the old to the new system.

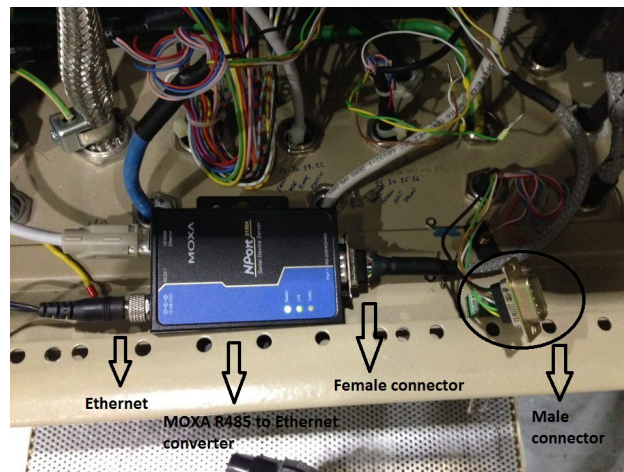


FIGURE 3.36: The connection of the new system with the RS485 to Ethernet converter.

After installing the new converter, a series of tests had to be done to reassure that the device is properly working. For this reason a simulation of a 2014 solar tracking was done and the results were compared in order to detect possible deviations between the previous and the current communication system. From figures 3.39 and 3.40 both systems lead to similar results for horizontal and vertical movement respectively. For a more precise comparison, the fitting of each data set is calculated and then subtracted from the data. In figure 3.41

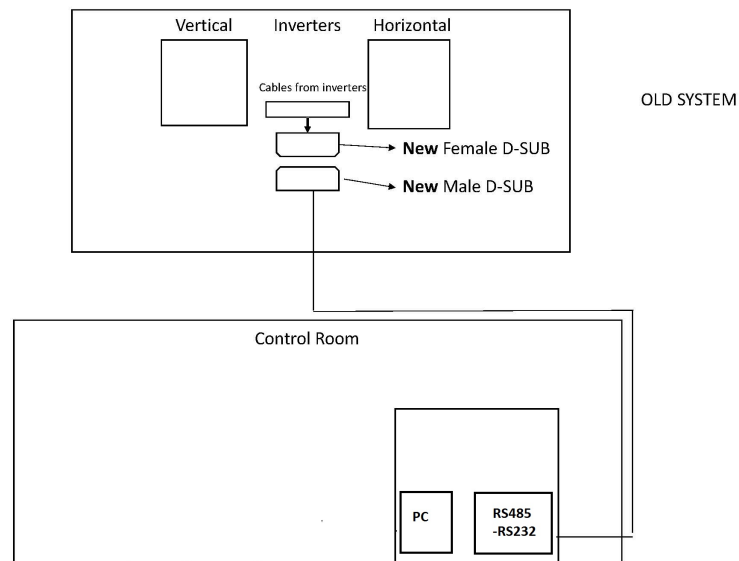


FIGURE 3.37: Previous communication system consisting of an RS485 to RS 232 converter

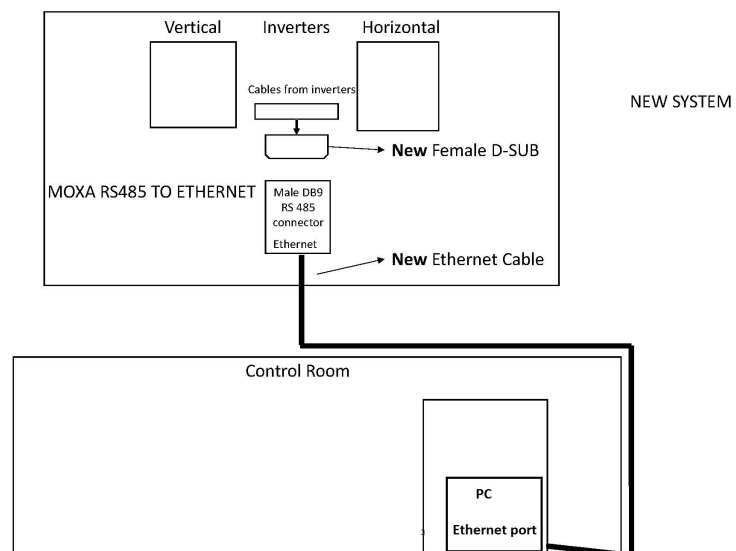


FIGURE 3.38: New communication system consisting of a RS 485 to Ethernet converter.

and 3.42 it can be seen that both systems follow the same trend compared to their fitting for horizontal and vertical movement without noticeable differences.

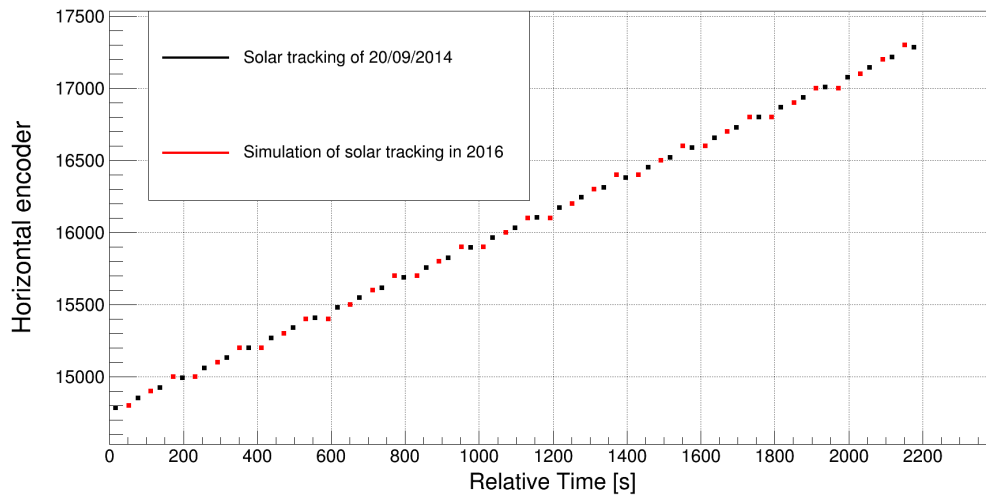


FIGURE 3.39: The Horizontal movement of the magnet as a function of time for the actual solar tracking of 2014 (blue) and for the fake tracking of 2016 with the new communication system (red)

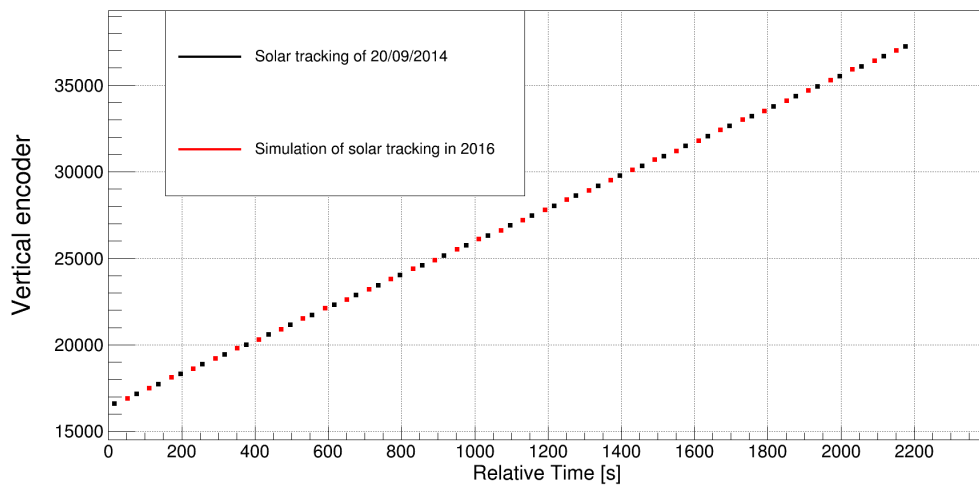


FIGURE 3.40: The Vertical movement of the magnet as a function of time for the actual solar tracking of 2014 (blue) and for the fake tracking of 2016 with the new communication system (red)

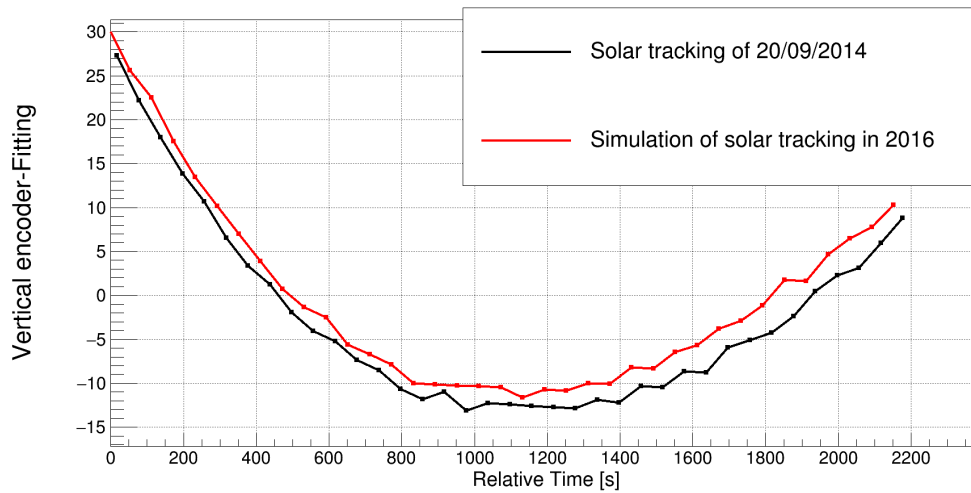


FIGURE 3.41: The Vertical encoders subtracted by the fitting as a function of time for the actual solar tracking of 2014 (blue) and for the fake tracking of 2016 with the new communication system (red)

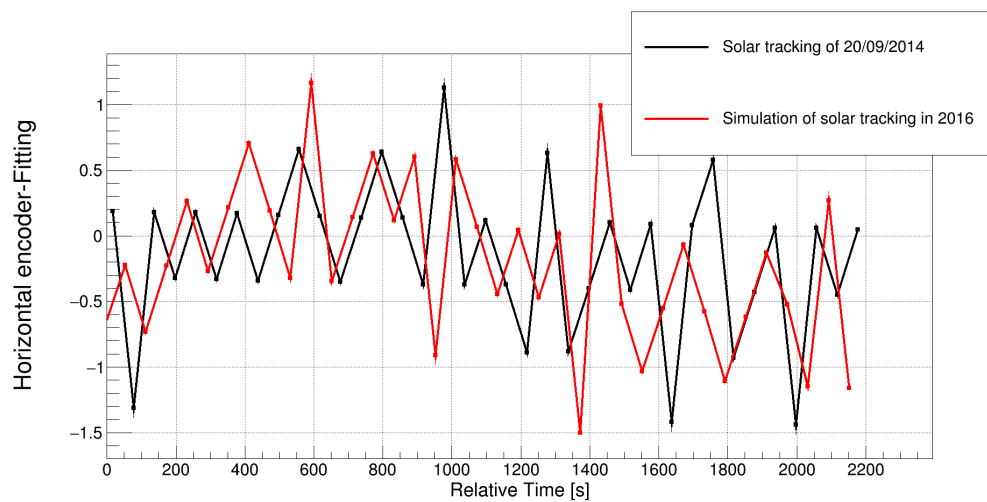


FIGURE 3.42: The Horizontal encoders subtracted by the fitting as a function of time for the actual solar tracking of 2014 (blue) and for the fake tracking of 2016 with the new communication system (red)

Chapter 4

Silicon Drift Detector System

4.1 Introduction

4.2 X-ray spectroscopy

4.2.1 Introduction

Radioactive sources are an essential tool for testing and calibrating detectors. Radiation refers to both electromagnetic emissions such as X-rays and γ -rays and corpuscular which include α -particles, Auger electrons, neutrons, protons among others as shown in figure 4.1. There are two categories of radiation. The first category, non ionizing radiation, has a wavelength of 10nm or longer and it includes radiowaves, microwaves, visible light and ultraviolet light. The rest of the electromagnetic spectrum, the ionizing radiation, includes X-rays, γ -rays with a shorter wavelength than that of X-rays and atomic and subatomic particles like electrons, positrons, protons, alphas, neutrons, heavy ions and mesons. Ionizing radiation causes ionization of an atom or a molecule of the medium it traverses. In the next section the X-ray production mechanism will be discussed.

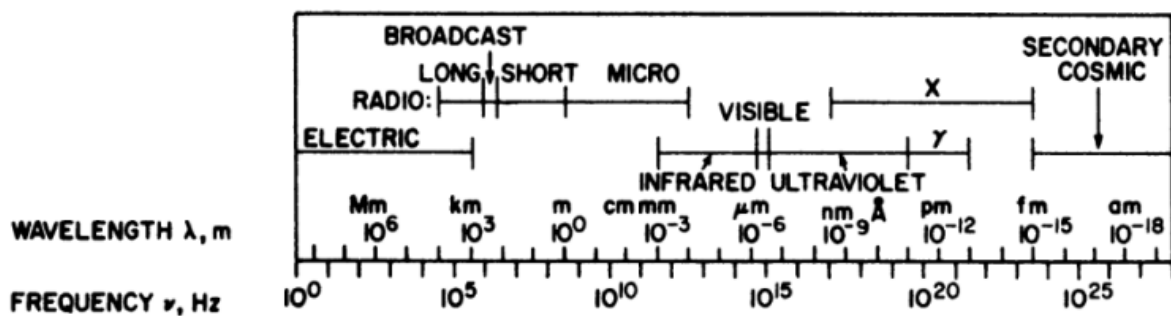


FIGURE 4.1: The electromagnetic spectrum.

4.2.2 X-ray fluorescence

Due to the photoelectric effect, when energetic particles with sufficient energy strike a target material, electrons are ejected from the inner shells of the atom, creating vacancies. The atom returns to a stable condition through the transition of electrons from outer to inner shells accompanied by an emission of X-rays with energies equal to the difference between the two binding energies of the corresponding shells. The characteristic X-rays are named according to the shell of their origin and according to the transition from higher shells as can

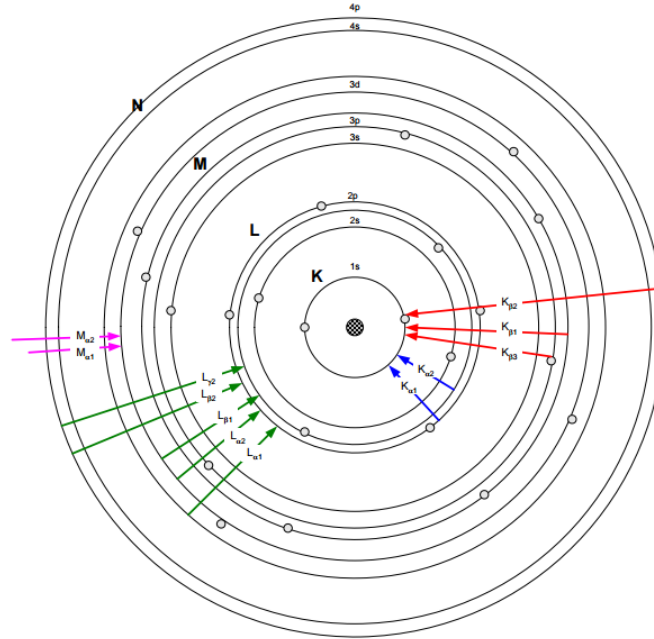


FIGURE 4.2: The X-ray fluorescence process. An electron from a specific shell is ejected from the atom and a vacancy is created. This vacancy is filled by an electron of an outer shell and through this process a characteristic X-ray is emitted [37].

be seen in figure 4.2. The label $K\alpha$ denotes an X-ray produced from an L to K shell transition, $K\beta$ from an M to K shell transition. Instead of the emission of a characteristic X-ray, the energy can be transferred to one of the outer shell electrons and cause its ejection from the atom (Auger electron). The energy levels are different for each element and therefore the X-rays emitted are characteristic.

Apart from the characteristic peaks, the X-ray spectrum consists of a continuous spectrum. The energetic electrons that hit the target decelerate and they lose part of their kinetic energy by emitting electromagnetic radiation. Therefore, this continuous band is due to bremsstrahlung, which means braking radiation. By conservation of energy, the maximum value that this spectrum can reach is equal to the acceleration voltage, when the electron loses all of its energy in one interaction. The X-ray spectrum of Copper is shown in figure 4.3.

4.2.3 Interaction of photons with matter

The most important mechanisms that take place when X-rays hit matter are the photoelectric effect, the Compton scattering and the production of pairs.

In the photoelectric effect, a photon interacts with the atom resulting the ejection of an electron from one of its bound shells with energy:

$$E = hv - E' \quad (4.1)$$

where:

h is the Planck constant

ν is the frequency of the photon

E' is the binding energy of the electron

The vacancy in the inner shell is filled by a free electron of the absorbed medium or by an electron from an outer shell, generating X-ray photons or Auger electrons.

During the Compton scattering the beam of photons partially transfers energy in the electrons of the material and are deflected from their initial course. The scattered radiation wavelength, the Compton shift wavelength, can be calculated as:

$$\Delta\lambda = \lambda_e(1 - \cos\theta) \quad (4.2)$$

where:

λ_e is the Compton wavelength of the electron

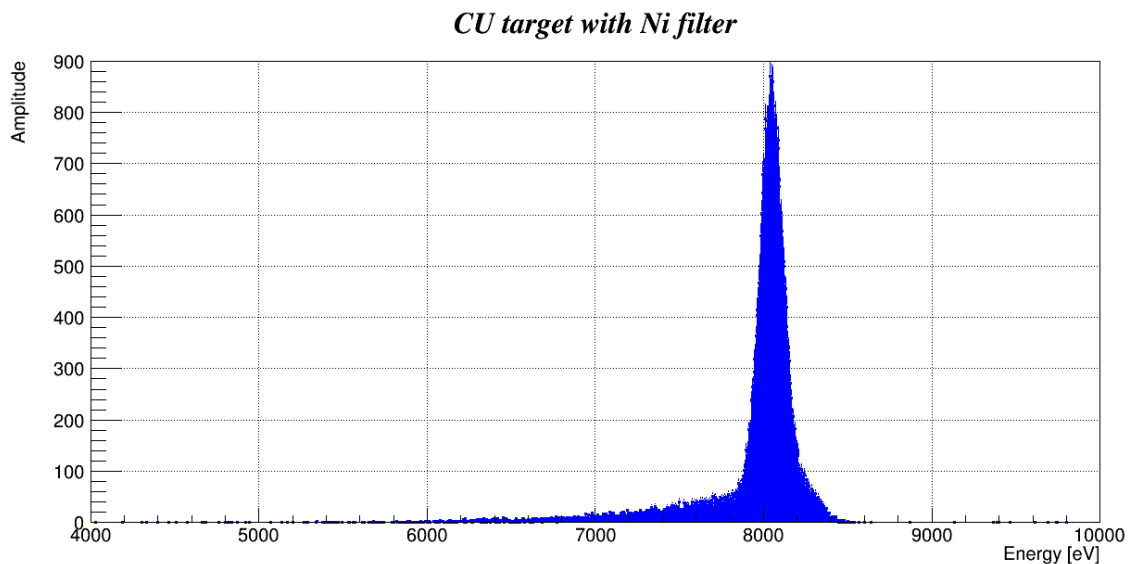


FIGURE 4.3: The X-ray spectrum of Copper with a Nickel filter. The bremsstrahlung and the superimposed X-ray peaks K_{a1} and K_{a2} at 8.0478 keV with relative intensity 100 and 8.0278 keV with relative intensity 51 respectively can be seen.

Electron-Positron pair production is possible when the γ -ray energy exceeds twice the electron rest mass energy. At high Z , pair production is the dominant process of photon interaction as can be seen in figure 4.4.

The probability of occurrence of these interactions per unit path length is the attenuation coefficient, it depends on the photon energy and on the material and it is expressed as follows:

$$\mu = \tau + \sigma + \kappa \quad (4.3)$$

where:

τ, σ, κ are the probability of photoelectric, Compton and pair production interactions respectively.

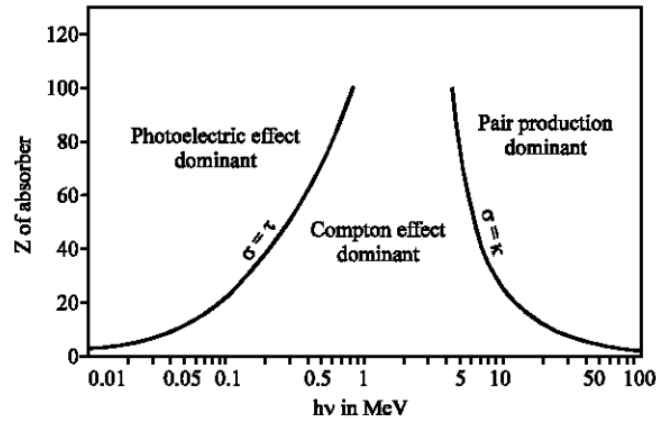


FIGURE 4.4: Interaction mechanisms of photons with matter according to the energy of the incident beam and the Z of the material [38].

The inverse quantity of the attenuation coefficient expresses the average distance that the ray will travel inside the absorber unaffected. The attenuation of the beam is due to the reduction of the number of photons from the beam and it is exponential respectively to the thickness. Therefore, the intensity of an X-ray beam traversing a material with thickness x can be calculated:

$$I(x) = I_0 \exp(-\mu x) \quad (4.4)$$

where:

I_0 is the incident beam intensity

μ is the absorption coefficient

x is the thickness of the absorber

4.2.4 X-ray beam line

The laboratory 162/S-065 at CERN is a detector testing facility with a variable target X-ray generator. The X-ray beam line, built at the Max-Planck-Institut für extraterrestrische Physik/Garching (MPE), is used for the calibration of the detectors used in the CAST experiment. The working principle of the X-ray generation is based on the use of the X-ray tube with electrons as the energetic particles.

By applying voltage to a vacuum cathode filament in vacuum, electrons are emitted and they are then accelerated by an intense electric field. The accelerated electrons hit the target and X-rays are produced, along with heat. The system of the variable targets includes 18 slots and all the available targets are summarized in table 4.1. The power supply of the anode can reach a maximum value of 35 kV, however for safety reasons it does not operate higher than 15 kV and the Wehnelt power supply provides focusing of the beam but it is not usually used (Figure 4.5). In order to turn on the power supplies a safety key must be used.

The X-ray generator must operate under vacuum. Gate Valve V2 separates the line into two sides, the generator and the detector side. If any modification has to be done in the detector side valve V2 must be closed so that the generator side is still under vacuum. The generator is pumped by a turbo molecular pump and a sputter ion pump. The detector

Position	Target	Peaks [keV]
1	Ti	4.51
2	Ag	3
3	Mn	5.9
4	C	0.28
5	Bn	0.18
6	Au	2.12
7-11	Al	1.49
12-18	Cu	8.05

TABLE 4.1: The available targets in the X-ray generator and the values of their characteristic peaks in the spectrum



FIGURE 4.5: The power supplies of the X-ray beam line.

side is pumped by two turbo molecular pumps, one of which has a needle valve for slow pumping. Gate Valve V1 is used to separate the generator side from the turbo pumps and to assure that this side is under static vacuum even when the pumping system is no operating

(Figure 4.6).

The pressure gauges are used to monitor the pressures in the system and their values are being displayed in a Maxigauge and a Dual Gauge. These values are associated with an interlock system which sends a signal if one of them exceeds a maximum value to open or close one of the valves or switch off the power supply of the anode. All the pressures are also monitored by a LabView Slow Control system [30].

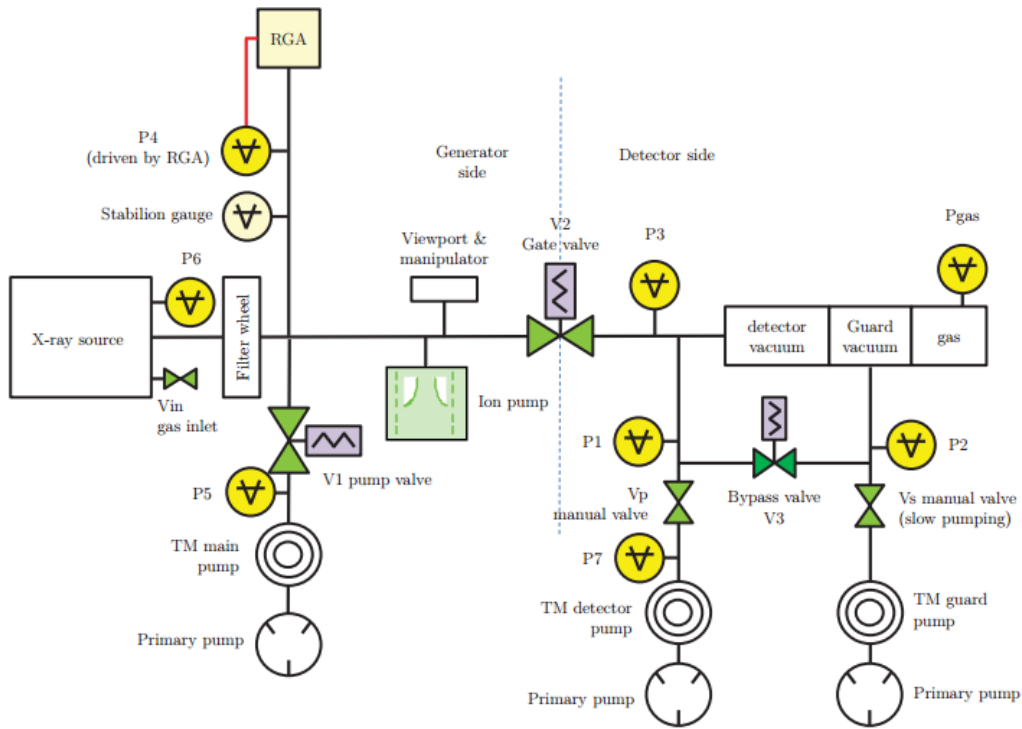


FIGURE 4.6: The vacuum system of the X-ray beam line [30].

4.3 Silicon Drift Detector

4.3.1 Properties of semiconductor materials

From Fermi statistics, the energy distribution of electronic states in solids can be described by the expression [39]:

$$N(E)dE = P(E)[S(E)dE] \quad (4.5)$$

where:

$N(E)dE$ is the number of electrons per unit volume with energy between E and $E+dE$

$S(E)dE$ is the number of electronic states per unit volume with energy between E and $E+dE$

$P(E)$ is the Fermi distribution function which describes the probability that a state of energy E is occupied and can be calculated as:

$$P(E) = \frac{1}{1 + e^{\frac{E-E_f}{kT}}} \quad (4.6)$$

where:

E_f is the Fermi energy

k is the Boltzmann constant

T is the temperature in Kelvin

For temperatures close to zero, the valence gap of semiconductors is fully occupied while the conduction band is empty. As temperature increases the tail in the Fermi distribution of figure 4.7 allows electrons to enter to the conduction band. This process can take place through absorption of radiation when electrons, after interacting with photons, acquire enough energy to cross over the bandgap which, for semiconductors, has a small value. The holes which are left in the valence interact with the electrons of the conduction band and during the deexcitation process more electrons and holes are produced, leading to higher necessary average energy for electron-hole production than the energy gap. Both parameters are a function of temperature as can be seen in figure 4.8.

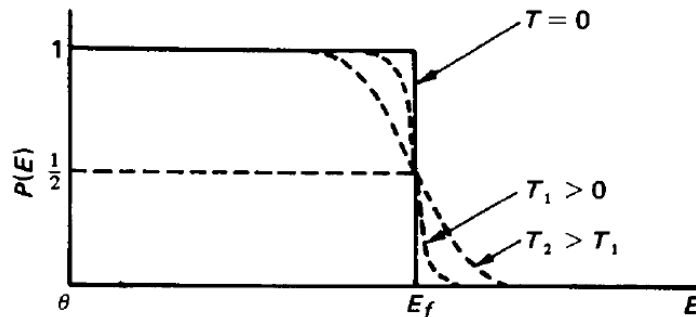


FIGURE 4.7: The Fermi distribution function. [39].

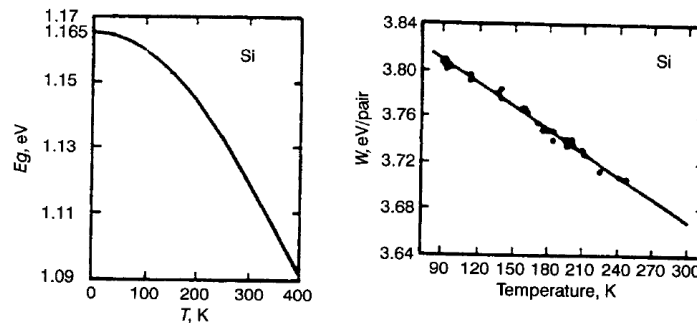


FIGURE 4.8: The variation of a) the energy gap on the left and b) of the average energy for electron-hole pair production on the right as a function of temperature of silicon. [39].

For semiconductor materials, the average energy for the creation of an electron-hole pair is one order of magnitude smaller than the one needed for ionization of gases as shown in figure 4.9. As a result, measurement of lower energies and much higher precision can be achieved. The high density of the material (2.33 g/cm^3) causes large energy losses and a short absorption length. Therefore, strong signals can be produced even with thin detectors. The delta-electrons have a very small range and do not escape a significant distance away from the primary radiation beam. Thus a great precision in the measurement of the start of the track can be achieved. However, the mobility of the carriers is not influenced by the high density and due to their high mobility they can be rapidly collected even in the case of high-rate events. Another unique characteristic of semiconductor detectors, is the possibility of doping the crystal used and creating sophisticated field configurations without affecting the mobility of the carriers. Both the material of the electronics and of the detector are manufactured by silicon and can be integrated into a single device [40].

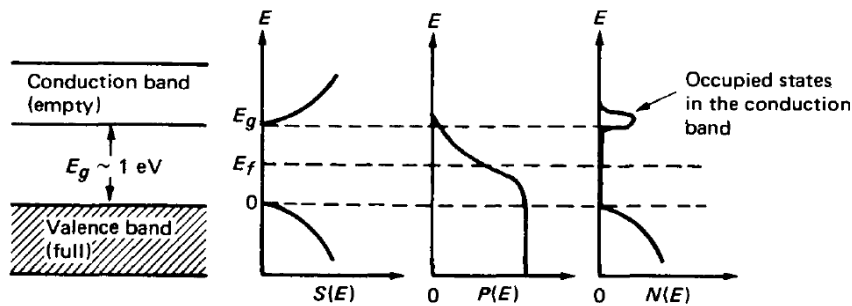


FIGURE 4.9: The energy gap of semiconductors. The average energy necessary for the creation of an electron-hole pair is equal to 3.66 eV. For most gases the average energy required for electron-ion pair production is equal to 30 eV. As temperature increases electrons are able to move to the conduction band. [39].

4.3.2 Characteristics of semiconductor detectors

Semiconductor detectors are solid-state devices that operate by measuring the electron-hole pair production from incident radiation in the material of the detector. Silicon (Si) and Germanium (Ge), the most widely used materials for that type of detectors, provide several characteristic properties that are not available with other detector types. The most important advantages of the semiconductor detectors are their improved energy resolution, the fast pulse risetime and the linear response.

When radiation interacts with semiconductor material electron-hole pairs are created with part of the energy absorbed, while the rest of the energy is converted into lattice vibrations called phonons. The number of pairs created can be calculated as follows:

$$N = \frac{E}{w} \quad (4.7)$$

where:

E is the energy absorbed

w is the mean energy for electron-hole pair production and it is equal to 3.65 eV for silicon

The variance of N is equal to:

$$\Delta N^2 = FN \quad (4.8)$$

where:

F is the Fano factor and it is equal to 0.115 for silicon

The Fano factor is added because the ionization events are not independent and the Poisson statistics cannot be applied. It is a function of all the energy transfer processes that can take place and it is characteristic of the medium. The Fano factor is usually $F < 1$ and for $F = 1$ the variance is the same as the Poisson distribution variance. The resolution of the detector, its ability to distinguish two close lying energies, is proportional to the full width at half maximum (FWHM):

$$\begin{aligned} \text{Resolution} &= \frac{\Delta E}{E} \\ &= 2.35 \sqrt{\frac{Fw}{E}} = 2.35 \sqrt{\frac{F}{N}} \end{aligned} \quad (4.9)$$

where:

ΔE is the full width at half maximum

With a sensitive region of a few millimeters and in combination with the speed of electrons being two to three times higher than that of the holes, the charge can be collected in the order of 10^{-7} s in semiconductor detectors.

4.3.3 Silicon Drift Detector (SDD)

The Silicon Drift Detector was first proposed by Gatti and Rehak in 1983 [41]. The operating principle is based on sideward depletion (Figure 4.10). In a large area of semiconductor wafer composed by high-resistivity n-type silicon, p^+ junctions cover both surfaces. By applying reverse bias with respect to a small ohmic n^+ contact the depletion layers expand to the wafer with the square root of the applied voltage until they are combined. As a result, the entire device is depleted at a voltage four times lower than that needed for the depletion of a $p^+ nn^+$ diode. The energy potential minimum is in the n^+ anode, as can be seen by figure 4.11, where the electrons must be drifted. This is achieved by adding arrays of p^+ electrodes in both sides of the wafer which provide a parallel to the surface electric field. Once ionizing radiation has lead to the production of an electron-hole pair, electrons are drifted to the anode while holes are collected by the p^+ electrodes. Through this mechanism, the interaction position can be determined from the drift time of the electrons and the energy of the incident ionizing radiation can be measured by the amount of collected charge in the anode.

In order to achieve low noise rates, the capacitance of the collecting node of the signal has to be minimized. Therefore, the collection area has to be decoupled from the readout node. In the silicon drift detector an applied electric field causes the transport of the signal to a low capacitance output node, which is independent of the size of the sensitive area of the detector. The electric field forces the electrons to the n^+ readout anode which collects

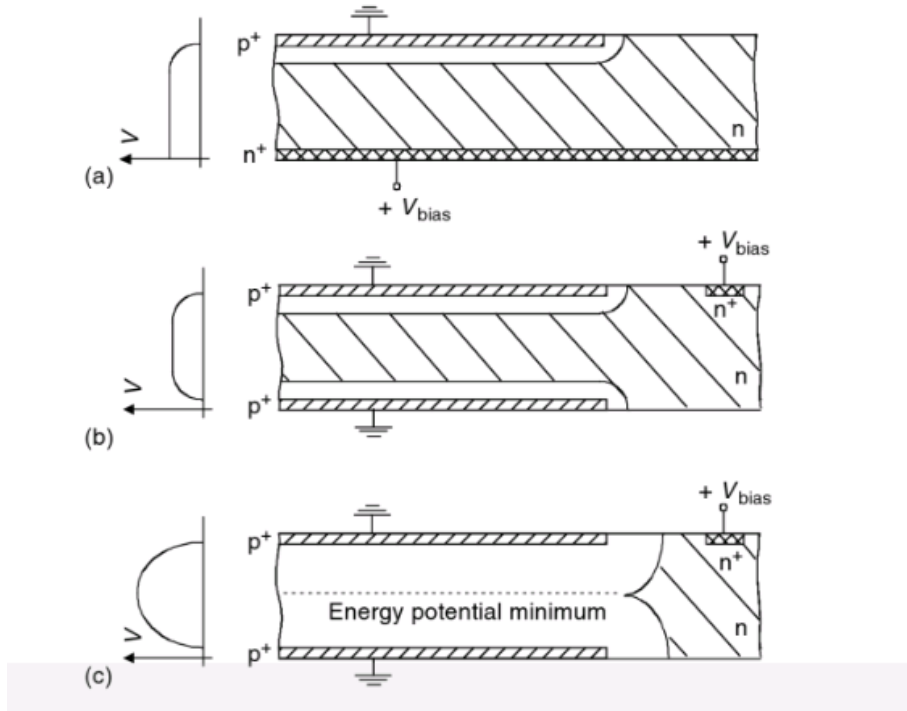


FIGURE 4.10: Sideward depletion [42].

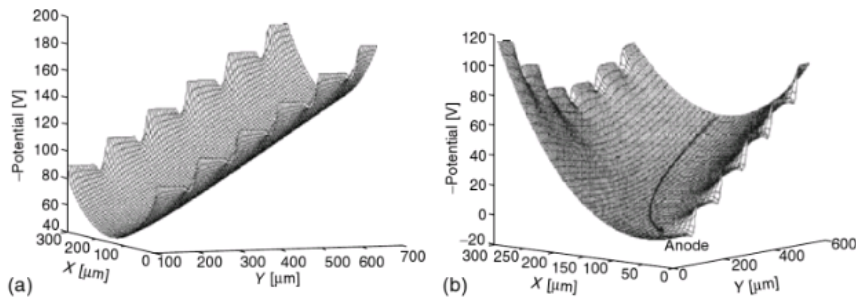


FIGURE 4.11: The potential in a) the drift region and b) in the region close to the anode where the electrons are directed towards the surface [42].

all accumulated electrons. The holes from the ionization disappear in the p^+ strips. The drift field E_d is applied between the out p^+ drift structures and the inner p^+ drift rings. The drift field can be calculated as follows:

$$E_D = \frac{\Phi_{out} - \Phi_{in}}{x_{out} - x_{in}}$$

The anode is connected to a single sided n-channel amplifying junction field effect transistor (JFET) integrated directly on the detector chip to avoid an increase of capacitance and electrical pickup that would be provoked by bond wires between the detector and the amplifier (figure 4.12). When an electron, generated by ionizing radiation, drift towards the anode, a voltage change is coupled to the p_+ gate of the n-channel transistor. As a result, the gate is reverse biased and thus depleting into the transistor channel, resulting in a current drop through the transistor, which can be measured. When the reverse bias of the

gate reaches a certain potential difference relative to the transistor channel it discharges by impact ionization in the transistor channel close to the junction of the gate and the drain at the end of the channel. However, the gate adjusts its potential so that all signal electrons and leakage current by the breakdown mechanism are compensated.

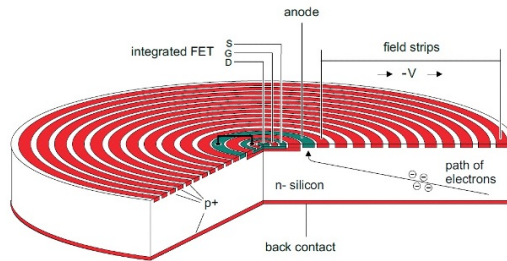


FIGURE 4.12: Operating principle of Silicon Drift Detector [43].

The total noise of the system is equal to sum of white serial noise, which is due to thermal fluctuations, the low frequency noise, because of the trapping of charge carriers and parallel noise due to the detector and the gate leakage current. The equivalent noise charge ENC can be calculated as:

$$\begin{aligned} ENC^2 &= \text{white series noise} + \text{low frequency noise} + \text{parallel noise} \\ &= (4kT \frac{2}{3g_m} C_{tot}^2) A_1 \frac{1}{\tau} + (2\pi a_f C_{tot}^2) A_2 + (qI_1 + \frac{2kT}{R_f}) A_3 \tau \end{aligned} \quad (4.10)$$

where:

g_m is the transconductance of the FET

A_1, A_2, A_3 are constants depending on shaper's filter function

a_f is a constant related to the low frequency noise

I_1 is the leakage current

R_f is the equivalent resistor feedback

The energy resolution of the detector can be expressed as:

$$\Delta E_{FWHM} = 2.355 \sqrt{ENC^2 + \frac{FE}{w}} \quad (4.11)$$

where:

F is the Fano factor and it is equal to 0.115 for silicon

E is the total X-ray energy

w is the pair creation energy

ENC is the rms fluctuation of the readout noise

The detector that was used in the CAST experiment was a commercial SDD-100-130pnW-OM-ic from PNdetector, Munich without a vacuum window and with a large surface of 89 mm^2 , covering 6.13% of a total diameter of 43 mm of the magnet cold bore [44]. The device was fabricated by $450 \text{ }\mu\text{m}$ thick polysilicon and a quantum efficiency of more than 80% for energies above 400eV as can be seen in figure 4.13. A copper heat exchanger block was used to remove the 1.1 W from the preamplifier and the 1.0W from the detector. The detector was put inside a vacuum vessel iso-K DN 100 mode from stainless steel and directly connected to the vacuum bore from the one side and to a OFE copper flange in the other side. Inside the vacuum vessel shielding was provided by a copper OFE inner cylinder and on the outside by lead plates and rings as can be seen in figure 4.14

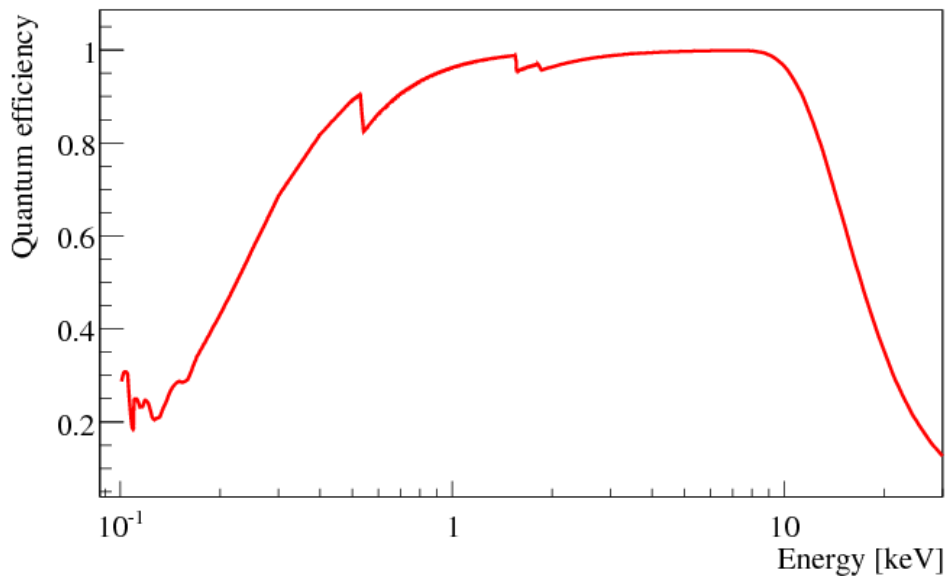


FIGURE 4.13: Quantum efficiency of Silicon Drift Detector [44].

4.3.4 Nuclear Instrumentation

The readout system of the Silicon Drift Detector consists of a preamplifier, a shaping amplifier and a Multichannel Analyzer as seen in figure 4.15. The current pulse from the detector enters the preamplifier and it takes the form of a voltage step. The output of the preamplifier is shaped, stored and then displayed. In the current section the electronic components of the readout system of the Silicon Drift Detector are presented.

Preamplifier

A preamplifier is required for silicon detectors. The output signal of the detector is a low-amplitude, short-duration current pulse. The preamplifier acts as a coupler between the signal from the detector and the rest of the counting system. The output signal of the detector must be amplified before being transmitted through a cable to the amplifier, otherwise due to the attenuation it will not be discriminated from the noise. The preamplifier must be placed as close to the detector as possible and it provides a first slight amplification. Its main purpose however is to provide electronic matching between the detector and the amplifier.

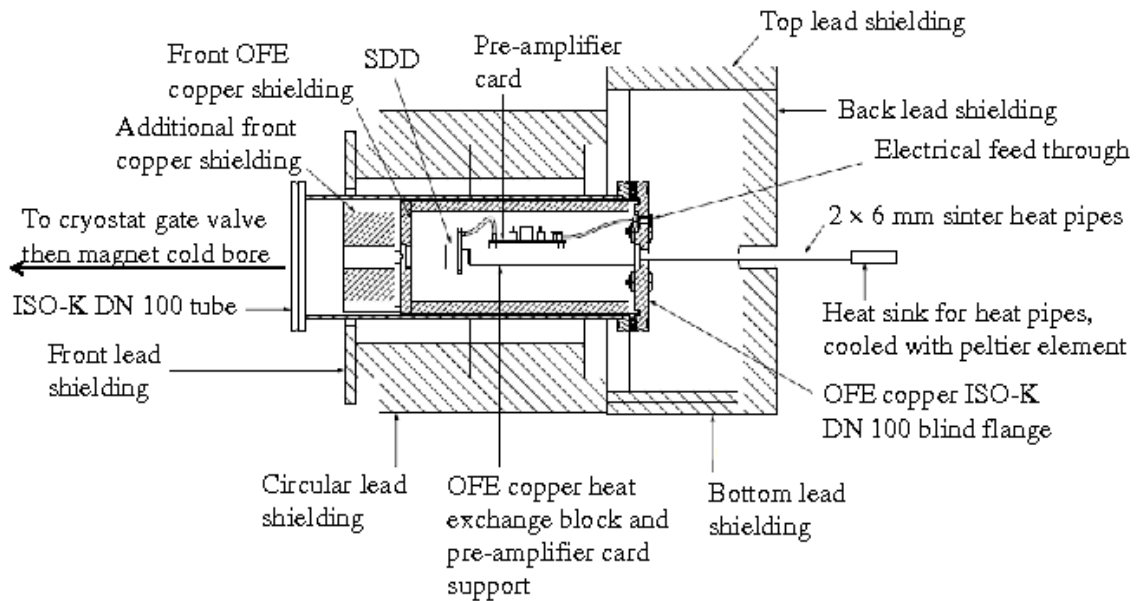


FIGURE 4.14: Vacuum and shielding system of Silicon Drift Detector [44].

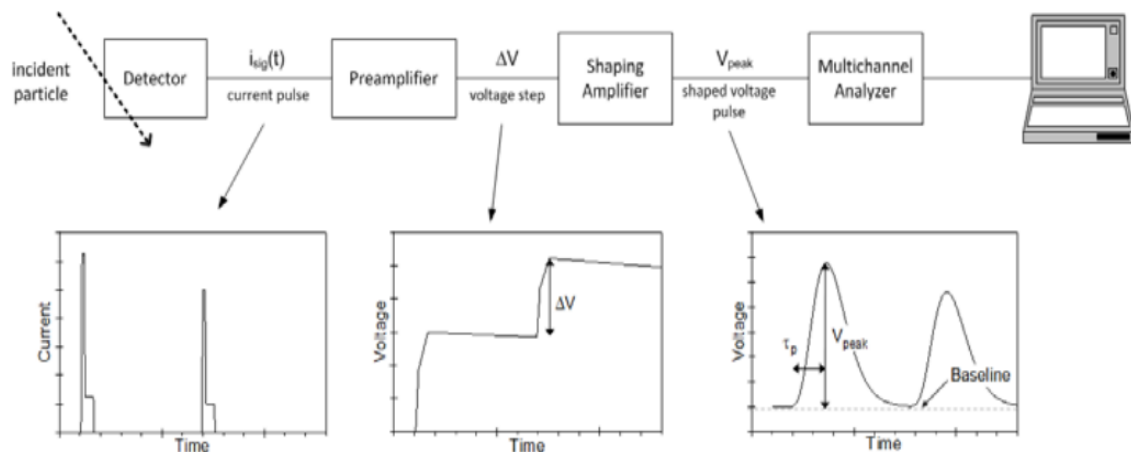


FIGURE 4.15: The Pulse Height analysis system [37].

With each event there is a step increase of the preamplifier output to a higher dc voltage. When the staircase of pulses approaches the power supply voltage, the voltage is reset to its initial value. The amplitude of the step is proportional to the energy deposited in the detector.

For the Silicon Drift Detector of the laboratory, a PNDetector preamplifier electronic board from Munich is used. The board provides the voltage supply for the detector and the

reset pulse. In a typical connection scheme, the board consists of a detector connector, one signal and one gate output and a supply voltage connector. For the operation of the SDD connector, a low voltage power supply +12V -24V, a high voltage power supply 170 V and a Peltier cooling 3V must be connected to the supply-voltage connector. In addition, a voltage meter is used for the display of the temperature of the detector.

Spectroscopy Amplifier

The low-voltage pulse from the preamplifier enters the preamplifier where it is amplified and shaped. All input pulses are linearly amplified over a range of 0 to 10 V as indicated by the coarse and fine gain controls. For the pulse shaping a combination of electronic differentiation, integration and filtering is required. The differentiating circuit consists of a capacitor and a resistor (figure 4.16) and acts as a high pass filter. If $q(t)$ is the charge of the capacitor at time t then the total voltage is equal to:

$$\begin{aligned} V_i(t) &= V_R(t) + V_C(t) \\ &= \frac{q(t)}{C} + R \frac{dq(t)}{dt} \end{aligned} \quad (4.12)$$

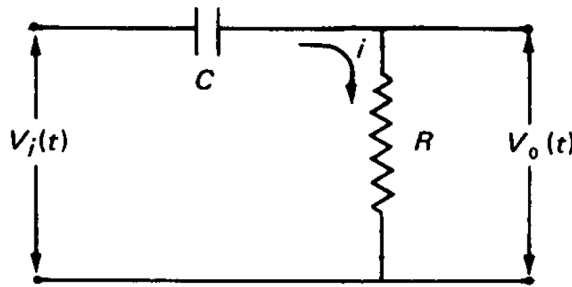


FIGURE 4.16: The electronic circuit of a differentiator [39].

The rising edge of the preamplifier passes and the voltage decays exponentially back to baseline. The output voltage can be calculated as:

$$\begin{aligned} V_o(t) &= R \frac{dq}{dt} \\ &= V_m e^{-\frac{t}{RC}} \end{aligned} \quad (4.13)$$

The integrating circuit consists as well of a capacitor and a resistor however the output signal is derived through the capacitor. The integrator as a low pass filter, improving the signal to noise ratio. For a step function as a input:

$$\begin{aligned} V_o(t) &= \frac{q(t)}{C} \\ &= V_m (1 - e^{-\frac{t}{RC}}) \end{aligned} \quad (4.14)$$

The total output of a CR-RC circuit is shown in figure 4.17. By adding another RC integrating circuit a Gaussian shaping is achieved.

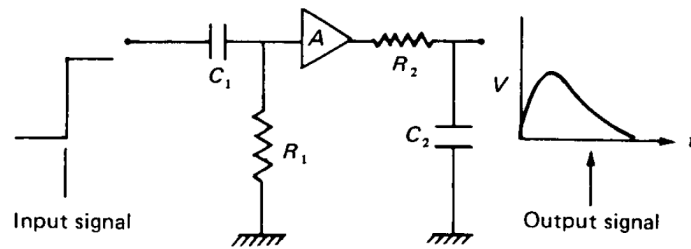


FIGURE 4.17: The electronic circuit of CR-RC shaping [39].

As a spectroscopy amplifier, the Canberra Model 2026 was used, power supplied by a NIM rack. Two types of pulse shaping methods were used in the measurements, Gaussian and Triangular and six shaping time constants for each pulse shaping method. In order to obtain an appropriate position of the peaks of interest in the spectrum, a coarse gain of 50 was selected. The reset pulse of the preamplifier produces a large signal to the amplifier. Therefore, the inhibit input of the amplifier was directly connected to the output of the gate of the preamplifier to avoid overloading condition and spectral distortion. The output of the amplifier is a positive shaped pulse with an amplitude linear to +10V and with a maximum value of 12V.

Multichannel Analyzer (MCA)

The multichannel analyzer stores every pulse in an appropriate channel according to its amplitude. The output of the amplifier is digitized through an ADC and a digital signal proportional to the amplitude of the input pulse is generated. The height of the pulse is proportional to the energy of the particle that hits the detector and every time that a pulse is stored in a specific channel the counter of that channel increases. Therefore, the spectrum that is recorded is a histogram of channels which correspond to a histogram of energies.

The readout system that includes a spectroscopy amplifier and a multichannel analyzer can be seen in figure 4.18

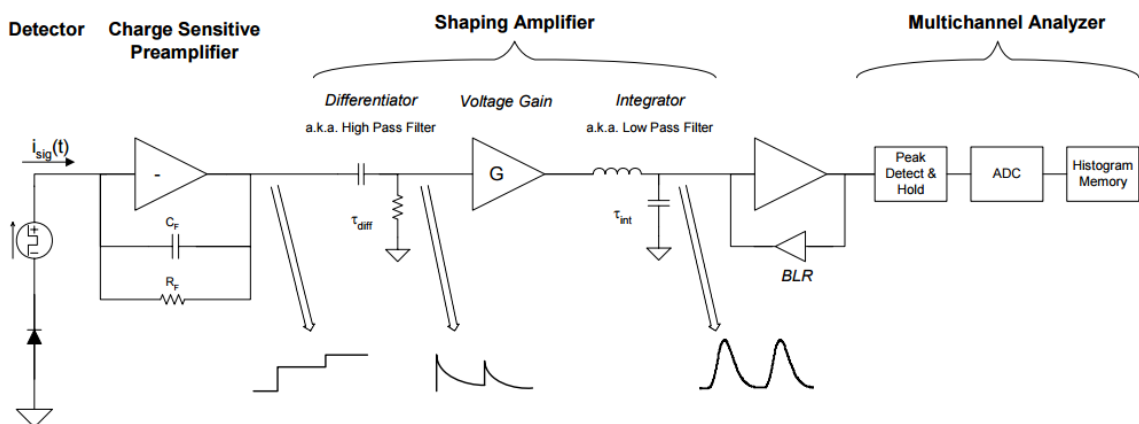


FIGURE 4.18: A schematic of an analog pulse processor consisting of a CR-RC-RC electronic circuit [45].

Digital Pulse Processor

A Digital Pulse Processor performs the same function as the system of a shaping amplifier and a Multichannel Analyzer, as described in the previous section, with multiple performance advantages. The output signal of the preamplifier, the millivolts-height step, passes through an ADC and it is directly digitized. Then it is differentiated, integrated and the digitized output pulse is stored in a histogram memory according to its amplitude (Figure 4.19). It must be noted that in DPP the pulse is shaped in triangular and trapezoidal shapes.

Multiple advantages are associated with the use of a Digital Pulse Processor:

- As seen in figure 4.20, the output of the differentiator is not an exponential function and therefore it has a finite impulse response, meaning that any input has a zero effect after a finite amount of time. As a result, a reduction of pile-up events is observed leading to an improved performance.
- In the Digital pulse Processor reduced ballistic deficit is observed. In the analog shaper if the rising edge is slow the exponential decay of the output pulse starts before the pulse has reached full amplitude, resulting in the loss of pulse height and worst resolution. When the signal passes through a digital differentiator, the actual maximum value of the pulse is acquired and therefore the rising edge of the output of the differentiator has the same shape as the preamplifier pulse (Figure 4.21).
- In the spectroscopy amplifier system, the signal reaches the Multichannel Analyzer and it is then digitized through an ADC, which adds dead time to the system. In a digital pulse processor the signal is directly digitized at a fast rate and not dead time is associated with the system.

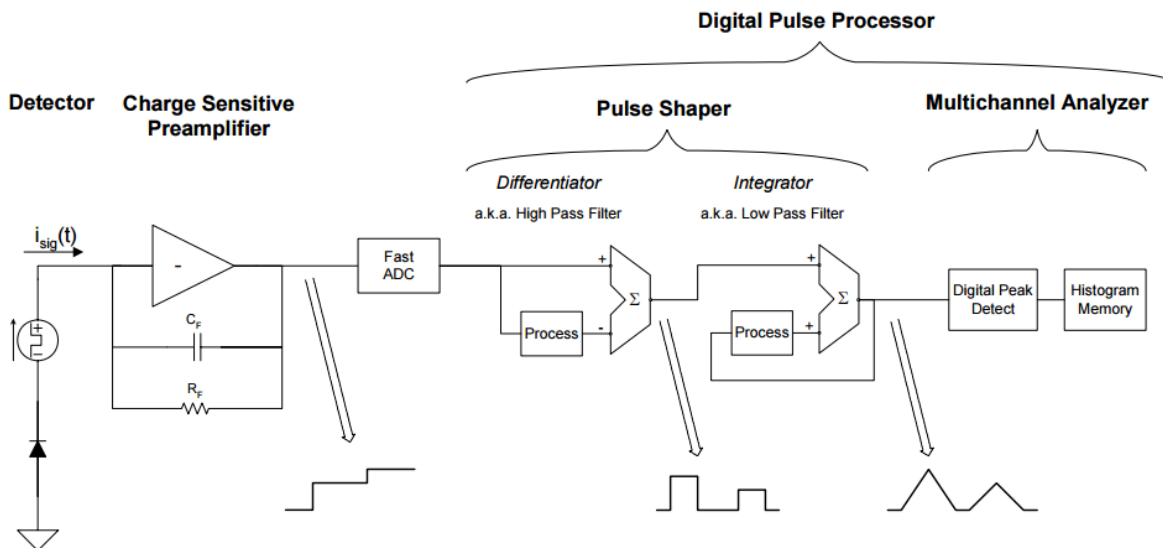


FIGURE 4.19: Schematic of an ideal digital pulse processor [45].

4.3.5 Signal acquisition using a Digital Pulse Processor (DPP)

The X-ray detector system that was installed on the sunrise side of CAST consisted of a Silicon Drift Detector and a preamplifier-readout card, both from PNDetector, Munich.

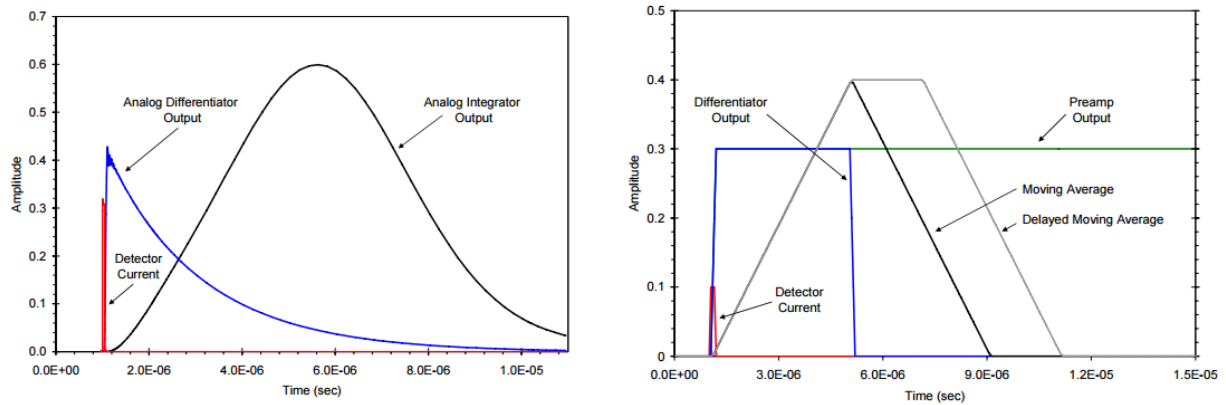


FIGURE 4.20: The shaped pulse and the output pulse of the differentiator in a) an analog pulse shaper in the left and b) in a Digital Pulse Processor in the right [45].

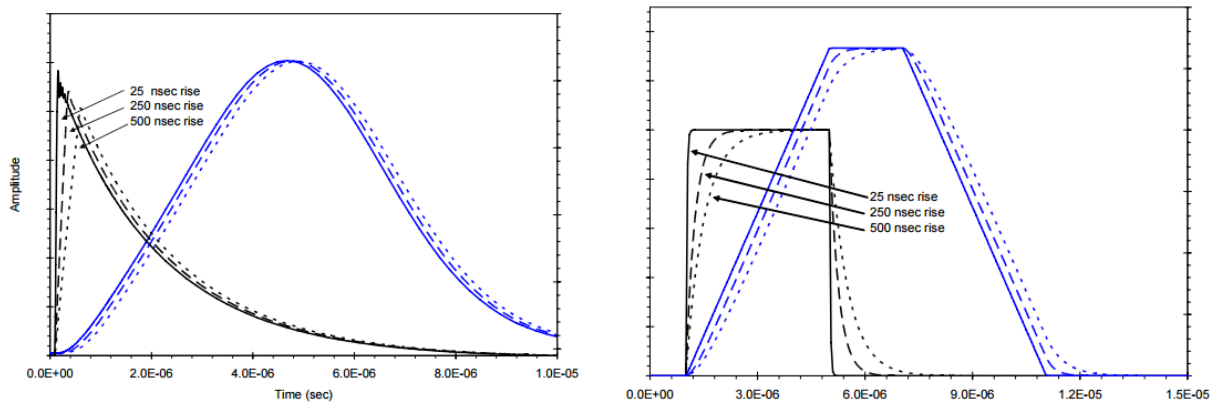


FIGURE 4.21: The differentiator output of a) an analog shaper on the left and b) a digital shaper on the right as a function of the rising time. For the analog shaper higher rising time leads to lower amplitude of the rise edge of the pulse and therefore loss of the actual amplitude of the preamplifier's signal [45].

For the readout of the system a PX5-Digital Pulse Processor from Amptek was used with a peaking time equal to $5.6 \mu s$, a reset pulse connected to the gate of the preamplifier board and an energy threshold of 168 eV. A flow diagram from this readout system is shown in figure 4.22.

Before installing the SDD on CAST, the detector was tested in the X-ray laboratory. The energy resolution was defined through the measured FWHM as a function of the energy of the characteristic peak of the target as can be seen in figure 4.23. Using carbon as a target the FWHM of the acquired spectrum was calculated equal to 39 eV.

After a few hours of run with the detector, a noticeable decrease of count rate in the range of 400-800 eV was observed, phenomenon proportional to the time elapsed by comparing the spectrum acquired directly after the cool-down of the detector with the spectrum taken after several hours as shown in figure 4.24. The drop of transmission due to the increasing deposition of hydrocarbon film on the surface of the detector can be seen for each energy bin in figure 4.25. This loss of efficiency was associated with the out gassing of electronic components of the system. The preamplifier board, the wiring and the connectors as well as the electrical vacuum feedthroughs were not High Voltage standard. Therefore, due to

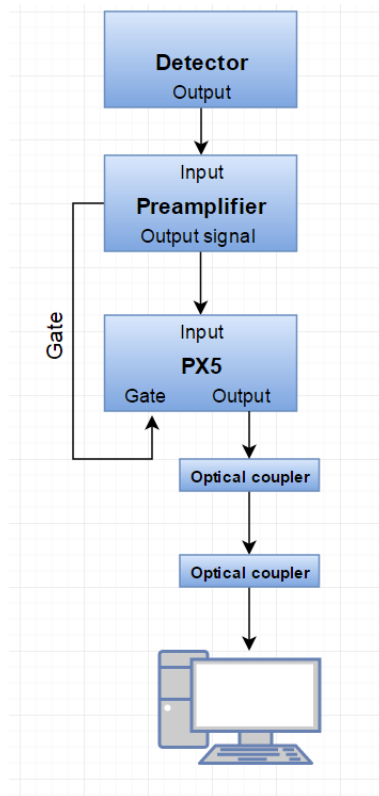


FIGURE 4.22: Flow diagram of the readout system of the SDD using a Digital Pulse Processor

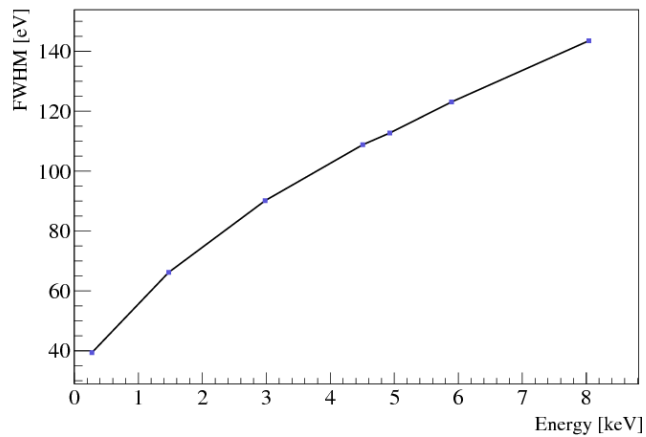


FIGURE 4.23: FWHM versus energy of the SDD [44].

the cryopumping of the SDD, which is operating at -30° , a thin film of hydrocarbon with a thickness increasing with time was deposited in the detector's surface. After 1 hour in ambient temperature, the efficiency of the detector recovered.

A solution to the out gassing of the electronic components was to remove the preamplifier board from the vacuum of the detector. This leads to an increased capacitance due to the

bond wires that connect the preamplifier and the detector and it could provoke electrical pickups, therefore a greater noise rate is expected. From equation 4.11, due to higher readout noise the FWHM increases and resulting a worse resolution. However, as can be seen from both figure 4.26 and figure 4.27 no noticeable decrease of count rate is observed with time after the preamplifier was removed from the vacuum system of the detector.

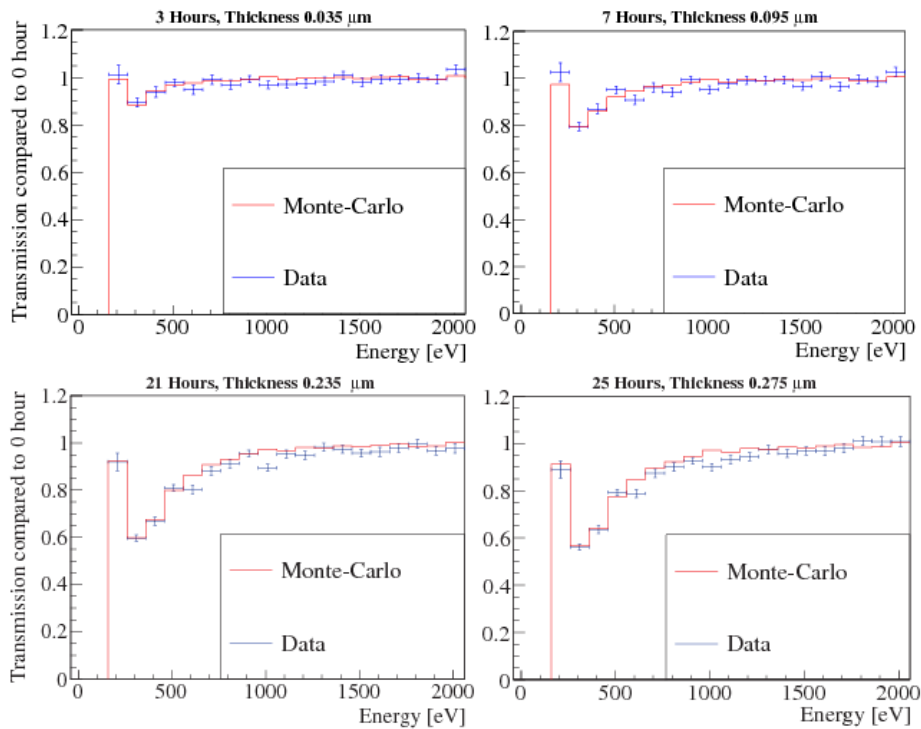


FIGURE 4.24: Comparison of the spectrum acquired from the run of the detector immediately after being cooled down with the data obtained after 3, 7, 21 and 25 hours later. The increasing drop of the count rate with time indicates a C_3H_6 film deposition on its surface. [44].

4.3.6 Upgrade of signal acquisition using a Spectroscopy Amplifier

The Canberra Model 2026 provides the option of Gaussian and Triangular pulse shaping for the Unipolar Output and six front panel switch-selectable shaping time constants. The flow diagram of the readout system using the spectroscopy amplifier and the MCA can be seen in Figure 4.28. All shaping methods and four time constants have been tested in order to optimize the resolution using multiple targets: Aluminium target with Aluminium filter, Copper target with Nickel filter, Manganese target with EIPC filter and Titanium target with EPIC filter for 0.5, 1, 2, 4, 6 μs

The DPMCA software of Amptek was used for the storage of the data of each run of tests. These data were used as an input to a ROOT program which, after calibration, reproduced the spectrum acquired as a function of energy. Then from the global fitting of the histogram a quadratic background fitting was subtracted resulting a more accurate fitting of the signal

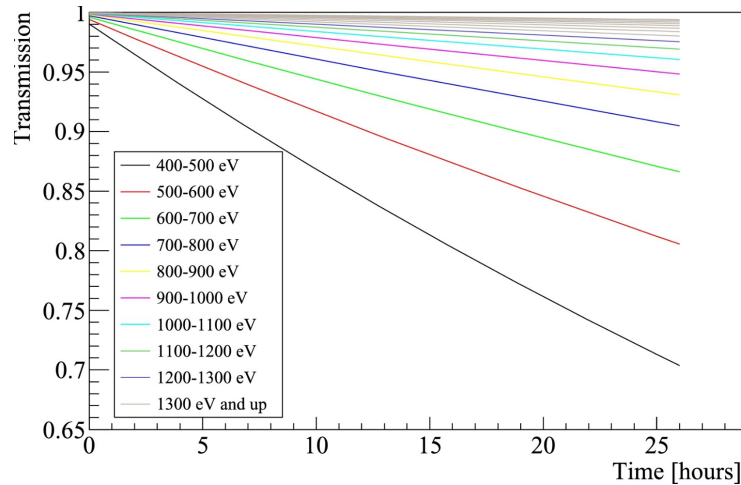


FIGURE 4.25: The drop in transmission due to the increasing deposition of the hydrocarbon film on the surface of the detector, for each energy bin, at the energy range of interest (400-1500 eV) [44].

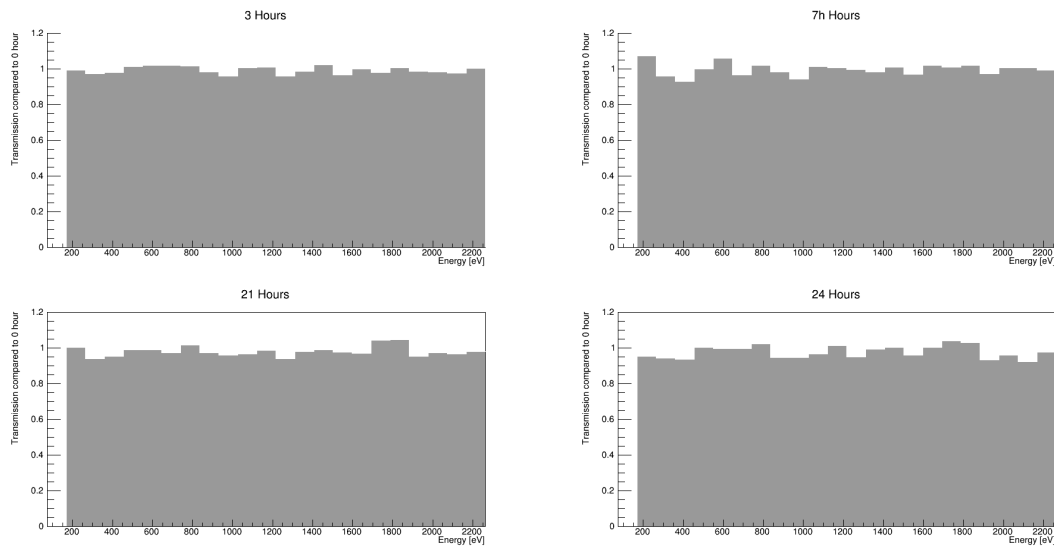


FIGURE 4.26: Comparison of the spectrum acquired from the start of the run of the detector with the spectrum obtained after 3,7,21 and 24 hours with the preamplifier board out of vacuum. No increasing drop of count rate is observed with time.

which was used to calculate the FWHM of the gaussian. Figures 4.29 and 4.30 show these fittings using Manganese as a target for gaussian and triangular shaping mode respectively and figures 4.31 and 4.32 for Titanium. The same analysis was done for all four targets and the FWHM as a function of the selected shaping time can be seen in figure 4.33. In most cases, the best resolution is achieved by selecting $1\mu s$ shaping time and Triangular shaping mode. These configurations will be used for the comparison of the efficiency of the readout systems in the next section.

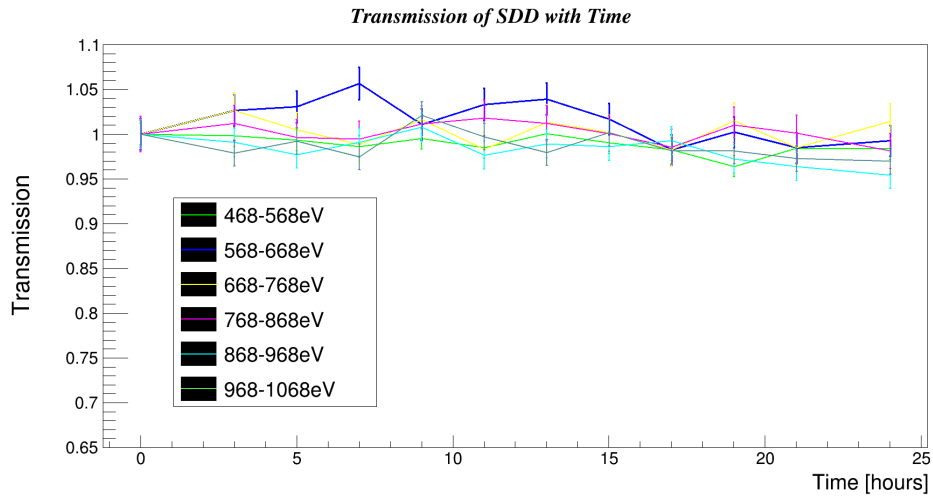


FIGURE 4.27: The transmission of the detector for each energy bin as a function of time indicates that no loss of efficiency is observed with the preamplifier outside of vacuum.

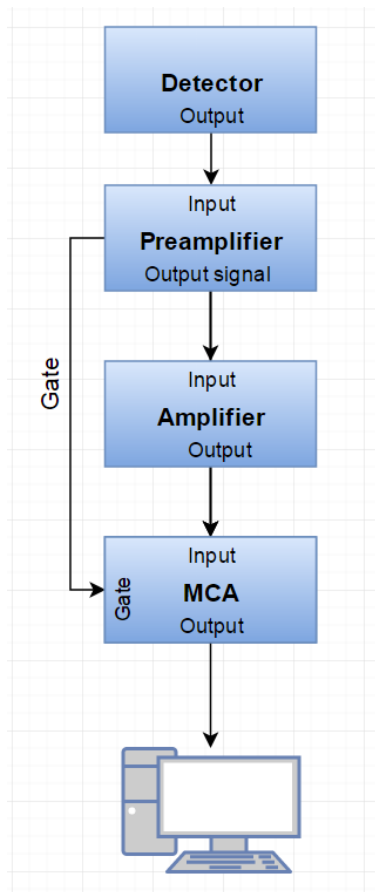


FIGURE 4.28: The flow diagram of the readout system using a spectroscopy amplifier and a MCA

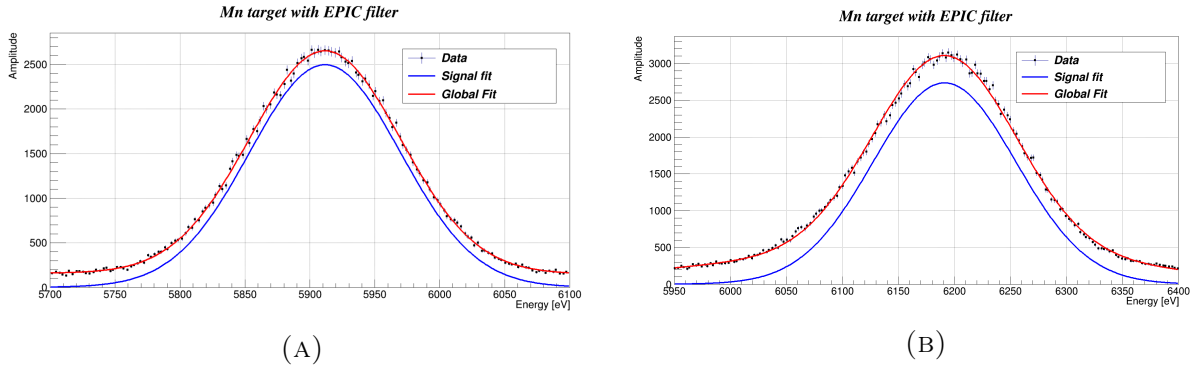


FIGURE 4.29: Fitting and background rejection of the spectrum acquired from Manganese target with EPIC filter for Gaussian pulse shaping and for A) $0.5\mu s$ shaping time B) $6\mu s$ shaping time

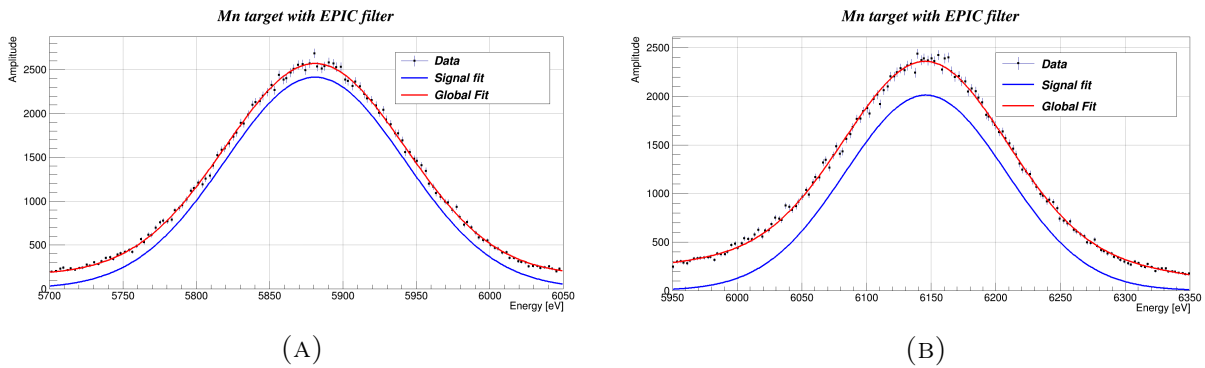


FIGURE 4.30: Fitting and background rejection of the spectrum acquired from Manganese target with EPIC filter for Triangular pulse shaping and for A) $0.5\mu s$ shaping time B) $6\mu s$ shaping time

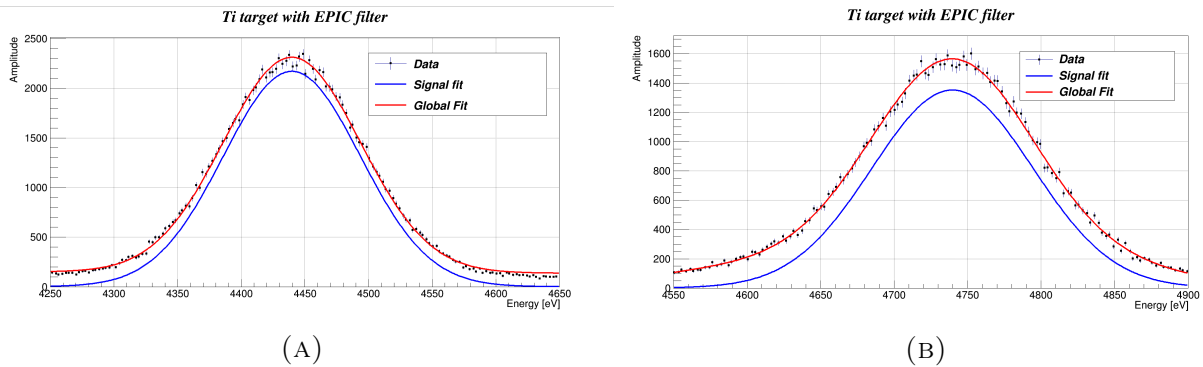


FIGURE 4.31: Fitting and background rejection of the spectrum acquired from Titanium target with EPIC filter for Gaussian pulse shaping and for A) $0.5\mu s$ shaping time B) $6\mu s$ shaping time

4.3.7 Comparison of signal acquisition systems

Background noise

For the comparison of the noise rates between the two readout systems, the detector was cooled down and the high voltage for the operation of the Silicon Drift Detector was set to

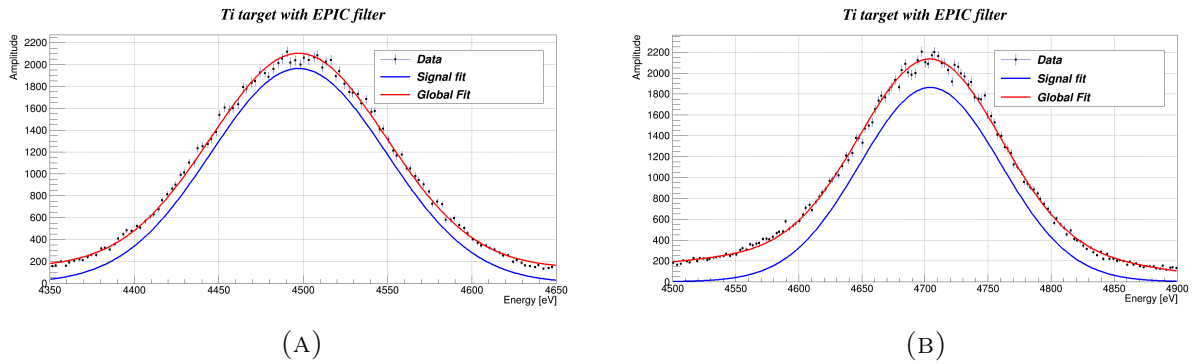


FIGURE 4.32: Fitting and background rejection of the spectrum acquired from Titanium target with EPIC filter for Triangular pulse shaping and for A) $0.5\mu\text{s}$ shaping time B) $6\mu\text{s}$ shaping time

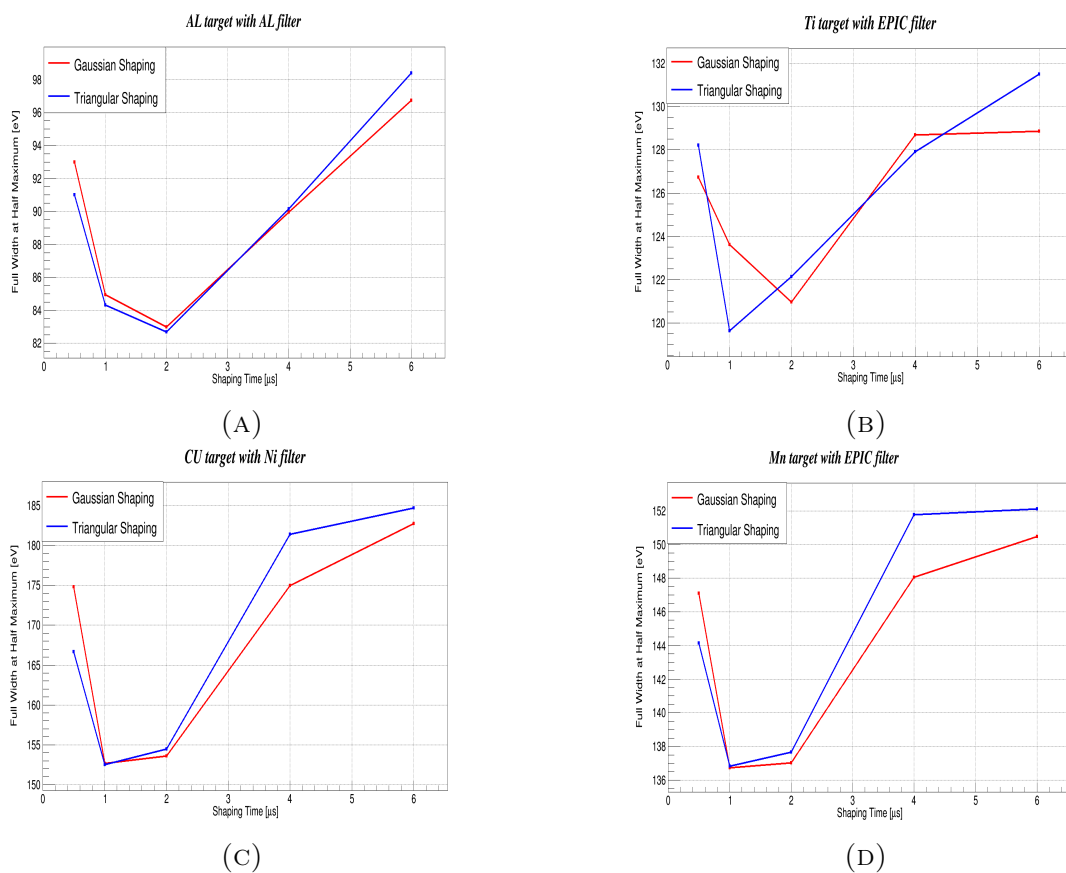


FIGURE 4.33: Full Width at Half Maximum as a function of the Shaping Time constant for A) Aluminium target with Aluminium Filter B) Titanium target with EPIC filter C) Copper target with Nickel filter and D) Manganese target with EPIC filter

its nominal value (170 V). The mode of the spectroscopy amplifier was set to $1\mu\text{s}$ shaping time and triangular shaping. The rate of noise in the spectroscopy amplifier system for the whole spectrum (150-10000 eV) was calculated equal to 11.024 mHz while the noise rate for energies in the range 400-1500 eV for each bin of 100 eV can be seen in figure 4.34. For the range 400-1500 eV the noise rate is equal to 2.417 mHz. For the PX5 system the total noise

rate was calculated equal to 36.903 mHz and the the noise rate for energies in the range 400-1500 eV for each bin of 100 eV are shown in figure 4.35. For the range 400-1500 eV the noise rate is equal to 10.305 mHz.

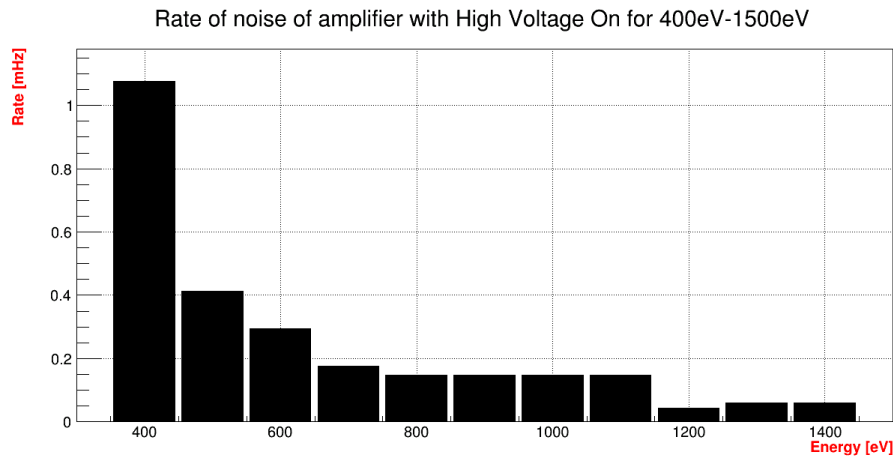


FIGURE 4.34: Noise rate of each 100 eV bin for the range of 400-1500 eV using the spectroscopy amplifier.

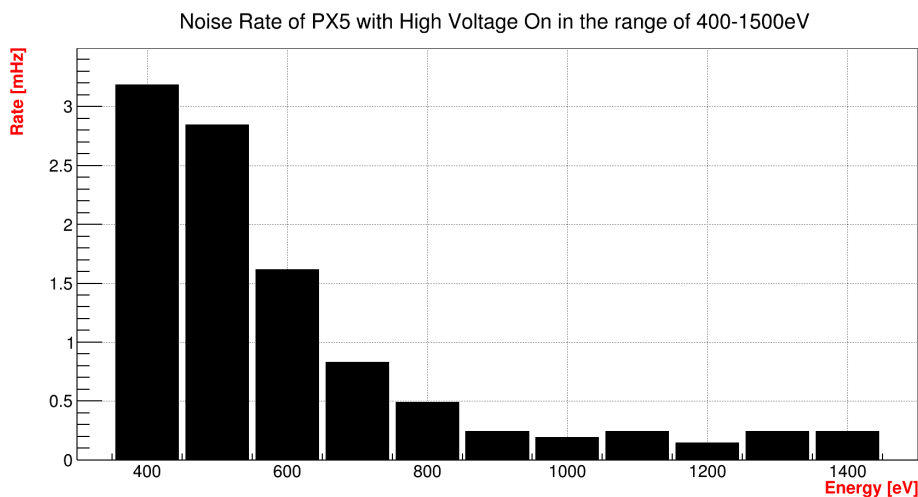


FIGURE 4.35: Noise rate of each 100 eV bin for the range of 400-1500 eV using the PX5.

X-ray peaks

For the comparison of the X-ray peaks Aluminum and Copper were selected as targets. The spectrum and fittings can be seen in 4.38 for aluminum, 4.39 for copper and 4.36 for aluminum, 4.37 for copper for the amplifier and the PX5 respectively. From these fittings the FWHM of each Gaussian was calculated and plotted (figure 4.40).

4.3.8 Conslusions

The results from the system with the amplifier and the one with the PX5 indicate that the FWHM values of the acquired spectra are approximately equal for both readouts, which

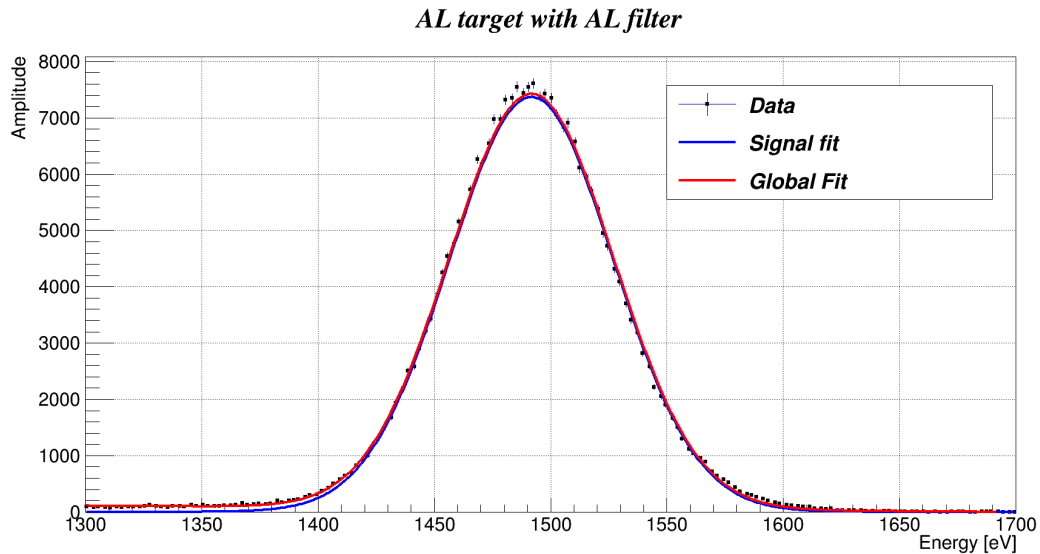


FIGURE 4.36: Fitting and background reduction for the Aluminum spectrum acquired using the PX5 system.

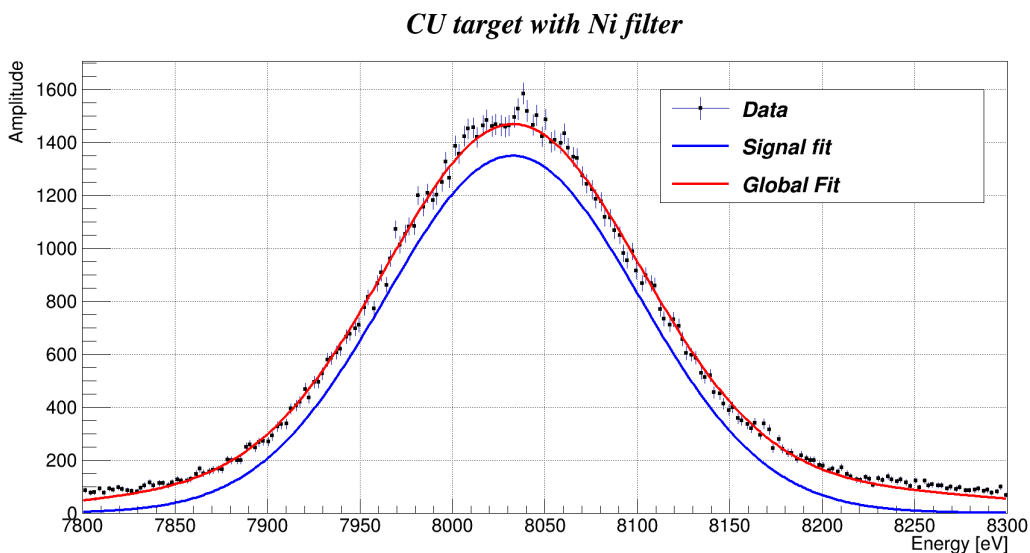


FIGURE 4.37: Fitting and background reduction for the Copper spectrum acquired using the PX5 system.

leads to equivalent resolution. The noise rates show an increase noise level by a factor of three in the case of the PX5, however this does not seem to affect the form of characteristic peaks of the targets. During the background measurements of the detector with the high voltage on in the laboratory, it was noticed that bursts of noise were detected from the environment. These bursts of noise were not present when the detector was used in the experiment because of the additional shielding. The results of the spectroscopy amplifier are similar to the ones acquired when the SDD was tested in the laboratory in 2013. The PX5 proved to be more sensitive to noise pickup and therefore a higher noise rate was observed compared to the spectroscopy amplifier.

With both systems a shift in the FWHM, equal to a mean value of 10-15 eV, was observed compared to the data acquired with the preamplifier inside the vacuum. This can

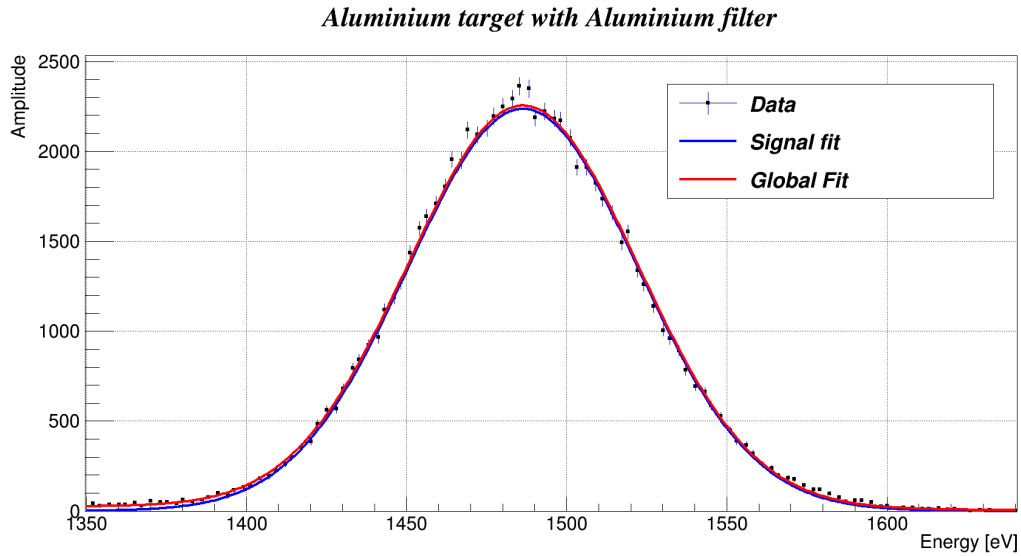


FIGURE 4.38: Fitting and background reduction for the Aluminum spectrum acquired using the spectroscopy amplifier for Triangular shaping mode with $1\mu s$ shaping constant

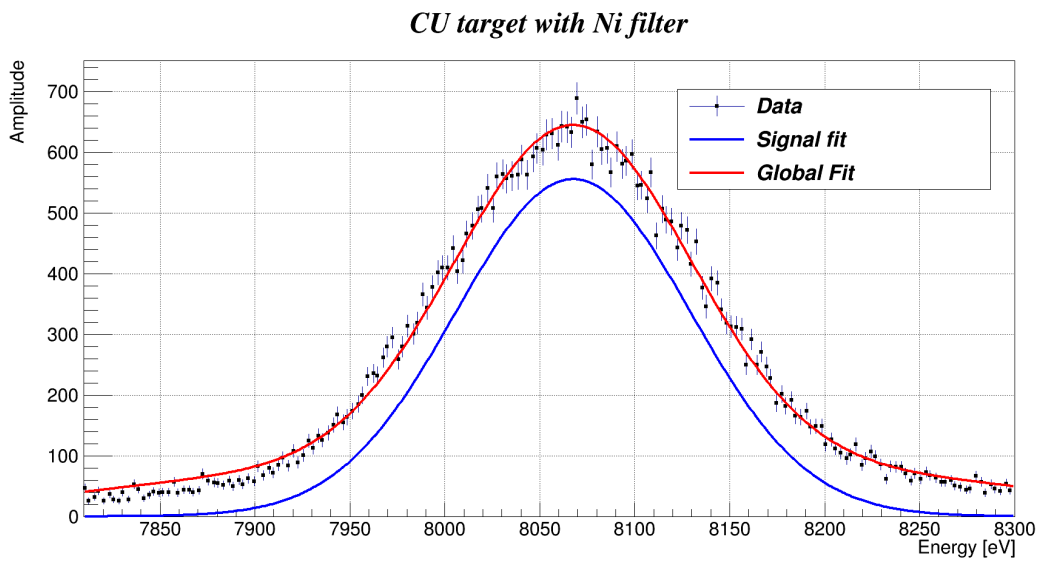


FIGURE 4.39: Fitting and background reduction for the Copper spectrum acquired using the spectroscopy amplifier for Triangular shaping mode with $1\mu s$ shaping constant.

be explained as a result of the increased length of the cables used for the coupling of the detector with the preamplifier, resulting a greater capacitance.

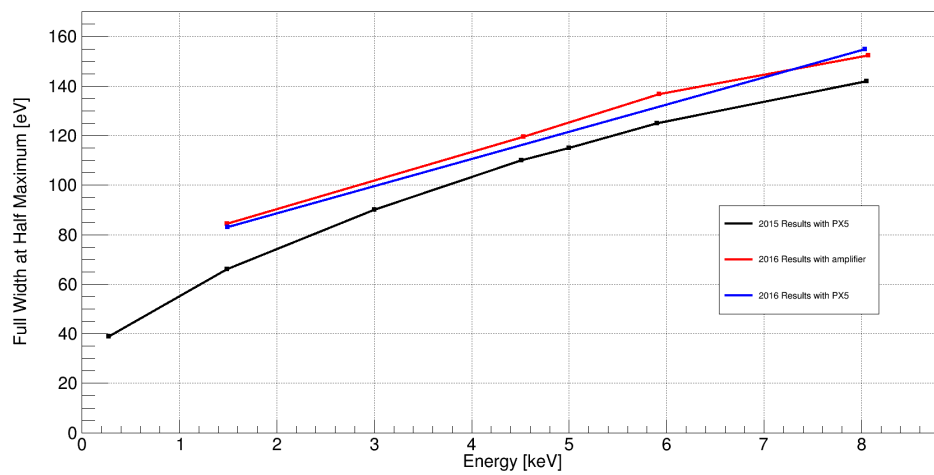


FIGURE 4.40: FWHM as a function of the energy of each characteristic peak for the data of 2015 and 2016 for the two readout systems. A higher FWHM is observed in 2016 with the preamplifier outside vacuum resulting to a worse resolution, which can be attributed to the longer distance between the detector and the preamplifier.

Chapter 5

Future prospects

5.1 Microwave cavities for axion detection

5.1.1 Introduction

Due to the fact that axions are a cold dark matter candidate, the searches have been focused on the detection of galactic halo axions. This can be achieved by employing microwave cavities permeated by the strong magnetic field in the cold bores of the magnet [46]. The novelty of the searches relies on the use of rectangular cavities in a dipole magnet, while up to now solenoid magnets have been used with cylindrical cavities [47, 48, 49], resulting a sensitivity that reaches regions that have never been explored. In Figure 5.1 the orange region involves dark matter axions. The lighter shaded orange area includes axions that can still be dark matter candidates but with decreasing mass this requires an increasing amount of fine tuning. The black region refers to the sensitivity achieved by other experiments. The light green regions are the expected sensitivity of a dipole search and the solidly shaped part corresponds to the region probed by a cavity with the parameters that will be used in the CAST experiment .

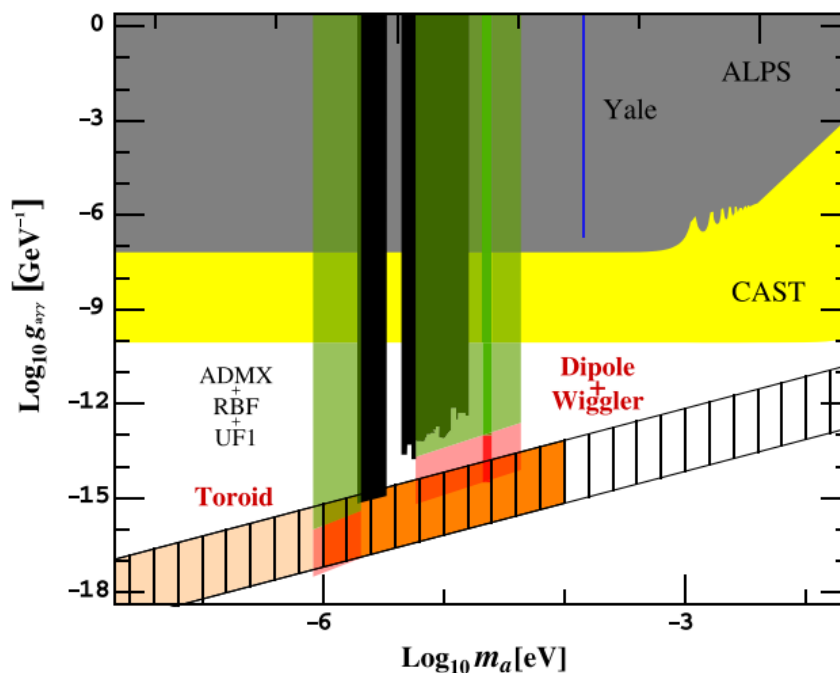


FIGURE 5.1: Existing bounds for ALPs. Achieved and expected limits in black and green respectively [46].

5.1.2 Haloscope operating principle

The wave equation of the electric field inside the cavity is equal to:

$$\nabla^2 \vec{E} - \mu\epsilon \frac{\partial^2 \vec{E}}{\partial t^2} = 0 \quad (5.1)$$

where:

μ is the permeability

ϵ is the permittivity

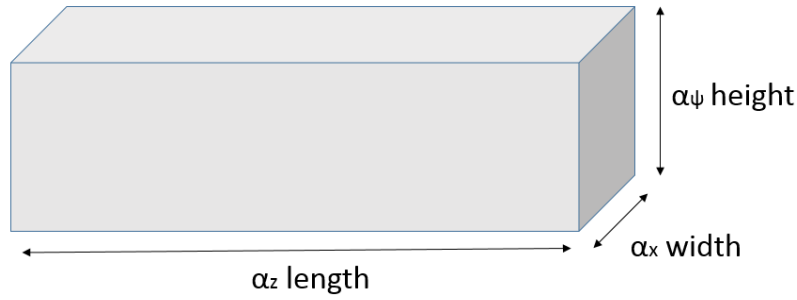


FIGURE 5.2: A rectangular cavity

The solution of the wave equation in free space is:

$$\vec{E}(\vec{r}, t) = E_0 e^{j(\omega t - \vec{k}\vec{r})} \quad (5.2)$$

where \vec{k} the wave vector

For the solution of the equation 5.2 it must be taken into account that $E_x = 0$ for $\psi = 0$, $z = 0$, $\psi = \alpha_\psi$ and $z = \alpha_z$. Similar conditions must be applied to the other field components E_ψ and E_z . In order to satisfy the boundary conditions at the wall of the cavity:

$$E_x = E_{x0} \cos(k_x x) \sin(k_\psi \psi) \sin(k_z z) e^{j\omega t} \quad (5.3)$$

$$E_y = E_{y0} \sin(k_x x) \cos(k_\psi \psi) \sin(k_z z) e^{j\omega t} \quad (5.4)$$

$$E_z = E_{z0} \sin(k_x x) \sin(k_\psi \psi) \cos(k_z z) e^{j\omega t} \quad (5.5)$$

where k_x , k_ψ and k_z the wave numbers of the field components

For the dimensions seen in figure 5.2:

$$k_x = \frac{\pi n_x}{a_x}, \quad k_\psi = \frac{\pi n_\psi}{a_\psi}, \quad k_z = \frac{\pi n_z}{a_z} \quad (5.6)$$

where n_x , n_ψ and n_z the integer mode numbers and a_x , a_ψ and a_z the height, width and length of the cavity respectively. The wave vector and the frequency must be related:

$$\vec{k}^2 = k_x^2 + k_\psi^2 + k_z^2 = \frac{\omega^2}{c^2} \quad (5.7)$$

The resonant frequencies are equal to:

$$\omega = \pi c \sqrt{\frac{n_x^2}{\alpha_x^2} + \frac{n_\psi^2}{\alpha_\psi^2} + \frac{n_z^2}{\alpha_z^2}} \quad (5.8)$$

where c is the speed of light inside the cavity From Maxwell 's equation:

$$\nabla \times \vec{E} = -j\omega\vec{B} \quad (5.9)$$

the magnetic field is perpendicular to the electric field. Assuming that:

$$\vec{E} \sim \cos(\omega t + \phi_0) \text{ and } \vec{B} \sim \sin(\omega t + \phi_0) \quad (5.10)$$

the Poynting vector can be calculated as:

$$\vec{S} = \vec{E} \times \vec{H} \sim \cos(\omega t + \phi_0)\sin(\omega t + \phi_0) = \frac{1}{2}\sin 2(\omega t + \phi_0) \quad (5.11)$$

with a time-averaged value:

$$\langle \vec{S} \rangle \sim \langle \sin 2(\omega t + \phi_0) \rangle = 0 \quad (5.12)$$

which means that energy is transferred only between the electric and the magnetic field and that the waves inside the cavity are standing waves.

The lowest resonant frequencies are the most isolated, while overlapping modes can lead to reduction in sensitivity. The lowest allowed frequency can be found by setting to zero the integer of the smallest dimension. In CAST $\alpha_\psi < \alpha_x < \alpha_z$ which leads to the $TE_{x\psi z} = TE_{101}$ mode. The fundamental frequency of such a cavity will be:

$$\omega = \pi c \sqrt{\frac{1}{\alpha_x^2} + \frac{1}{\alpha_z^2}} \quad (5.13)$$

The resonant field of the TE_{101} mode:

$$E_x = 0 \quad (5.14)$$

$$E_\psi = E_0 \sin\left(\frac{\pi n_x}{\alpha_x}\right) \sin\left(\frac{\pi n_z}{\alpha_z}\right) e^{j\omega t} \quad (5.15)$$

$$E_z = 0 \quad (5.16)$$

From Maxwell 's equation the magnetic field will be equal to:

$$B_x = -j \frac{k_z}{\omega} E_0 \sin\left(\frac{\pi n_x}{\alpha_x}\right) \cos\left(\frac{\pi n_z}{\alpha_z}\right) e^{j\omega t} \quad (5.17)$$

$$B_\psi = 0 \quad (5.18)$$

$$B_z = j \frac{k_x}{\omega} E_0 \cos\left(\frac{\pi n_x}{\alpha_x}\right) \sin\left(\frac{\pi n_z}{\alpha_z}\right) e^{j\omega t} \quad (5.19)$$

For the characteristics of the CAST magnet a inner dimensions $25mm \times 24mm$ cavity will be used. From equation 5.13:

$$\omega = \pi \cdot 3 \cdot 10^8 m/s \sqrt{\frac{1}{(24mm)^2} + \frac{1}{(25mm)^2}} \quad (5.20)$$

$$f = \frac{\omega}{2\pi} = 6.3 \text{ GHz} \quad (5.21)$$

The relation between the resonant frequency f and of the cavity equals the mass m_a , galactic halo axions convert into photons [50]:

$$f \approx \frac{m_a}{h} \quad (5.22)$$

where h is the Planck constant. By using a dielectric tuning mechanism the fundamental mode frequency can be modified, corresponding to other values of the axion masses.

The rate of energy dissipation is characterized by the quality factor, Q :

$$E(t) = E(0)e^{-\frac{\omega t}{Q}} \quad (5.23)$$

where:

E is the energy

Q is the number of cycles before the energy is reduced by a factor of $1/e$ and it can be defined as:

$$Q = \frac{f}{FWHM} \quad (5.24)$$

with FWHM the full width at half maximum and f the resonant frequency. The quality factor of the cavity can be expressed [51]:

$$Q = \left(\frac{1}{Q_c} + \frac{1}{Q_d}\right)^{-1} \quad (5.25)$$

where:

Q_c the loaded quality factor, which is the power loss from the walls of the cavity

Q_d the unloaded quality factor, which is the power loss from the dielectric material and it has the dominant effect on Q [51].

The time required to reach a given signal-to-noise ratio is calculated from the Dicke radiometer equation as [48]:

$$SNR = \frac{P_a}{P_N} \sqrt{bt} = \frac{P_a}{k_B T_s} \sqrt{\frac{t}{b}} \quad (5.26)$$

where:

P_a is the power output

P_N is the noise output

k_b is the Boltzmann 's constant

b is the bandwidth

T_s is the total system noise temperature which is equal to the temperature of the cavity and the noise of the amplifier.

By using the typical velocity distribution of dark matter ALPs $\Delta v_a \sim 10^{-3}c$ the bandwidth can be determined as [46]:

$$2\pi b_a = m_a \left(\frac{1}{\sqrt{1 - \delta v_a^2}} - 1 \right) \sim 10^{-6} m_a \quad (5.27)$$

From equation 5.26 the time required for one measurement is equal to:

$$t = (SNR)^2 \left(\frac{k_B T_s}{P_a} \right)^2 b_a \quad (5.28)$$

5.1.3 Rectangular cavities in the CAST dipole magnet

Cavities and tuning mechanism

Each microwave cavity will be a copper-plated, stainless-steel rectangular inner dimensions $25 \times 24 \times 500$ mm cavity locked inside the magnet's bores. For a total 46% effective volume of the magnet filled, a Q value of 5000 and a total temperature of 3.8 K, it has been estimated that for a coupling constant of $g_{a\gamma\gamma} = 10^{-14} \text{ GeV}^{-1}$ the time needed for one frequency measurement is 10 days whereas for $g_{a\gamma\gamma} = 10^{-13} \text{ GeV}^{-1}$ it is equal to one minute [52]. These values reach unexplored regions of the axion searches which will be scanned through a tuning mechanism. With the use of Sapphire or Alumina bars placed parallel to the resonator long sides the field in the cavity is modified, as the electromagnetic waves inside the dielectric material propagate with lower phase velocity [52]. A piezo actuator will move the bars closer to the center, resulting a lower resonant frequency and therefore a shift of the sensitivity to lower masses [46].

Electronics

- **Antenna:** The readout of the signal of the cavity starts with the antenna. The microwave signal is picked up by the antenna and transmitted to the first amplification stage.
- **Heterojunction field effect transistor (HFET-HMET) amplifier:** HFET are low-noise amplifiers, available in the GHz frequency range. The first-stage amplifiers will be placed on top of a gold-plated copper plate inside a vacuum vessel at cryogenic temperatures and outside of the bores of the magnet to prevent any degradation of the signal due to fringe field effects. Conventional doping techniques increase the free carrier concentration and conductivity of the semiconductor but it leads to reduction of carrier mobility due to scattering with the impurities. HFET is a layered structure of different semiconductor materials with different bandgaps that form a heterostructure. A highly n-type doped material with a wide bandgap, usually AlGaAs, is connected with a non-doped material with a more narrow bandgap, in most cases GaAs. The conduction band of the doped AlGaAs lies energetically higher than the one of the

GaAs. The electrons move to the undoped GaAs side where the energy state is lower and the concentration of electrons is increased. In this side electrons do not interact with donors. This technique does not compromise the mobility of the carriers as it causes increase of the concentration of free carriers without dopant impurities added [53]. The amplified signal is transmitted through the hermetically sealed feedthroughs of the vacuum vessel to ambient temperature for further amplification.

- **Directional coupler:** The directional coupler between the cavity and the cryogenic amplifier allows the application of test and calibration signals. By applying a rf signal through the directional coupler the cable and connectors attenuation response can be determined [49].

Bibliography

- [1] R.D. Peccei and H.R. Quinn. “CP Conservation in the Presence of Pseudoparticles”. In: *Physical Review Letters* 38(25):1440 (1977).
- [2] G. 't Hooft. “Symmetry Breaking through Bell-Jackiw Anomalies”. In: *Physical Review Letters* 37(1):8 (1976).
- [3] G. 't Hooft. “Computation of the quantum effects due to a four-dimensional pseudoparticle”. In: *Physical Review D* 14(12):3432 (1976).
- [4] S. Weinberg. “The U(1) Problem”. In: *Physical Review D* 11(12):3583 (1975).
- [5] V. Baluni. “CP-nonconserving effects in quantum chromodynamics”. In: *Physical Review D* 19,2227 (1979).
- [6] S. Weinberg. “A New Light Boson”. In: *Physical Review Letters* 4 (1978).
- [7] R.D. Peccei and H.R. Quinn. “CP conservation in the Presence of Instantons”. In: *Physical Review Letters* 38,1440 (1977).
- [8] R.D. Peccei and H.R. Quinn. “Constraints imposed by CP conservation in the presence of instantons”. In: *Physical Review D* 16,1791 (1977).
- [9] R.D. Peccei. “QCD, Strong CP and Axions”. In: *Journal of the Korean Physical Society* 29:S199-S208 (1996).
- [10] G. G. Raffelt. “Axions-Motivation, limits and searches”. In: *Journal of Physics* A40 (2006).
- [11] J.E. Kim. “Light pseudoscalars, particle physics and cosmology”. In: *Physics Reports* 109 (1987).
- [12] I. Antoniadis and T.N. Truong. “g, Lower bound for branching ratio of axion and non-existence of Peccei-Quinn axion”. In: *Physics Letters B* 109 (1982).
- [13] A.I. Vainshtein, M.A. Shifman and V.I. Zakharov. “Can confinement ensure natural CP invariance of strong interactions?” In: *Nuclear Physics* 166(3):49 (1980).
- [14] J. E. Kim. “Weak-Interaction Singlet and Strong CP Invariance”. In: *Physical Review Letters* 43(2):103 (1979).
- [15] W. Fischler, M. Dine and M. Srednicki. “A simple solution to the strong CP problem with a harmless axion”. In: *Physical Letters B* 104(3):199 (1981).
- [16] G.G. Raffelt. “Astrophysical axion bounds”. In: *Lecture Notes in Physics* 741 (2008).
- [17] G.G. Raffelt. “Stars as laboratories for fundamental physics”. In: *University of Chicago Press* (1996).
- [18] F.D. Steffen. “Dark Matter Candidates - Axions, Neutralinos, Gravitinos, and Axinos”. In: *European Physical Journal* C59 (2008).
- [19] S. J. Asztalos et al. “Searches for Astrophysical and Cosmological Axions”. In: *Annual Review of Nuclear and Particle Science* (2006).

- [20] H. Primakoff. “Photo-Production of Neutral Mesons in Nuclear Electric Fields and the Mean Life of the Neutral Meson”. In: *Physical Review* 81(5)889 (1951).
- [21] S. Andriamonje et al. “An improved limit on the axion-photon coupling from the CAST experiment”. In: *Journal of Cosmology and Astroparticle Physics* (2007).
- [22] Cenk Yildiz. “Search for Axions with micromegas detectors in the CERN CAST experiment”. PhD thesis. Bogazici University, 2013.
- [23] K. Zioutas et al. “A decommissioned LHC model magnet as an axion telescope”. In: *Nuclear Instruments and Methods in Physics Research A* 425 (1999).
- [24] K.Zioutas et al. “First Results from the CERN Axion Solar Telescope”. In: *Physical Review Letters* 94 (2005).
- [25] S.Andriamonje et al. “An improved limit on the axion–photon coupling from the CAST experiment”. In: *Journal of Cosmology and Astroparticle Physics* 94 (2007).
- [26] M.Arik et al. “Search for Solar Axions by the CERN Axion Solar Telescope with 3He Buffer Gas:Closing the Hot Dark Matter Gap”. In: *Physical Review Letters* 112 (2014).
- [27] E. Arik et al. “Search for Sub-eV Mass Solar Axions by the CERN Axion Solar Telescope with 3He Buffer Gas”. In: *Physical Review Letters* 107 (2011).
- [28] E. Arik et al. “Probing eV-scale axions with CAST”. In: *Journal of Cosmology and Astroparticle Physics* 94 (2009).
- [29] K.Barth et al. “Commissioning and First Operation of the Cryogenics for the CERN Axion Solar Telescope (CAST)”. In: *AIP Conference Proceedings* 710 (2004).
- [30] T. Vafeiadis. “Contribution to the search for solar axions in the CAST experiment”. In: 62 (2012), pp. 107–122. URL: <https://cds.cern.ch/record/1607071/files/CERN-THESIS-2012-349.pdf>.
- [31] National Instruments. *Complete guide to build a measurement system*. http://download.ni.com/evaluation/daq/Measurement_System_Build_Guide.pdf. [Online; accessed 24-April-2016].
- [32] Texas Instruments Incorporated. *How delta-sigma ADCs work, Part 1l*. <http://www.ti.com/lit/an/slyt423/slyt423.pdf>. [Online; accessed 24-April-2016].
- [33] L.J Breems M. Bolatkale and K.A.A. Makinwa. *High Speed and Wide Bandwidth Delta-Sigma ADCs*. Springer, 2014.
- [34] National Instruments. *M series User Manual*. <http://www.ni.com/pdf/manuals/371022k.pdf>. [Online; accessed 24-April-2016].
- [35] S.J. Chapman. *Electric Machinery Fundamentals*. Mc Graw Hill, 2005.
- [36] Allen-Bradley. *Frequency controlled AC motor drive*. <https://www.ab.com/support/abdrives/documentation/fb/1024.pdf>. [Online; accessed 24-April-2016].
- [37] Amptek. *Understanding Characteristic X-Rays*. http://amptek.com/pdf/characteristic_xrays.pdf. [Online; accessed 24-April-2016].
- [38] M. D’Aloia M. Rizzi and B. Castagnolo. “Detectors and Principles of Radiation-matter Interaction”. In: *Journal of Applied Sciences* 10 (2010), pp. 3141–3155. URL: <http://scialert.net/abstract/?doi=jas.2010.3141.3155>.

- [39] N. Tsoulfanidis. *Measurement and detection of radiation*. London: Taylor & Francis, 1995.
- [40] R. V. Grieken K. Tsuji J. Injuk. *X-Ray Spectrometry: Recent Technological Advances*. John Wiley & Sons, Ltd, 2004.
- [41] P. Rehak E. Gatti. “Semiconductor Drift Chamber - An Application of a Novel Charge Transport Scheme”. In: *Nucl. Instr. and Meth A* 225 (1984), pp. 608–614.
- [42] B. Beckhoff et al. *Handbook of Practical X-Ray Fluorescence Analysis*. Germany: Springer Science & Business Media, 2007.
- [43] PN detector. *The Complete SDD Module*.
- [44] V. Anastassopoulos et al. [CAST Collaboration]. “Search for chameleons with CAST”. In: *Physics Letters B* 749 (2015), pp. 172–180. URL: [arXiv:1503.04561%20\[astroph.SR\]](https://arxiv.org/abs/1503.04561).
- [45] Amptek. *Digital Pulse Processors Theory of Operation*. http://www.amptek.com/pdf/dpp_theory.pdf. [Online; accessed 24-April-2016].
- [46] O.K Baker et al. “Prospects for searching axionlike particle dark matter with dipole, toroidal, and wiggler magnets”. In: *Physical Review D* 85, 035018 (2012).
- [47] S. J. Asztalos et al. “Improved rf cavity search for halo axions”. In: *Physical Review D* 69, 011101(R) (2004).
- [48] S. J. Asztalos et al. “SQUID-Based Microwave Cavity Search for Dark-Matter Axions”. In: *Physical Review Letters* 69, 011101(R) (2010).
- [49] S. J. Asztalos et al. “Large-scale microwave cavity search for dark-matter axions”. In: *Physical Review D* 64, 092003 (2001).
- [50] W. U. Wuensch et al. “Results of a laboratory search for cosmic axions and other weakly coupled light particles”. In: *Physical Review D* 10 (1989).
- [51] D. Pozar. *Microwave Engineering*. New York: Wiley, 1998.
- [52] K.Zioutas G. Cantatore L. Miceli. “Search for solar chameleons and relic axions with CAST”. In: *CERN-SPSC SPSC-P-352* (2015).
- [53] R.F Bradley. “Cryogenic, low-noise, balanced amplifiers for the 300-1200 MHz band using heterostructure field-effect transistors”. In: *Nuclear Physics B (Proc. Suppl.)* 72 (1999).